UNIVERSITY OF SOUTHAMPTON

Hydrography and Flow in the Rift Valley of the Mid-Atlantic Ridge

Andreas M. Thurnherr

Submitted for the degree of Doctor of Philosophy

School of Ocean and Earth Sciences

April 2000

Abstract

Slow-spreading mid-ocean ridges such as the Mid-Atlantic Ridge are characterized by deep axial rift valleys which are isolated from the water on the ridge flanks. Topographic effects therefore have a significant impact on the rift-valley hydrography and dynamics but little is known about the details. Known processes of global importance acting near the axes of mid-ocean ridges include high rates of diapycnal mixing associated with the rough topography and high-temperature hydrothermal circulation, a major source for a number of chemical constituents of the ocean.

Physical data sets from the rift valley of two connected segments of the Mid-Atlantic Ridge, which include the largest known hydrothermal vent field of the Atlantic, were analyzed to investigate the segment-scale hydrography, dynamics and geothermal fluxes. The data include two quasi-synoptic hydrographic and particle plume surveys (one year apart) and one-year-long records from an array of moored current meters.

The hydrographic properties of the rift-valley water were similar during the two surveys, suggesting a stable state characterized by inflow from the eastern ridge flank, unidirectional along-segment flow (directly observed during an entire year), and monotonic along-valley hydrographic gradients consistent with high rates of diapycnal mixing. Geothermal processes do not appear to contribute significantly to these patterns. The data contain signatures of a range of dynamical processes consistent with high rates of diapycnal mixing, including hydraulically controlled sill flows, topographic lee waves and high-energy tidal flows.

The spatial distribution of the light-scattering anomalies associated with the dispersing hydrothermal particle plume are consistent with the dynamical observations. Close to the vent field the particle distribution is highly inhomogeneous but density-averaged profiles indicate that the mean plume is Gaussian in depth. To quantify the fluxes associated with the hydrothermal plume the corresponding hydrographic anomalies were determined. The

complexity of the hydrography within the rift valley precludes the application of "standard" methods so that a new method had to be developed resulting in the first quantitative hydrographic anomaly measurements of an Atlantic hydrothermal plume. The hydrographic and particle anomalies of this plume are linearly correlated, indicating that the particles behave conservatively in the near field.

Estimates for the heat flux associated with the hydrothermal plume were derived using two established methods, one based on plume-rise modeling and the other on the advection of heat anomalies away from the vent field. Height-of-rise modeling yields values which are an order of magnitude too low because the plume model relies on a point-source assumption which is violated by the geometry of the vent field. The uncertainties associated with the advection method are particularly small at the site studied because of the uni-directionality of the flow field, the small uncertainties of the hydrographic anomaly measurements, and the Gaussian shape of the averaged near-field plume. The resulting estimate for the heat flux associated with the particle plume is 2.5 GW.

Mass and heat budgets of the rift valley indicate that high diapycnal diffusivities are required to account for the hydrographic observations and suggest that a portion of the water flowing along the rift valley may be lost to the overlying water column. Inspired by the observations a simple analytical and numerical model for the flow within the rift valley was developed. The results indicate that the rift valley acts as an efficient low-pass filter with characteristic time scales of weeks to months, providing a plausible explanation for the persistence of the along-segment flow.

Acknowledgments

I would like to thank my supervisors Kelvin Richards, Chris German and Greg Lane-Serff for their support and also Steve Thorpe for getting me interested in processes of physical oceanography.

Financial support was provided by the British taxpayers (to whom I am especially grateful) via the University of Southampton and an Oversea Research Studentship, by the unwitting customers of Digicomp AG in Switzerland, by UNESCO, and by a variety of my supervisors' grants.

My life during the last three years has been made enjoyable by my friends in Southampton (especially Alan, Luca and Magali) and in Zurich (especially JdB and Renato). Christof has provided me with tunes and my parents have supported me in everything I have ever done. Most of all I want to thank Silvia for being entirely unimpressed, amongst other things.

Contents

List of Figures

List of Tables

List of Symbols

Greek Symbols

Symbol	Units	Meaning
α	$^\circ\mathrm{C}^{-1}$	thermal expansion coefficient (general)
α_0	$^\circ\mathrm{C}^{-1}$	thermal expansion coefficient (linear equation of state)
β	psu^{-1}	haline contraction coefficient (general)
β_0	psu^{-1}	haline contraction coefficient (linear equation of state)
γ		rift-valley topographic slope; see p.54
ϵ	$\mathrm{m}^2\cdot\mathrm{s}^{-2}$	error variance of along-mean flow; see p.59
θ	$^\circ\mathrm{C}$	potential temperature
$\overline{\Delta\theta}$	$^\circ\mathrm{C}$	mean potential temperature deficit; see p.104
θ_2	$^\circ\mathrm{C}$	potential temperature referenced to 2000 dbar
$\Delta\theta_e$	$^\circ\mathrm{C}$	equilibrium-plume temperature anomaly; see p.99
$\overline{\Delta\theta_e}$	$^\circ\mathrm{C}$	mean equilibrium-plume temperature anomaly (c.f. $\Delta_\rho T$); see p.78
$\overline{\Delta\theta_i}$	$^\circ\mathrm{C}$	mean hydrothermal source temperature anomaly; see p.78
θ_z	$^\circ\mathrm{C}\cdot\mathrm{m}^{-1}$	vertical potential temperature gradient
κ		model parameter for outflow across multiple sills; see p.112
Λ		bulk-plume entrainment coefficient; see p.97
λ	m	horizontal wave length
μ		mean
ρ	$\mathrm{kg}\cdot\mathrm{m}^{-3}$	density
ρ_0	$\mathrm{kg}\cdot\mathrm{m}^{-3}$	reference density
ρ_b	$\mathrm{kg}\cdot\mathrm{m}^{-3}$	density of background water column; see p.97
ρ_i	$\mathrm{kg}\cdot\mathrm{m}^{-3}$	asymptotic hydrothermal source-fluid density; see p.99
ρ_k	$\mathrm{kg}\cdot\mathrm{m}^{-3}$	individual density measurement; see p.85

Symbol	Units	Meaning
σ		standard deviation
σ_2	$\mathrm{kg \cdot m^{-3}}$	potential density referenced to 2000 dbar
σ_θ	$\mathrm{kg \cdot m^{-3}}$	potential density referenced to the surface
σ_l	$\mathrm{m \cdot s^{-1}}$	standard deviation of along-mean flow; see p.58
σ_x	$\mathrm{m \cdot s^{-1}}$	standard deviation of cross-mean flow; see p.58
τ	days	analytic model solution time scale; see p.113
τ_l	days	integral time scale of along-mean flow; see p.58
χ^2		chi-squared merit function; see p.85
ω	$\mathrm{s^{-1}}$	frequency

Latin Symbols

Symbol	Units	Meaning
A	°C	regression coefficient of bilinear method; see p.85
A_ρ	$\mathrm{m^2}$	area of isopycnal surface; see p.104
B	$\mathrm{°C \cdot m^3 \cdot kg^{-1}}$	regression coefficient of bilinear method; see p.85
B_i	$\mathrm{m^4 \cdot s^{-3}}$	hydrothermal source buoyancy flux; see p.98
C	$\mathrm{°C \cdot V^{-1}}$	regression coefficient of bilinear method; see p.85
C_d		drag coefficient; see p.32
C_r		rotary coefficient; see p.56
c_p	$\mathrm{J \cdot kg^{-1} \cdot K^{-1}}$	specific heat
d	m	depth of model basin; see p.111
E		cross-valley section; see p.99
f	$\mathrm{s^{-1}}$	Coriolis parameter ($8.6 \times 10^{-5}\,\mathrm{s^{-1}}$ at 36°N)
G		topographic blocking parameter; see p.31
g'	$\mathrm{m \cdot s^{-2}}$	reduced gravity
H_c	W	conductive geothermal heat flux; see p.104
H_p	W	convective geothermal heat flux; see p.104

Symbol	Units	Meaning
h	m	vertical length scale
	m	in chapter 9: model interface height above outflow sill; see p.111
h_0	m	model interface height initial condition; see p.113
h_b	m	obstacle height; see p.31
h_{eq}	m	model-interface equilibrium height; see p.113
h_u	m	upstream interface height of hydraulic calculation; see p.33
K_v	$m^2 \cdot s^{-1}$	diapycnal diffusivity
k_l	m^{-1}	along-slope wave number; see p.54
k_x	m^{-1}	cross-slope wave number; see p.54
l	m	horizontal length scale
	m	in chapter 9: length of model basin; see p.111
N	s^{-1}	buoyancy frequency
N_i	s^{-1}	buoyancy frequency upstream of obstacle; see p.31
Δn	V	nephelometry anomaly
$\Delta_r n$	V	residual nephelometry anomaly; see p.93
Δn^*	V	peak value of Gaussian nephelometry plume; see p.69
P		sill friction parameter; see p.32
Q	$m^3 \cdot s^{-1}$	volume flux
Q_e	$m^3 \cdot s^{-1}$	equilibrium-plume volume flux; see p.78
Q_i	$m^3 \cdot s^{-1}$	hydrothermal source volume flux; see p.78
	$m^2 \cdot s^{-1}$	in chapter 9: model inflow (forcing term); see p.111
Q_i^*	$m^3 \cdot s^{-1}$	observed inflow into segment; see p.113
Q_o	$m^2 \cdot s^{-1}$	model outflow; see p.111
Q_o^*	$m^3 \cdot s^{-1}$	observed outflow from segment; see p.113
Q_u	$m^2 \cdot s^{-1}$	volume flux across model interface; see p.111
R_ρ		water-column stability ratio; see p.78
R_ρ^i		hydrothermal source density-anomaly ratio; see p.78
Ro		Rossby number; see p.34
r		correlation coefficient of linear regression
r_{BC}		cross-correlation coefficient of bilinear method; see p.86

Symbol	Units	Meaning
S	psu	salinity
$\overline{\Delta S_i}$	psu	mean hydrothermal source salinity anomaly; see p.78
$\Delta_\rho S$	psu	isopycnal salinity anomaly; see p.80
S_+	$\mathrm{m^2 \cdot s^{-2}}$	anticlockwise-polarized flow spectral energy; see p.56
S_-	$\mathrm{m^2 \cdot s^{-2}}$	clockwise-polarized flow spectral energy; see p.56
S_0	psu	reference salinity
S_b	psu	salinity of background water column
S_z	$\mathrm{psu \cdot m^{-1}}$	vertical salinity gradient
s		analytic model solution; see p.114
s'		analytic model solution; see p.114
T	°C	temperature
$\Delta_\rho T$	°C	isopycnal temperature anomaly (c.f. $\overline{\Delta\theta_e}$); see p.80
$\Delta_S T$	°C	isohaline temperature anomaly; see p.81
T_0	°C	reference temperature
T_r	days	current-meter record length; see p.59
U	$\mathrm{m \cdot s^{-1}}$	horizontal velocity
$\overline{U}$	$\mathrm{m \cdot s^{-1}}$	mean horizontal velocity
U_0	$\mathrm{m \cdot s^{-1}}$	reference velocity
U_i	$\mathrm{m \cdot s^{-1}}$	velocity upstream of obstacle; see p.31
U_n	$\mathrm{m \cdot s^{-1}}$	equilibrium-plume advection velocity; see p.99
W	$\mathrm{m \cdot s^{-1}}$	vertical velocity
w	m	width of hydraulic overflow current; see p.33
	m	in chapter 9: model-basin width; see p.113
X	$\mathrm{m^2}$	cross-sectional area of time-averaged buoyant plume; see p.97
z^*	m	maximum plume rise height; see p.98
z_0	m	reference depth

Chapter 1

Introduction

1.1 Motivation

The mid-ocean ridge system is the largest mountain chain of the Earth, spanning the entire globe with a total length of over 60×10^3 km and rising to a typical height of 3 km above the abyssal basins of the ocean. It marks the constructive boundaries between tectonic plates where hot material rises from the asthenosphere forming new oceanic lithosphere (e.g. *Fowler,* 1990). One of the principal parameters characterizing mid-ocean ridges is the spreading rate of the underlying plate boundaries. Together with the magma supply it determines the cross-axial morphology (e.g. *Macdonald et al.,* 1991). Most slow-spreading ridges such as the Mid-Atlantic Ridge (MAR) are characterized by rough topography and deep (1–3 km) median (or rift) valleys while fast-spreading ridges are smoother and lack deep valleys. Mid-ocean ridges are not continuous in the along-axis direction. At more or less regular intervals the ridge axes are laterally offset by transform faults and non-transform discontinuities separating the ridges into individual segments. Transform faults are generally associated with deep cross-axial valleys which connect the ridge axes to the open ocean. Neighboring transform faults are typically a few hundreds of kilometers apart. Non-transform discontinuities are characterized by lateral offsets which are smaller than the width of the ridges (< 30 km). Because most such discontinuities occur at depth maxima the rift valleys of slow-spreading ridges are often (partially) blocked between segments. Typical distances between neighboring non-transform discontinuities are a few tens of kilometers.

The water column overlying the rough topography of mid-ocean ridge systems is associated with greatly enhanced levels of diapycnal mixing (e.g. *Polzin et al.,* 1997), which is required

to balance the convective deep-water formation, thereby closing the global circulation (e.g. *Munk,* 1966). The processes giving rise to the enhanced mixing are not well known but it has been inferred that approximately half of the total energy required can be derived from astronomical tides interacting with the topography *(Munk and Wunsch,* 1998). Strong vertical shear associated with hydraulically controlled overflows is also known to greatly enhance diapycnal mixing (e.g. *Wesson and Gregg,* 1994; *Polzin et al.,* 1996). While it has been hypothesized that canyons on the flanks of mid-ocean ridges are locations where much of the diapycnal fluxes take place *(Polzin et al.,* 1997; *Ledwell et al.,* 2000) the role of the rift valleys of slow-spreading ridges has not been investigated in this context.

The young lithosphere near mid-ocean ridge axes gradually looses its excess heat to the water column. Comparison of oceanic heat flow measurements with thermal models indicate that, in addition to conductive cooling, a large amount of the heat is transferred by hydrothermal circulation (see *Lowell et al.* (1995) for a historical review and *Stein and Stein* (1994) for a recent evaluation of current models and estimates). The most spectacular manifestations of hydrothermal circulation are the high-temperature vent fields which give rise to particle-rich plumes rising hundreds of meters above the seafloor where they spread laterally into the surrounding water column. In addition to the resulting hydrographic anomalies and the corresponding dynamical responses, hydrothermal processes have profound effects on ocean chemistry and biology. For some chemical species hydrothermal circulation constitutes a source of similar magnitude to riverine input, while particle precipitation in hydrothermal plumes removes others (e.g. *Elderfield and Schultz,* 1996). The input of heat and chemicals also supports distinct and fascinating ecosystems (e.g. *Tunnicliffe,* 1991). To assess the impact of hydrothermal processes the fluxes associated with individual vent fields must be quantified.

The dispersal and fluxes of hydrothermal plumes in the rift valley of the MAR have been the focus of a number of studies (see section 1.3.2 for a detailed review). Most of the attention has been directed at the immediate vicinity of the vent fields, usually with the main emphasis on plume-driven dispersal. Inter-segment dispersal has received little attention and dispersal beyond the rift valley appears not to have been investigated at all, possibly because of the apparent lack of basin-scale hydrothermal signatures in the Atlantic (e.g. *Talley and Johnson,* 1994). (Recently, hydrothermal helium *(Roether et al.,* 1998; *Rüth et al.,* 2000) and methane *(Rehder et al.,* 1999) anomalies have been reported in the vicinity of the MAR crest, however.)

The dispersal of hydrothermal plumes is closely linked to the biological colonization pathways between vent fields (e.g. *Kim and Mullineaux,* 1998).

The following main questions are addressed in this thesis:

1. What are the dominant processes determining the hydrography and flow within the rift valley of the MAR?

2. What role do conductive geothermal heating and hydrothermal circulation play in this context?

3. Which processes (plume-driven, topographic, etc.) control the segment-scale dispersal of hydrothermal plumes?

4. How are hydrothermal tracers and biota dispersed between segments and how do they exit the rift valley?

5. What are the impacts of rift-valley processes on larger scales?

While some of these questions (especially 4 and 5) require much more investigation than is possible in the context of a thesis an attempt is made at providing answers by studying data from the rift valley of two connected segments of the MAR containing a large hydrothermal vent field. It is expected that some of the insights gained will be applicable elsewhere.

The data sets analyzed here were collected in the course of the *FLAME* (Fluxes at *AMAR* Experiment) project *(German et al.,* 1995), the goal of which is to perform a comprehensive study of the physical, geochemical and biological processes associated with the dispersal of the effluents rising from the largest (in terms of the lateral extent of the non-buoyant plume) known hydrothermal site of the MAR, located within the rift valley near 36°15′N. The project was set up in the framework of the *AMORES EC MAST III* program.

1.2 Thesis Outline

In the remainder of the introduction the background relevant for the investigation of the hydrography and dynamics within the rift valley of the MAR (section 1.3.1) and for hydrothermal dispersal and flux calculations (section 1.3.2) is reviewed. (Additional background concerning the interpretation of hydrothermal particle plume signatures and hydrographic

anomalies is reviewed in the introductions to chapters 5 and 6.) The study site is described in sections 1.3.3 and 1.3.4. The data sets and methods are presented in chapter 2.

In the following three chapters the hydrographic (chapter 3), current-meter (chapter 4), and particle-plume observations (chapter 5) are analyzed and interpreted. In chapter 6 two new methods for calculating hydrographic anomalies associated with hydrothermal particle plumes are developed and applied to the *FLAME* data sets. Combining the hydrographic, dynamical and plume observations, heat flux estimates are derived in chapter 7.

In chapter 8 mass and heat budgets of the rift valley are used to asses the importance of geothermal heating, to investigate the pathways of the rift-valley water, and to estimate bulk diapycnal diffusivities. In chapter 9 a simple model for the flow within the rift valley is developed.

The thesis ends with a summary of the main findings and conclusions, followed by a discussion (and some speculation) regarding their implications (chapter 10). There are no appendices. (Some of the work presented here has recently been accepted for publication by *JGR–Oceans (Thurnherr and Richards,* 2000); the sections covered in the paper are 2.1, 3.2, 5.2, and 7.3).

1.3 Background

1.3.1 Rift-Valley Hydrography and Flow

The first systematic study of the segment-scale hydrography within the median valley of the MAR was carried out by *Saunders and Francis* (1985). They reviewed 27 temperature profiles taken in the rift valley of 7 segments between 43°N and 47°N and report the following observations:

- the density stratification within the rift valley is reduced in comparison to profiles taken over the ridge flanks;
- the near-bottom temperatures within short segments show variations of order 0.02°C;
- the near-bottom temperature of a long (≈120 km) segment is characterized by a unidirectional gradient of order 0.1°C;
- differences between the near-bottom temperatures of adjacent segments are as high as 0.4°C;

- the lowest temperature observed in each segment is similar to the temperature in the off-ridge water column at the depth of the lowest nearby sill which connects the rift valley to the ridge flank.

From these observations *Saunders and Francis* (1985) infer that the water in the rift valley is renewed by hydraulically controlled inflows across sills near the locations where the coldest water is found. They investigate a number of different processes which can potentially provide the density flux within the segments to balance the inflows and conclude that the most likely scenario is alternating inflow events and periods of homogenization caused by diapycnal mixing (tidal stirring). They discount geothermal heating as an unlikely primary driving mechanism for the renewal of the rift-valley water because of the episodic nature of volcanic eruptions and hydrothermal circulation. (At the time of their investigation no hydrothermal vent fields had been discovered on the MAR, whereas subsequent studies have shown that hydrothermal circulation is not uncommon in the rift valley; e.g. *German and Parson,* 1998.) Reduced rift-valley stratification has been observed elsewhere on the MAR (e.g. *Rona and Speer,* 1989). In one case this was attributed to stirring and heating associated with a hydrothermal vent field *(Murton et al.,* 1999).

Wilson et al. (1995) also investigated the hydrography within (and overlying) the rift valley of the MAR. Because they contoured their sections across segment boundaries their data, which covers the segments between 33°N and 40°N, is difficult to evaluate in the context of the findings of *Saunders and Francis* (1985). Nevertheless, fig. 3 of *Wilson et al.* (1995) shows along-valley sloping isotherms and isopycnals in a number of segments, most notably between 35.6°N and 37.1°N which encompasses the segments investigated here. There are other studies containing hydrographic data from the MAR rift valley, but these are usually either single profiles from meridional sections across the ridge (e.g. *Roemmich and Wunsch,* 1985) or profiles taken in the immediate vicinity of hydrothermal vent fields, selected to show the hydrographic signatures of the buoyant and non-buoyant plumes (e.g. *Rona and Speer,* 1989; *Rudnicki and Elderfield,* 1992).

There are few investigations of physical processes within the MAR rift valley which are not directly related to hydrothermal plumes. *Rudnicki et al.* (1994) analyzed the temporal variability of the hydrography at the TAG hydrothermal site near 26°N over a semi-diurnal tidal cycle. They show vertical excursions of the isopycnal surfaces of the order of 100 m consistent with the semi-diurnal tidal frequency, and cite current meter observations indicating

that the semi-diurnal tidal currents of order $0.1\,\mathrm{m\cdot s^{-1}}$ dominate the flow energy. Additional rift-valley current meter observations were made at the *Broken Spur* hydrothermal site near 29°N. *Murton et al.* (1999) report low-pass filtered along-valley flow velocities peaking at $0.08\,\mathrm{m\cdot s^{-1}}$ and containing numerous flow reversals during the 225 days of sampling, while 19 days' worth of data from a different array of instruments deployed during another time in the same segment show the flow to be dominated by the semi-diurnal tidal currents peaking at 0.05–$0.1\,\mathrm{m\cdot s^{-1}}$ *(Lukashin et al.,* 1995). Finally, observations from the *Lucky Strike* hydrothermal site near 37°N indicate that the flow was dominated by semi-diurnal tidal currents of up to $0.23\,\mathrm{m\cdot s^{-1}}$, and the residual of order $0.03\,\mathrm{m\cdot s^{-1}}$ was predominantly parallel to the ridge axis and reversed its direction twice during the first 3 months of data collection *(Jean-Baptiste et al.,* 1998).

1.3.2 Hydrothermal Plume Dispersal and Fluxes

"Typical" hydrothermal vent fields consist of a number of vent chimneys, each with one or more orifices from which high-temperature ($\approx$350°C) effluents rise into the water column. At such high temperatures the equation of state of sea water (the main constituent of the hydrothermal effluents) is highly non-linear *(Bischoff and Rosenbauer,* 1985). Sub-surface boiling and phase-separation resulting in spatial heterogeneity of the effluents of a single vent field may also occur, depending on the sub-surface pressures and temperatures (e.g. *Von Damm,* 1995). Rapid initial cooling results in precipitation of metal sulfides and oxides so that high-temperature buoyant plumes take on the appearance of rising "smoke" (e.g. *Converse et al.,* 1984). The (time-averaged) temperatures in the plumes are reduced to near-ambient values close to the vent orifices and linear equations of state can be used *(Turner and Campbell,* 1987). Laboratory investigations of buoyant plumes show high variability at any distance from the source (e.g. *Papantoniou and List,* 1989), indicating that models of integrated or "bulk" plumes (e.g. *Morton, Taylor, and Turner,* 1956) should not be compared to individual profiles. The rising buoyant parcels of diluted hydrothermal effluents mix with background water and eventually reach a level where they are in equilibrium with the background density field and start dispersing along isopycnal surfaces, possibly after some vertical momentum-driven "overshoot" (where plume fluid is detrained, c.f. *Abraham and Eysink,* 1969). In the absence of other effects, lateral plume spreading is restricted by the Earth's rotation limiting the diameter of the equilibrium plumes to the order of the relevant

Rossby radius *(Helfrich and Speer,* 1995). The rise height of starting plumes in stagnant backgrounds is also affected by the Earth's rotation if the buoyancy sources persist for longer than an inertial period because of the cyclonic circulation set up around the buoyant plumes *(Speer and Marshall,* 1995). (The extensive literature on turbulent jets and plumes (e.g. *Turner,* 1973; *Fischer,* 1979; *List,* 1982) and on observed and modeled properties of hydrothermal plumes (e.g. *Helfrich and Speer,* 1995; *Speer and Helfrich,* 1995; *Lupton,* 1995) is not reviewed in detail here.)

In addition to the focused high-temperature flows, lower-temperature hydrothermal effluents not associated with strong particle anomalies percolate through the walls of vent edifices and through porous sediments, and rise as small plumes from cracks and fissures in the vicinity of the "smoker" chimneys. There are observations (e.g. *Rona and Trivett,* 1992; *Schultz et al.,* 1992) and at least one model *(Schultz and Elderfield,* 1997) which indicate that the fluxes associated with this "diffuse" hydrothermal constituent can be an order of magnitude larger than the high-temperature fluxes in the same vent fields but the range of ratios is unknown and the partition of the total fluxes between "focused" and "diffuse" is an open problem (see below).

Hydrothermal effluents are characterized by a range of anomalous hydrographic and chemical properties with respect to the background water column (e.g. *Von Damm,* 1995). One of the principal goals of hydrothermal research is to quantify the chemical and physical fluxes associated with hydrothermal circulation. Direct measurement (e.g. *Converse et al.,* 1984; *Schultz et al.,* 1992; *Ginster et al.,* 1994) is both costly (involving manned submersibles) and difficult because of the distributed nature of the sources. Particle anomalies, some chemical anomalies, and sometimes even hydrographic anomalies associated with the high-temperature hydrothermal plumes can be easy to detect in the water column, on the other hand. Hydrothermal fluxes are therefore often estimated from dispersal observations of the non-buoyant plumes. Because it is not clear to what extent the effluents of the "diffuse" hydrothermal constituent are entrained into the high-temperature plumes the calculated values may not represent the total fluxes. Heat-flux estimates from the Endeavor segment of the Juan de Fuca Ridge, for example, span two orders of magnitude *(McDuff,* 1995) with high values derived from non-buoyant plume surveys *(Baker and Massoth,* 1987; *Thomson et al.,* 1992) and low ones from direct measurements at the vent orifices *(Bemis et al.,* 1993). This is consistent with a large "diffuse" constituent entrained into the high-temperature plumes

but buoyant-plume measurements *(Ginster et al.,* 1994) do not support this view. Non-entrainment of "diffuse" effluents has also been inferred from observations at other sites (e.g. *Rona and Trivett,* 1992; *Trivett and Williams,* 1994).

A widely used method for estimating the fluxes associated with non-buoyant hydrothermal plumes is based on the calculation of tracer fluxes across vertical sections *(Baker and Massoth,* 1987). The large uncertainties generally associated with this method reflect uncertainties in the mean tracer and velocity distributions across the sections (e.g. *McDuff,* 1995). Determining mean tracer distributions is complicated by spatial (e.g. *Baker and Massoth,* 1987; *Lavelle,* 1997) and temporal (e.g. *Converse et al.,* 1984; *Schultz et al.,* 1992) variability of the hydrothermal circulation, and by the inherent heterogeneity of turbulent plumes. These problems are sometimes exacerbated by poor sampling coverage (e.g. *Baker et al.,* 1999). In the case of heat flux calculations from hydrographic anomaly fluxes the problem is compounded by uncertainties as to how the anomalies should be defined in the first place (e.g. *Thomson et al.,* 1992). Uncertainties in the advection velocities are caused by spatial and temporal variability (e.g. *Thomson et al.,* 1992; *Rudnicki et al.,* 1994).

An alternative method for calculating hydrothermal fluxes from non-buoyant plume observations consists in estimating the source buoyancy fluxes by matching the height-of-rise of buoyant plume models to the observations (e.g. *Rudnicki and Elderfield,* 1992). (The detailed assumptions depend on the plume model used. Because there are currently no numerical models which can resolve buoyant plumes rising from multiple time-varying sources into turbulent, sheared backgrounds, the most commonly used models are derived from that of *Morton, Taylor, and Turner* (1956), extended to allow for separate temperature and salinity buoyancy effects and sometimes also for uniform crossflows (e.g. *Middleton and Thomson,* 1986).) Hydrothermal fluxes can be calculated from the resulting buoyancy flux estimates and effluent property measurements. This method has been applied primarily to Atlantic hydrothermal plumes, possibly because the background hydrography of the rift valley can be too complicated to allow the quantification (or even detection) of the hydrographic anomalies associated with the hydrothermal plumes (e.g. *Wilson et al.,* 1996). The simplifying assumptions underlying the height-of-rise method together with its sensitivity to the observed parameters (height-of-rise, background hydrography) give rise to the large uncertainties associated with this method (e.g. *Speer and Helfrich,* 1995).

Hydrothermal fluxes can also be estimated from geochemical anomaly ratios in the plumes;

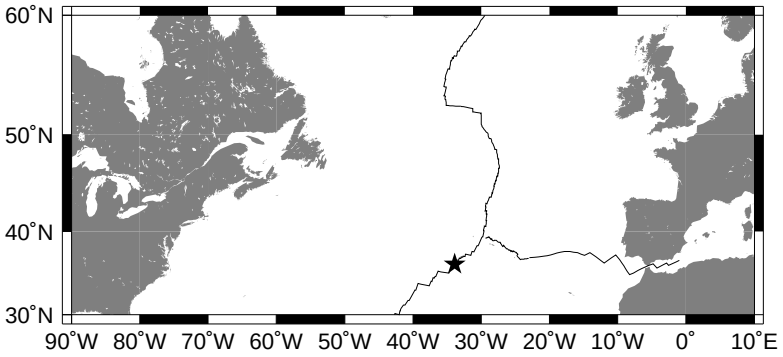

Fig. 1.1: Location of the *AMAR* segments (star); solid lines indicate the boundaries between the European, African and North American tectonic plates.

this method is associated with large uncertainties as well (see *Elderfield and Schultz* (1996) for a discussion).

Heat fluxes have been calculated for a number of Atlantic hydrothermal vent fields. At *TAG* near 26°N different applications of the height-of-rise method resulted in estimates of 500–940 $\times 10^6$ W *(Rudnicki and Elderfield,* 1992) and 70 $\times 10^6$ W *(Rudnicki et al.,* 1994) (a buoyant-plume method yielded 10 $\times 10^6$ W at the same site; *Rona and Speer,* 1989). At *Broken Spur* near 29°N the height-of-rise method resulted in estimates of order 50 $\times 10^6$ W *(James et al.,* 1995) while a heat budget calculated from current meter and temperature records yielded 275 $\times 10^6$ W *(Murton et al.,* 1999). The height-of-rise method applied to the *Lucky Strike* hydrothermal plume near 37°N resulted in an estimate of 120–400 $\times 10^6$ W *(Wilson et al.,* 1996) while a heat flux calculation based on the ^{3}He flux in the non-buoyant plume and the helium-heat ratio measured in the high-temperature effluents yielded 2.5–5 $\times 10^9$ W *(Jean-Baptiste et al.,* 1998). Finally, *German et al.* (1996c) applied the height-of-rise method to plume observations from the *Rainbow* hydrothermal vent field (the site investigated here; section 1.3.4) resulting in an estimate of the order of 100 $\times 10^6$ W (c.f. chapter 7).

1.3.3 The *AMAR* Segments

Fig. 1.1 indicates the location of the *AMAR* (ALVIN Mid-Atlantic Ridge) segments of the MAR. Figs. 1.2 and 1.3 show their bathymetry extracted from two different data sets. (Because the data sets are mutually consistent they were combined e.g. for Fig. 2.2.) The rift valley runs from the southwest (SW) to the northeast (NE). The non-transform discontinuity near 36°15′N separates the ridge into two segments: *AMAR* to the NE and *South AMAR*

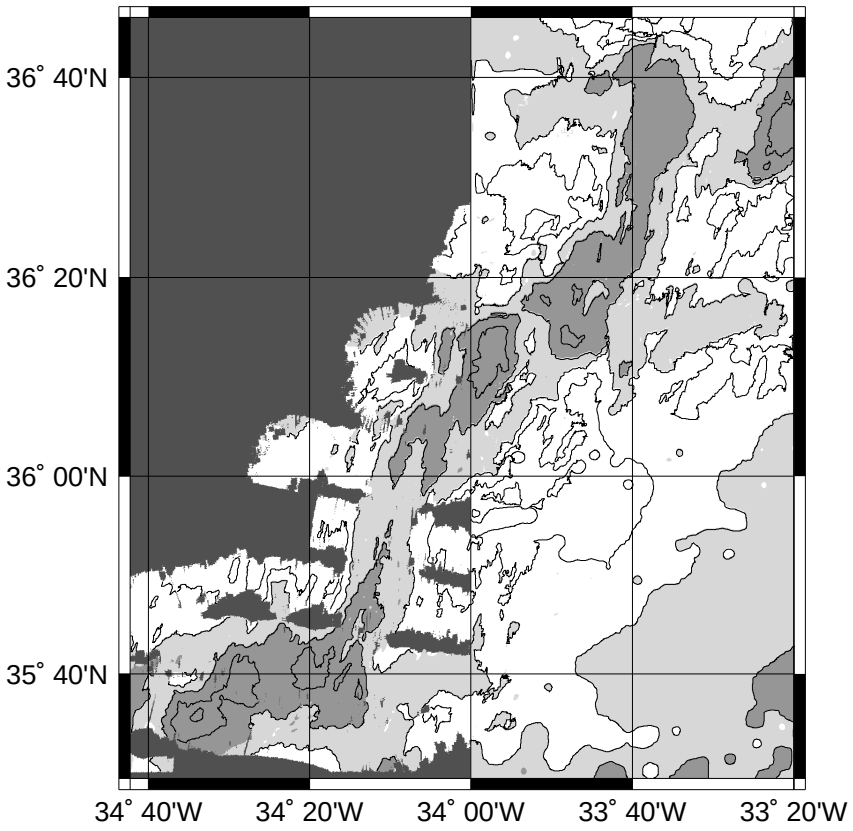

Fig. 1.2: High-resolution (nominally 100 m×100 m) *AMAR* bathymetry; intermediately dark shaded regions are deeper than 2500 m, lightly shaded regions are between 2000 m and 2500 m, and unshaded regions are less than 2000 m deep; contour interval is 500 m; dark shaded regions without contours are regions without data.

to the SW. The approximate lengths of the two segments are 100 km *(South AMAR)* and 50 km *(AMAR)*. *Detrick et al.* (1995) further subdivide *South AMAR* into three segments (PO-5, PO-6 and PO-7 in their terminology); PO-5 was previously called *AMAR Minor*, but subsequent sidescan sonar investigation has revealed no magmatic evidence to support this distinction as an additional ridge segment (C.R. German, *pers. comm.)*.

The rift-valley floor of the *AMAR* segments is characterized by a number of deep "basins" (defined here as depressions below 2500 m) connected by shallower regions. On both sides of the valley the walls rise to depths above 2000 m. Below 2000 m there is a sill connecting *South AMAR* to the *North Oceanographer* segment near 35°40′N/34°40′W (minimum depth 2200 m). North of *AMAR* the rift valley continues in the *FAMOUS* (French-American Mid-Ocean Undersea Study) segment, connected to *AMAR* at the sill near 36°35′N/33°30′W

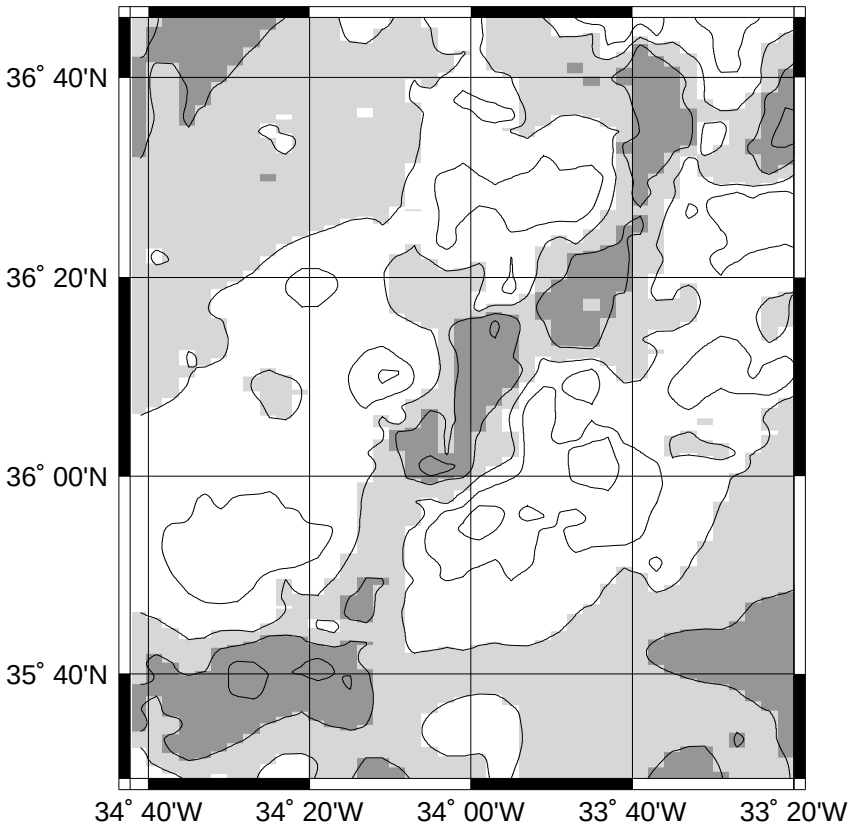

Fig. 1.3: *AMAR* bathymetry extracted from the *Smith and Sandwell* (1997) data set ($2' \times 2'$ resolution at the equator), derived from gravity anomalies constrained by ship tracks; shading and contours are the same as in Fig. 1.2.

(minimum depth 2200 m). Another sill near 35°35′N/34°10′W (minimum depth 2300 m) connects the *South AMAR* rift valley to the eastern ridge flank. There may also be a connection between the *AMAR* rift valley and the western ridge flank below 2000 m near 36°40′N/34°00′W but the available bathymetric data are ambiguous (neither data set indicates a connection below 2100 m, however).

1.3.4 The *Rainbow* Hydrothermal Vent Field

The *Rainbow* hydrothermal plume was discovered during a large-scale survey of the MAR near the non-transform discontinuity separating the *South AMAR* and the *AMAR* segments *(German et al.*, 1996b). There, the rift valley is blocked by a small ridge *(Rainbow Ridge;* minimum depth 1950 m) and an adjacent sill *(Rainbow Sill;* minimum depth 2500 m), separating it into a SW and a NE basin (Fig. 1.4). Based on water-column light-transmission

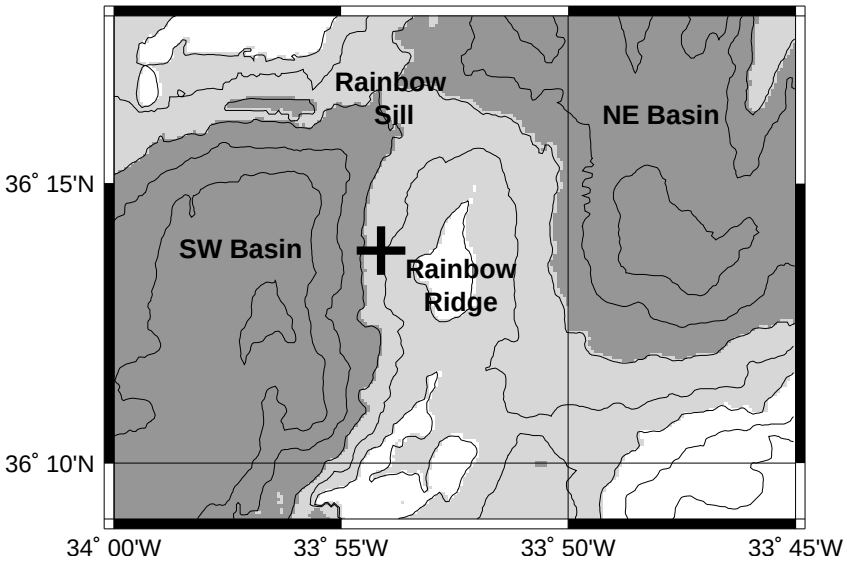

Fig. 1.4: *Rainbow* region bathymetry and nomenclature; shading is the same as in Fig. 1.2; contour interval is 250 m; the black cross near the 2250 m contour marks the location of the vent field; the two deep basins are part of the median valley running SW–NE; the unshaded regions in the SE and NW corner form part of the rift-valley walls.

anomalies, the site was chosen for a preliminary study using 7 CTD casts *(German et al.,* 1996c) and for testing the *BRIDGET* tow-yo platform which was used to map the hydrothermal plume over a horizontal extent of 10–15 km *(Rudnicki et al.,* 1995). The particle plume was observed to rise to a depth of 2000–2100 m, i.e. it was confined within the rift valley. Based on these observations the *FLAME* project (section 1.1) was initiated to investigate the hydrography, plume dynamics, chemistry, and biology of the *Rainbow* site. Preliminary findings from the first *FLAME* cruise (section 2.1) were reported by *German et al.* (1998). During a subsequent submersible dive the active hydrothermal vent field was discovered at a depth between 2270 m and 2320 m at 36°13.80′N, 33°54.12′W *(Fouquet et al.,* 1998).

Chapter 2

Data Sets and Methods

2.1 1997 Survey *(FLAME)*

In May/June 1997 the first of two cruises to the *AMAR* segments (the *FLAME* cruise) took place. Two different platforms were used to collect data at the stations shown in Fig. 2.1: *BRIDGET*, an instrument developed for deep tow-yo lines through hydrothermal plumes *(Rudnicki et al.,* 1995), and a standard CTD package. In addition to the CTD stations shown, two eastern (≈50 km off axis) and one western (≈100 km off axis) background stations were occupied for reference. Total sampling time was 24 days.

The *BRIDGET* platform was used to collect data between 1700 m and the sea bed by tow-yoing it at speeds not exceeding 1.5 knots. It was equipped with one and sometimes two self-contained *FSI MicroCTD* instruments, a *Chelsea Instruments Aquatracka* Nephelometer (measuring light-scattering at a 90° angle), as well as a 12-bottle sampling rosette and auxiliary instruments such as attitude sensors and an altimeter. The circles representing the *BRIDGET* tows in Fig. 2.1 show the locations of the intersections of the tow-yo lines with the 2100 m depth.

The CTD package was used for vertical profiles, a tow-yo, and a ten-hour yoyo. It was equipped with a *General Oceanics Neil Brown Mk3c CTD,* a *Chelsea Instruments Mk2 Subaquatracka* Nephelometer, a self-contained *RDI Acoustic Doppler Current Profiler* used as a lowered ADCP (LADCP), a 12-bottle sampling rosette, as well as auxiliary instruments such as an altimeter.

The temperature sensors of two of the three CTDs were pre-cruise calibrated (the remaining one was taken as a spare). The *Neil Brown CTD* was re-calibrated 10 months after

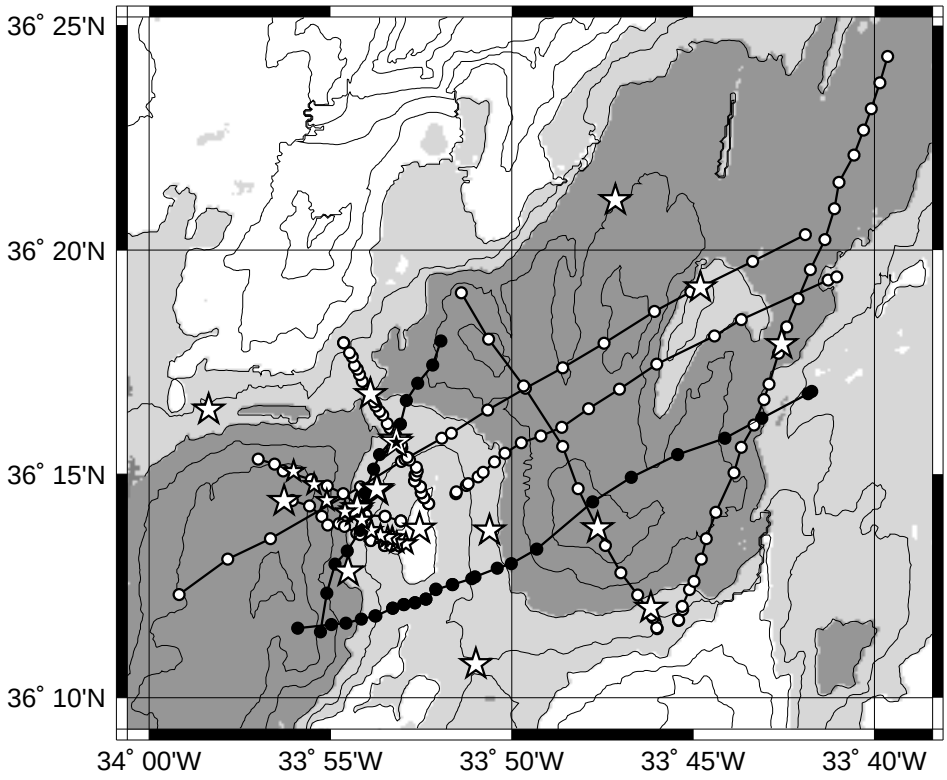

Fig. 2.1: *FLAME* stations; shading is the same as in Fig. 1.2; contour interval is 250 m; CTD stations are marked with stars and *BRIDGET* tow-yos with circles. The *BRIDGET* tows marked with black circles are the cross-sill tow of Fig. 3.11 and the cross-ridge tow of Fig. 3.12. The black star with a white border near *Rainbow Sill* indicates the position of the 10 h CTD yoyo (Fig. 3.13); the small stars on the western slope of *Rainbow Ridge* show the CTD tow-yo.

the cruise. Based on the calibration information and direct instrument comparison on the *BRIDGET* platform the temperature intercalibration error is estimated to be $\pm 10^{-2}$°C. At the mean plume depth (2100 m; see section 5.2) this corresponds to a density uncertainty of $\pm 2 \times 10^{-3}\,\mathrm{kg \cdot m^{-3}}$, the same order of magnitude as some of the important hydrographic patterns (e.g. Fig. 3.6). Therefore, data sets from different instruments were not combined. Because the CTD data set is essentially a spatial subset of the *BRIDGET* data set (Fig. 2.1), this is not a problem — the CTD data were used to verify the patterns observed in the *BRIDGET* data.

The conductivity sensor of the *Neil Brown CTD* was calibrated by analyzing 207 bottle samples with an *Ocean Scientific International AUTOSAL Model 8400A* salinometer, resulting in a RMS error of 2.7×10^{-3} psu. Because of hardware problems with one of the two

CTDs flown on *BRIDGET* not enough bottle samples were available to reliably calibrate either conductivity sensor. The salinity calibration of one of the CTDs that failed twice during the cruise was judged to be too unreliable to be used at all. Therefore, the measurements of that instrument were removed from the hydrographic data set. (The affected tows are not shown in Fig. 2.1.) A trend of 5.8×10^{-4} psu per day was removed from the data of the 2nd *BRIDGET* CTD. For calibration, the resulting T/S was fitted against the Neil Brown T/S. To assess the quality of this intercalibration, the result was compared to the 37 available AUTOSAL samples for the *BRIDGET* instrument resulting in a RMS error of 1.7×10^{-3} psu in the plume range (35–35.1 psu). This corresponds to a density uncertainty of $\pm 1.5 \times 10^{-3}\,\mathrm{kg \cdot m^{-3}}$.

Nephelometry values are usually reported in arbitrary units called "nephels" *(Nelsen et al.,* 1987); here, instrument voltage (V) is used. To remove the offset between the CTD and the *BRIDGET* nephelometers as well as the trends observed during long *BRIDGET* tow-yos (caused by lens-fogging), an offset was applied to the individual profiles by subtracting the mean value between 1500 m (or the upper turning point of the *BRIDGET* tow-yo profiles) and 1850 m (above the highest particle plume observations; section 5.2). This results in some negative nephel values. To compare the response characteristics of the two nephelometers the mean values ($\pm 1\sigma$) of the near-surface light-scattering maximum were compared; the resulting agreement between $0.15(\pm 0.05)$ V derived from 19 *BRIDGET* profiles and $0.14(\pm 0.03)$ V derived from 25 CTD profiles indicates that the (assumed linear) response characteristics of the two instruments are comparable.

The LADCP data presented here were derived from water-track data averaged over 5 m bins. In contrast to the data presented by *German et al.* (1998) no averaging between the up- and the downcasts was performed. Average layer velocities (e.g. Fig. 3.1) were derived by separately calculating the mean of the northward and eastward velocity components — this method may produce small values in dynamically active layers where velocity components take on both signs.

2.2 1998 Survey *(FLAME-2)*

In June/July 1998 the *AMAR* segments were revisited during the *FLAME-2* cruise, the main purpose of which was the recovery of eight moorings with 25 current meters deployed in

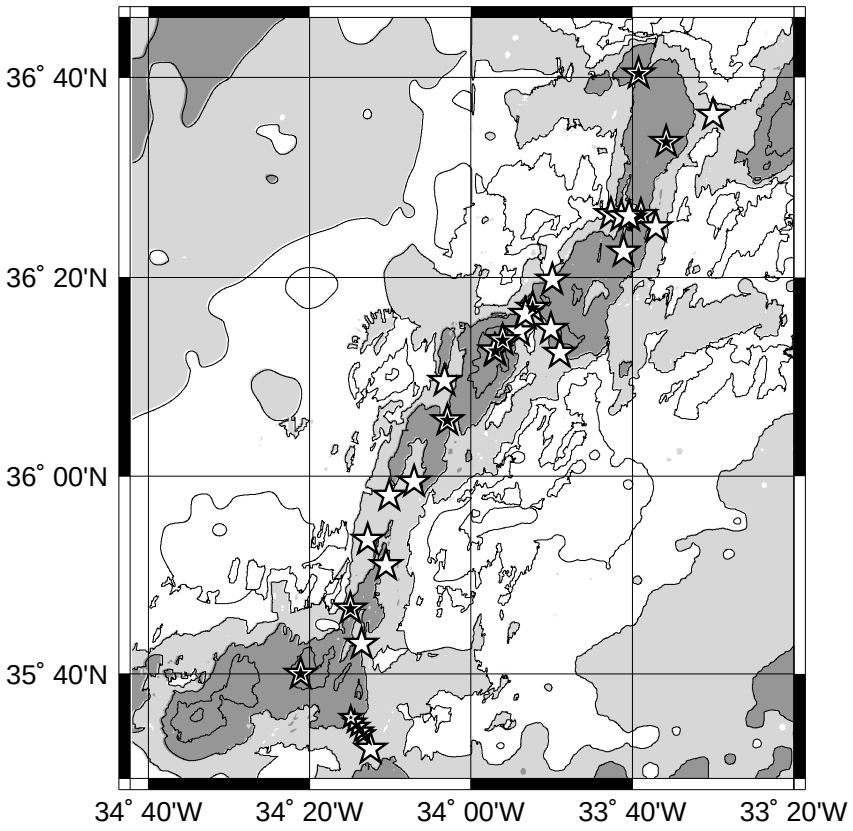

Fig. 2.2: *FLAME-2* CTD stations; shading is the same as in Fig. 1.2; contour interval is 500 m; full-depth CTD stations are marked with big stars; the small stars near 35°35′N/34°15′W show the bottom turning points of a CTD tow-yo (Fig. 3.19); black stars with white borders indicate profiles extending below 2550 m.

1997 (section 2.3). To investigate the low-frequency variability of the hydrography and of the particle plume the *Rainbow* region was re-sampled. Because of favorable weather conditions sampling was extended in both directions along the rift valley to cover the *South AMAR* and *AMAR* segments. Fig. 2.2 shows the locations of the tow-yo and the full-depth stations occupied during the 6 days of sampling. In addition to the stations shown, the eastern off-ridge background station of the *FLAME* cruise (section 2.1) was re-occupied for reference.

Because of instrument problems, two separate *Neil-Brown Mk.IIIb* CTDs were used on a platform which was also equipped with a *Sea Tech Light Scattering Sensor* (LSS), a 12-bottle sampling rosette, and auxiliary instruments such as an altimeter. The temperature sensor of one of the two CTDs was pre-cruise calibrated (the other instrument was taken as a spare).

To calibrate the temperature sensors, the first sampling bottle of the CTD rosette was

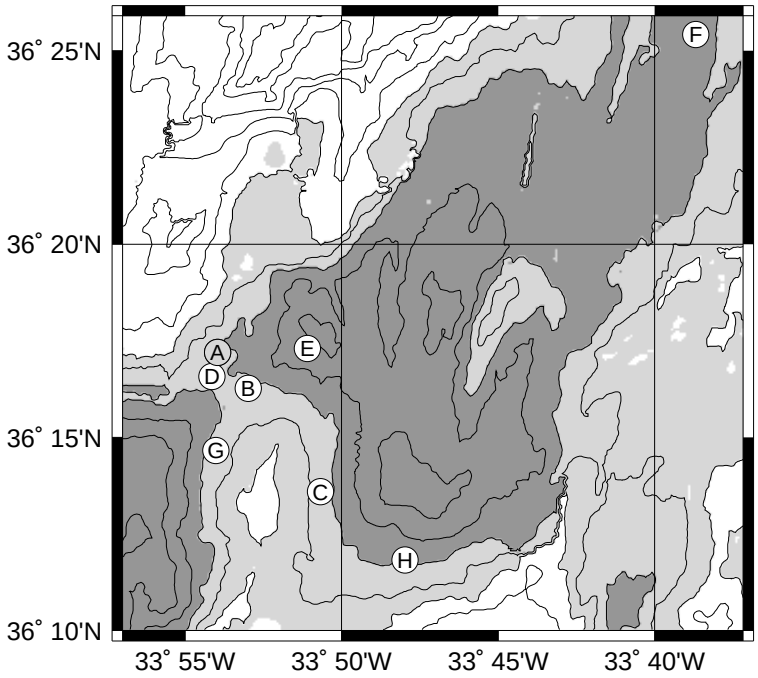

Fig. 2.3: Current-meter mooring positions; shading is the same as in Fig. 1.2; contour interval is 250 m; mooring "A" was not recovered.

fitted with two digital reversing thermometers, pre-cruise calibrated to $\pm 2 \times 10^{-3}$ °C. Near-bottom temperatures were recorded at 23 out of the 35 CTD stations. The average of the two thermometer readings was used for calibration. RMS errors of the temperature calibrations for the two CTDs are 1.2×10^{-3} °C and 1.5×10^{-3} °C, respectively.

The conductivity sensors of both CTDs were calibrated by analyzing 34 and 158 bottle samples with an *Ocean Scientific International AUTOSAL Model 8400A* salinometer, resulting in RMS errors of 1.8×10^{-3} psu and 3.3×10^{-3} psu, respectively. The conductivity sensor accuracy of $5 \times 10^{-6}\,\mathrm{S \cdot m^{-1}}$ corresponds to a salinity accuracy of 6×10^{-3} psu at 4°C and 3000 dbar.

The LSS was not calibrated and instrument voltage anomalies with respect to the observed mean between 1500 m and 1850 m are used as the "nephel" unit (c.f. section 2.1).

2.3 Current-Meter Moorings

2.3.1 Sensors and Data

Between July 1997 and July 1998 25 *Aanderaa RCM 8* current meters were deployed on 8 moorings (Fig. 2.3). Mooring "A" was not recovered successfully, leaving 7 moorings with three current meters each, nominally at 1800 m, 2100 m and 2300 m. All instruments had temperature sensors installed. The 2100 m current meters were additionally fitted with *Sea Tech Light Scattering Sensors* (LSS), and some also with pressure and/or conductivity sensors. Table 2.1 lists the instruments and information concerning their installed sensors and data quality. Velocity and temperature data from all instruments were recovered successfully. Flow speeds and directions were sampled every 72 s. Every hour the vector-averaged mean velocities and spot measurements from the other sensors were recorded. Total common record length is 372 days (53 weeks and 1 day).

After approximately 7 months of deployment all LSS records show an increasing trend followed by an abrupt (order 1 day) drop to zero followed approximately 10 days later by a sudden increase to ≈ 4 V (total range is 0–5 V). The most likely explanation for this behavior is a power drop of the instrument batteries (Aanderaa representative, *pers. comm.)*. Because it cannot be determined accurately which portions of the LSS records are contaminated by the instrument failures these data were not used at all.

All pressure records from the 2100 m instruments show sudden increases between 3 dbar and 150 dbar coinciding with the sudden LSS voltage increases. Because there are no coincident pressure changes in any of the other records, these signals are assumed to be contamination effects of the LSS failures. The remaining data (temperature, conductivity, speed and direction) do not show any clear indication for similar contamination — because of the variability of the data small calibration shifts cannot be excluded, however.

2.3.2 Calibrations

Speed: manufacturer-specified linear calibration.

Direction: first, a manufacturer-specified linear calibration was applied to map the raw data to the compass range. The compasses were calibrated before and after deployment at 10° intervals; because of the calibration procedure, differences between the two calibrations (nowhere greater than 10°) are more likely to be errors than shifts in the compass

Mooring	Depth	IID	LSS	Conductivity	Pressure
B	1770 m	B18	n/i	ok	ok
(2450 m)	2070 m	B21	bad	n/i	bad
	2270 m	B23	n/i	bad	ok
C	1840 m	C18	n/i	n/i	ok
(2400 m)	2140 m	C21	bad	ok	bad
	2340 m	C23	n/i	ok	ok
D	1805 m	D18	n/i	n/i	ok
(2520 m)	2105 m	D21	bad	n/i	bad
	2305 m	D23	n/i	n/i	n/i
E	1755 m	E18	n/i	n/i	ok
(2890 m)	2055 m	E21	bad	ok	bad
	2255 m	E23	n/i	partially bad	n/i
F	1720 m	F18	n/i	bad	ok
(2650 m)	2020 m	F21	bad	ok	bad
	2220 m	F23	n/i	ok	n/i
G	1830 m	G18	n/i	n/i	ok
(2410 m)	2130 m	G21	bad	ok	bad
	2330 m	G23	n/i	ok	n/i
H	1830 m	H18	n/i	n/i	ok
(2450 m)	2130 m	H21	bad	ok	bad
	2330 m	H23	n/i	ok	n/i

Table 2.1: Current-meter instrument list; water depths as recorded during mooring deployment are given in parenthesis beneath the mooring letters; "IID" denotes the instrument identifiers used in chapter 4; "LSS", "Conductivity", and "Pressure" columns indicate whether such sensors were fitted ("n/i" meaning "not installed") and the quality of the recovered data.

calibrations (P.G. Taylor, *pers. comm.)* — therefore, the more self-consistent of the two calibrations (based on the difference at neighboring calibration points) was applied. In a third step, the calibrated data were corrected for magnetic declination ($-15°$), calculated for $36°25'$N/$33°50'$W, January 1st 1998 with the *IGRF95* model *(IAGA*

Division V Working Group 8, 1995).

Pressure/Depth: in addition to the contamination of the 2100 m instruments caused by the LSS failures (section 2.3.1), many of the remaining pressure records also show trends and jumps of various magnitudes. Because these could nowhere be correlated between separate instruments on the same mooring they are all assumed to be sensor problems and the affected data were removed from the records. From the remaining data a mean offset to the nominal depth was calculated using both pre- and post-deployment calibrations. From these a common mean offset was estimated for each mooring and added to the nominal values to yield the depths listed in Table 2.1. For the analysis (chapter 4) the nominal depths (1800 m, 2100 m, 2300 m) are used exclusively.

Temperature: the sensors were calibrated both before and after the deployment; a number of the post-deployment calibrations were erroneous and were therefore re-done; the pre- and the repeated post-deployment calibrations differ by up to 0.5°C without any indication for similar sensor calibration shifts in the data but most are of order 0.03°C or less. Because the quality of the calibrations is somewhat doubtful and because the temperature records do not show any recognizable trends or shifts which could be corrected by taking the pre- to post-deployment calibration differences into account, it was decided to individually apply the calibrations which minimize the differences between the mean hydrography sampled during the *FLAME* cruise (section 2.1) and the mean temperatures calculated from the first week of each current-meter record. (Because of the variability of the hydrography on short time scales (section 3.2.3) no attempt was made to relate the temperature records to individual CTD profiles.) Both nominal and calibrated depths were used, with the calibrated depths resulting in smaller mean differences. The calibrated temperatures are all low-biased between 0.05°C and 0.08°C.

Salinity: In a first step, the raw conductivity data were plotted against time and the data sets marked "bad" (Table 2.1) where the conductivity sensors were not working. One instrument (E23) initially returned bad data — based on a visual assessment the data before deployment day 132 were removed. The remaining conductivity data were calibrated in the same way as the temperature records.

Chapter 3

Quasi-Synoptic Hydrographic and Flow Observations

3.1 Introduction

In this chapter the hydrographic and velocity data collected during the two quasi-synoptic surveys of the 1997 *FLAME* (section 2.1) and the 1998 *FLAME-2* (section 2.2) cruises are analyzed and interpreted. The main goal is to provide the hydrographic context for the analysis of the current-meter records (chapter 4) and of the hydrothermal plume signatures (chapters 5 and 6).

In section 3.2 the 1997 survey is presented. First, the regional hydrography above the MAR is analyzed, including the signatures of the Mediterranean water tongue and of the Azores Current. Within the rift valley the water column was less dense and stratified than both eastern and western off-ridge water, with T/S characteristics consistent with inflow across a sill from the east. The data from the rift valley west of *Rainbow Ridge* contain signatures consistent with interleaving of western off-ridge water above 2000 m. Below 2000 m, the rift-valley hydrography and dynamics were dominated by a hydraulically controlled NE-ward along-valley flow across *Rainbow Sill*. Large-amplitude internal waves consistent with tidal forcing were observed near the sill. Above 2000 m the mean flow across the topography generated lee waves which radiated energy upwards and downstream.

In section 3.3 the 1998 survey is presented. A comparison of the θ_2/S properties of the two surveys suggests that the rift-valley water was of the same origin in both years. No

σ_2	σ_θ	Depth	Relevance
36.20	27.37	780 m	top of Mediterranean outflow water
36.60	27.68	1120 m	Mediterranean water salinity maximum
36.82	27.79	1500 m	MAR crest
36.93	27.82	2000 m	"bifurcation depth" (section 3.2.3)

Table 3.1: Key depths and potential densities referenced to the surface (σ_θ) and to 2000 dbar (σ_2); σ-units are omitted.

interleaving of western water was observed in 1998. Below 3000 m the water had cooled by 0.06° C but at the depth of the current meters (1800–2100 m) no systematic temperature trend rises above the variability encountered during each survey. Direct velocity measurements indicate that the flow below 2100 m was similar in 1997 and 1998 but that it had reversed direction at 1800 m. Along-segment distributions of temperature, salinity and density below 2500 m are characterized by unidirectional gradients consistent with along-valley mixing but not with geothermal heating. Near the southern end of the segments hydrographic signatures of inflow from the eastern ridge flank were observed. The chapter concludes with a discussion in section 3.4.

3.2 1997 Survey *(FLAME)*

3.2.1 Regional Hydrography

The *AMAR* segments are located in a section of the MAR with a complex hydrography which is affected by the ridge topography, the Mediterranean water tongue and the Azores Current and Front (e.g. *Wilson et al.*, 1995). (For comparison with other studies some key potential densities referenced to 2000 dbar (σ_2) and to the surface (σ_θ), together with the associated depths estimated from the pressure-averaged CTD profile of the entire survey, are listed in Table 3.1.)

In full-depth hydrographic profiles the Mediterranean water tongue is immediately apparent as a region of nearly constant salinity in the θ_2 (potential temperature referenced to 2000 dbar) range of 7.5–9.5° C (e.g. Fig. 3.3 below). The mean salinity maximum of 35.42 psu has an associated potential density σ_2 of 36.6 kg·m^{-3} (σ_2 units will be omitted below). These

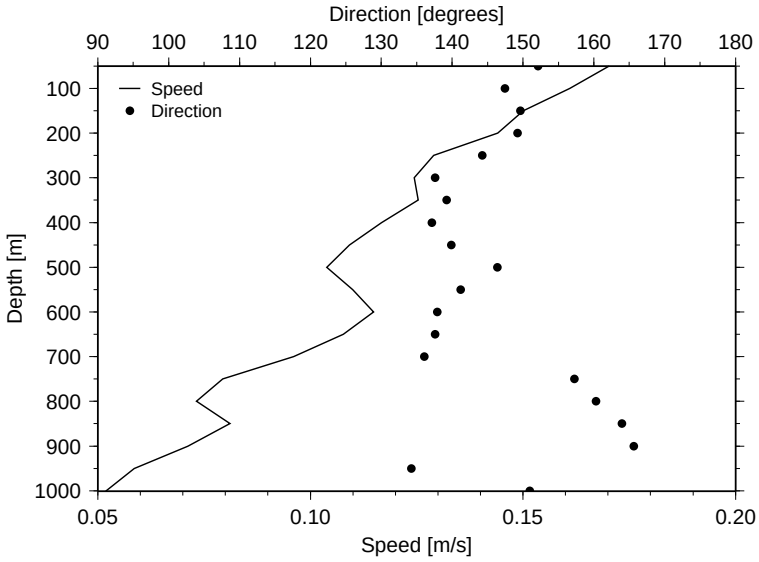

Fig. 3.1: Mean LADCP-derived flow speeds and directions in the top 1000 m of the water column; each data point represents a 50 m vertical mean.

values are consistent with published data of the Mediterranean water tongue in this region (e.g. *Sy,* 1988). The horizontal distribution of the Mediterranean outflow water can be traced as a wedge penetrating deep into the North Atlantic well beyond the MAR (e.g. fig. 69 of *Fukumori et al.,* 1991). According to *Sy* (1988), this wedge is bounded by two main branches of the Gulf Stream extension: the North Atlantic Current to the north ($\approx$46°N) and the Azores Current to the south. While the North Atlantic Current flows too far north to influence the *AMAR* segments, the latitude of the Azores Current near 34°W is not well defined. There is considerable evidence for meanders on a scale of at least 100 km (e.g. *Gould,* 1985; *Sy,* 1988; *Fernandez and Pingree,* 1996).

Fig. 3.1 shows the mean flow velocities in the top 1000 m of the water column, derived from the LADCP profiles of all CTD stations. The flow is mainly SE-ward with the speed decreasing nearly linearly from 0.17 $\mathrm{m \cdot s^{-1}}$ at the surface to 0.05 $\mathrm{m \cdot s^{-1}}$ at 1000 m. Below 1000 m the mean speed remains approximately constant down to the depth where the topography begins to influence the flow (see Fig. 3.10). The magnitude and vertical structure of the observed current are consistent with geostrophic calculations presented by *Gould* (1985) and by *Sy* (1988), both reporting velocities around 0.25 $\mathrm{m \cdot s^{-1}}$ at the surface decreasing nearly linearly to 0.05 $\mathrm{m \cdot s^{-1}}$ at 1000 m in the vicinity of the *AMAR* segments. *Gould* (1985) also proposes two criteria to assess if a given station lies north or south of the Azores Front, one

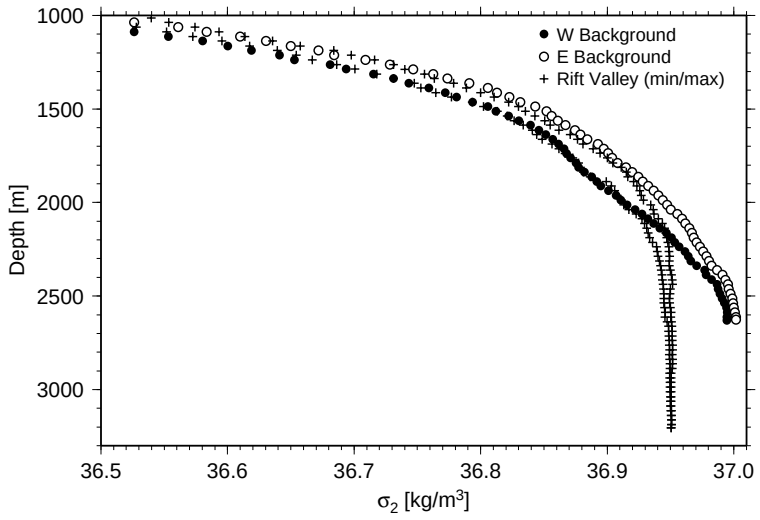

Fig. 3.2: CTD potential density profiles from the rift valley and from an eastern and a western off-ridge background station; at each depth both the minimum and the maximum densities of the rift-valley profiles are shown.

for the depth of the 15°C isotherm (less than 300 m with typical values around 100 m north of the front) and the other for the surface salinity (less than 36.4 psu with typical values near 36.2 psu north of the front). For the data of the 1997 survey the respective mean values are 280 m and 36.3 psu, indicating that the frontal region was sampled. The hydrography and current measurements of the *FLAME* cruise are therefore consistent with a SE-ward flowing meander of the Azores Current influencing the top 1000 m of the water column.

3.2.2 Origin of the Rift-Valley Water

Fig. 3.2 shows the potential density range (min/max) observed within the rift valley as well as density profiles of an eastern and a western background station. The stratification within the rift valley below 2200 m is reduced with respect to the ridge flanks, consistent with the observations of *Saunders and Francis* (1985). The two background profiles indicate a cross-ridge density gradient, bracketing the density range observed in the rift-valley profiles above 2000 m. The data of *Fukumori et al.* (1991) show a similar cross-ridge gradient. This density drop across the ridge axis implies that inflows into the rift valley across sills from the east are energetically favored.

Fig. 3.3 shows the pressure-averaged θ_2/S diagrams of the CTD stations of the NE and SW basins (Fig. 1.4) as well as those of two off-ridge reference stations. The rift-valley water

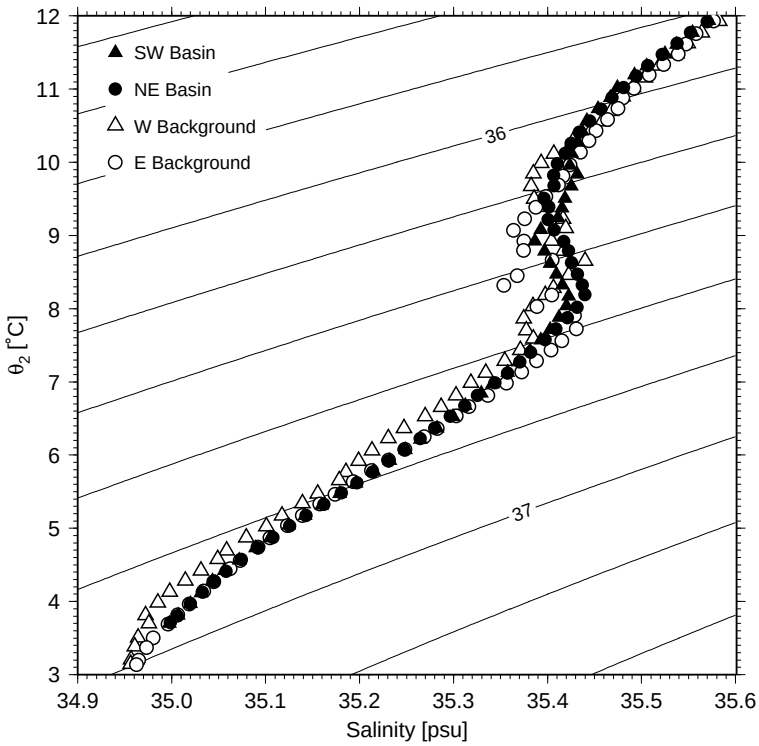

Fig. 3.3: θ_2/S diagram showing the mean water characteristics of the two deep basins on either side of *Rainbow Ridge* as well as the characteristics of an eastern and a western off-ridge background profile; potential density contours are referenced to 2000 dbar (σ_2), contour interval is 0.2.

characteristics are almost identical to those of the eastern off-ridge profile for $\sigma_2 > 36.7$ (below $\approx$1300 m) while there is a significant difference to those of the western background profile. Therefore, the valley water most likely originates east of the MAR as was previously asserted by *German et al.* (1998). The θ_2/S characteristics of the water in the two basins separated by *Rainbow Sill* are virtually identical, indicating that the deep water of both basins most likely has the same origin, consistent with the small range of potential densities observed in the rift valley below 2500 m (Fig. 3.2).

Individual CTD profiles indicate that the situation in the rift valley is not as simple as the mean hydrographic properties suggest (Fig. 3.4). Features such as the θ_2/S offset of approximately -0.1°C between 4.1°C (1975 m) and 4.5°C (1690 m) in the rift-valley profile are common in the SW basin. In the NE basin they are not observed away from the eastern slope of *Rainbow Ridge* (i.e. east of 33°50′W). In profiles with hydrothermal plume signatures (section 5.2) such structures occur higher up in the water column than the light-scattering

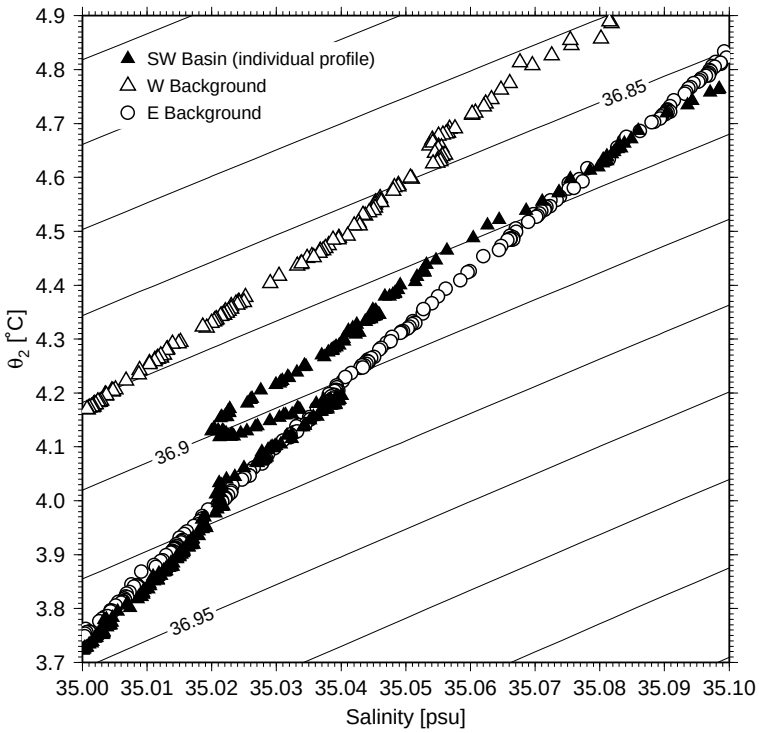

Fig. 3.4: θ_2/S diagram showing interleaving of cold/fresh water between 1720 m and 1920 m in a profile from the SW basin; σ_2 contour interval is 0.025.

peaks, indicating that these hydrographic offsets are not caused by hydrothermal processes. Because there is no evidence for additional water masses in this region the non-hydrothermal θ_2/S offsets are assumed to be caused by interleaving of western off-ridge water as noted by *German et al.* (1998). The depth and horizontal distribution of the interleaving structures suggest a possible pathway for western water to intrude into the rift valley across a sill near 36°25′N/34°10′W (Fig. 1.3).

3.2.3 Rift-Valley Hydrography and Flow

Horizontal Density Distribution

Fig. 3.5 shows the horizontal distribution of potential density at 2200 m, i.e. at an intermediate depth between the peak of *Rainbow Ridge* (1950 m) and the saddle of *Rainbow Sill* (2500 m). The shading of each cell is determined by the pressure-averaged *BRIDGET* density measurements within its boundaries, with darker shades indicating higher densities. At 2200 m the SW basin water is generally denser than the NE basin water. It is not clear if the

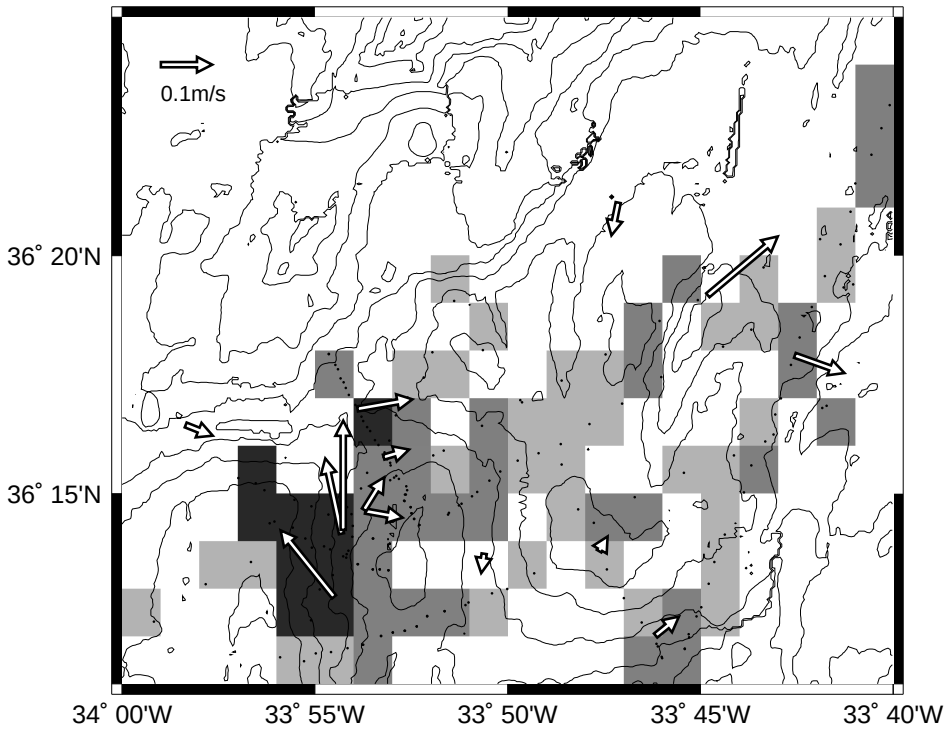

Fig. 3.5: Horizontal density distribution and instantaneous LADCP velocity measurements (arrows) between 2175 m and 2225 m; bathymetric contour interval is 250 m; lightly shaded cells indicate below-average potential densities, darkly shaded cells are more than one standard deviation ($\approx 3 \times 10^{-3}$) denser than the mean, and intermediately shaded cells lie in between.

high-density water is confined to the northeastern part of the SW basin because the lightly shaded cells found in the remainder of the basin are all derived from few data points from single *BRIDGET* lines.

Fig. 3.6 shows the pressure-averaged potential density profiles of the two deep basins and *Rainbow Sill*. The horizontal density difference between the basins has a maximum value of 4.5×10^{-3} near 2250 m. The different slopes of the density profiles between 2000 m and 2250 m indicate that, on average, the isopycnals in this depth range are more spread in the NE basin than in the SW basin. This is confirmed by the corresponding buoyancy frequency profiles (Fig. 3.7). The stratification below 2400 m is too weak to be resolved accurately. An estimate of $10^{-4}\,\mathrm{s}^{-1}$ is used below for the SW basin buoyancy frequency at 2500 m.

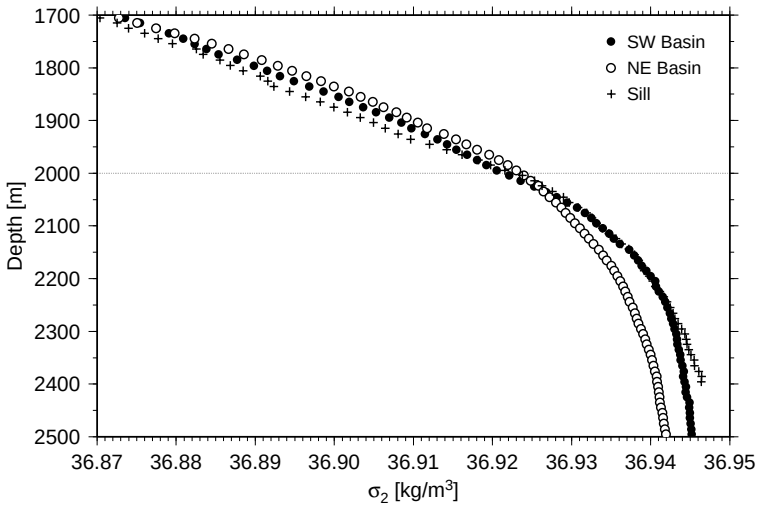

Fig. 3.6: Pressure-averaged potential density profiles of the SW basin, *Rainbow Sill*, and the NE basin; the dotted line at 2000 m indicates the depth below which the density profiles diverge (see also Fig. 3.7).

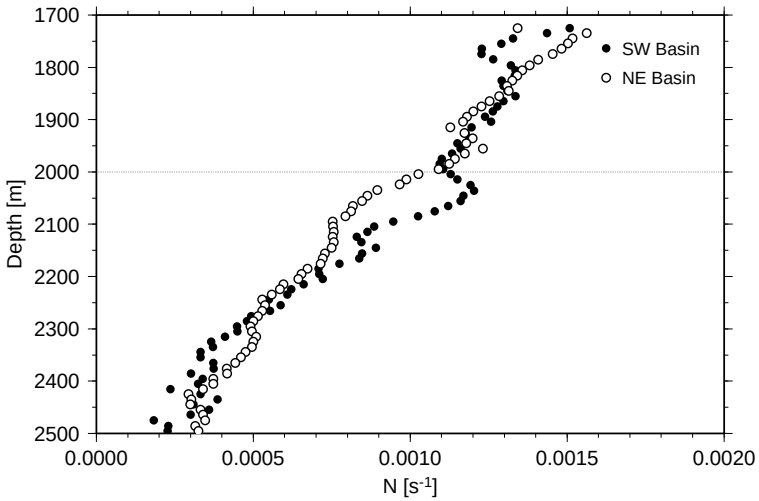

Fig. 3.7: Pressure-averaged buoyancy frequency profiles of the SW and the NE basins; the dotted line is the same as in Fig. 3.6.

Direct Flow Observations

In addition to the density distribution, Fig. 3.5 also shows the LADCP current measurements at 2200 m. The two main features to note are the consistent clockwise flow around the northern tip of *Rainbow Ridge* (the individual measurements were taken over a period of three weeks) and the large velocities observed on its western slope. Fig. 3.8 shows the current

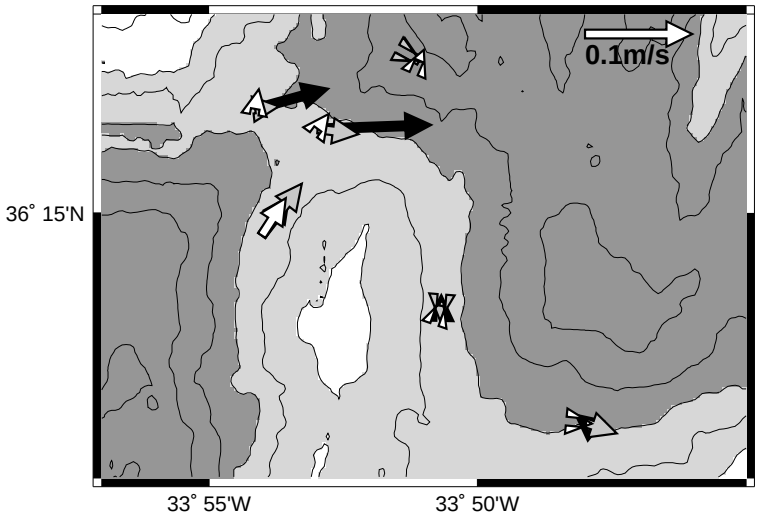

Fig. 3.8: Average current-meter velocities in the vicinity of *Rainbow Ridge* recorded during the first week of mooring deployment; shading of the arrows is determined by the instrument depths with black, gray and white indicating 2300 m, 2100 m and 1800 m, respectively; bathymetric shading is the same as in Fig. 1.2; contour interval is 250 m.

meter velocities averaged over the first week of deployment, i.e. immediately after the *FLAME* cruise. (The current-meter data are analyzed in chapter 4). On the sill the velocities at 2300 m (black arrows) are consistent in magnitude and direction with the LADCP velocities shown in Fig. 3.5 while the strong boundary current on the western slope of *Rainbow Ridge* was not sampled. Overall, the consistency between the two independent velocity measurements is striking and suggests that the flow across *Rainbow Sill* can be considered quasi-steady over periods of weeks. The current meters from mooring "F", which is not shown in the figure, indicate N- to NE-ward mean flow of 0.01–0.03 $\mathrm{m \cdot s^{-1}}$ between 1800 m and 2300 m.

Fig. 3.9 shows a flow-speed profile from the saddle of *Rainbow Sill*. The layer of strong flow peaking at $> 0.25\,\mathrm{m \cdot s^{-1}}$ has a vertical scale of approximately 300 m. Similar layers of intense currents are apparent in four out of the seven profiles from the western slope of *Rainbow Ridge*; they have vertical scales between 250 m and 400 m and peak flow speeds between $0.17\,\mathrm{m \cdot s^{-1}}$ and $0.28\,\mathrm{m \cdot s^{-1}}$. Fig. 3.10 shows the vertical structure of the 50 m-averaged velocity field on the western slope of *Rainbow Ridge* derived from all seven LADCP profiles. The layer of intense flow is confined to depths below 2000 m where the direction is much more uniform than above, indicating topographic steering.

Layers of intensified flow near the seabed were observed in profiles away from the western

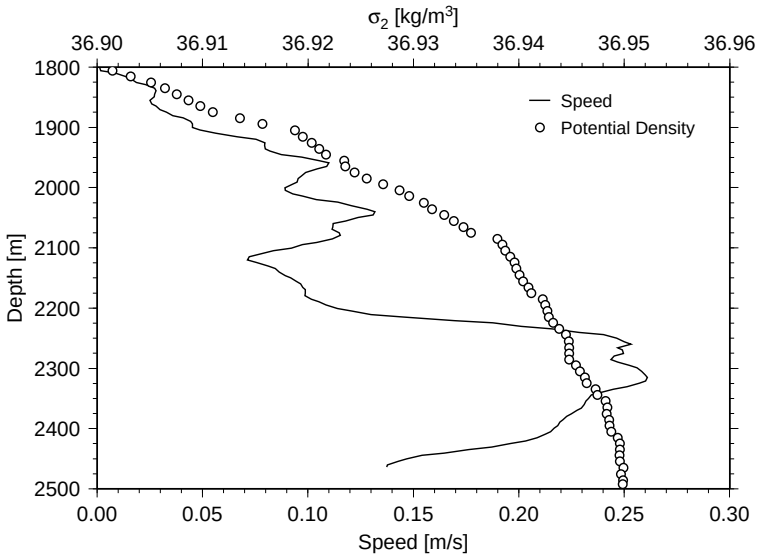

Fig. 3.9: Flow speed and density profiles from the saddle of *Rainbow Sill*.

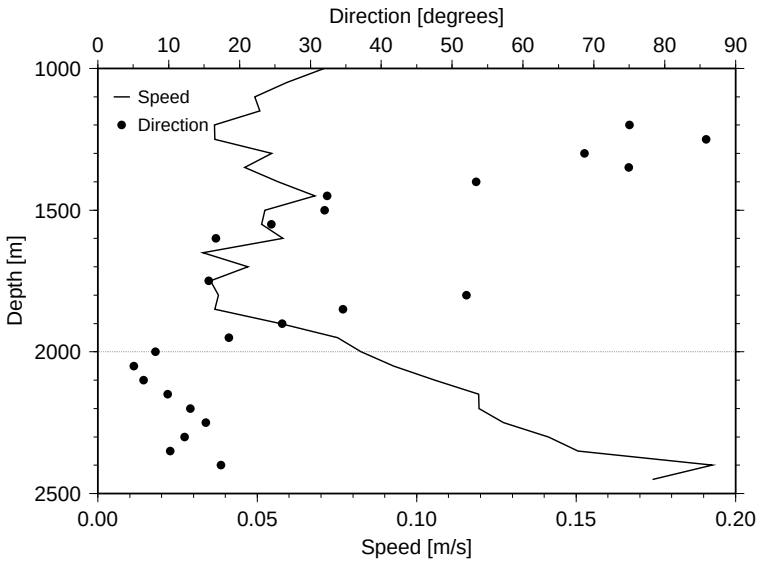

Fig. 3.10: Pressure-averaged flow field on the western slope of *Rainbow Ridge*; each data point represents a 50 m vertical mean; the dotted line is the same as in Fig. 3.6.

slope of *Rainbow Ridge* as well. They have typical vertical scales of $\approx$50 m and peak flow speeds between 0.1 m·s^{-1} and 0.15 m·s^{-1}. (It is interesting to note that a profile from the western slope of a different topographic high (near 33°45′W/36°19′N) is similar to the ones from the western slope of *Rainbow Ridge*, with a 200 m-thick layer of intensified flow peaking at 0.19 m·s^{-1}.)

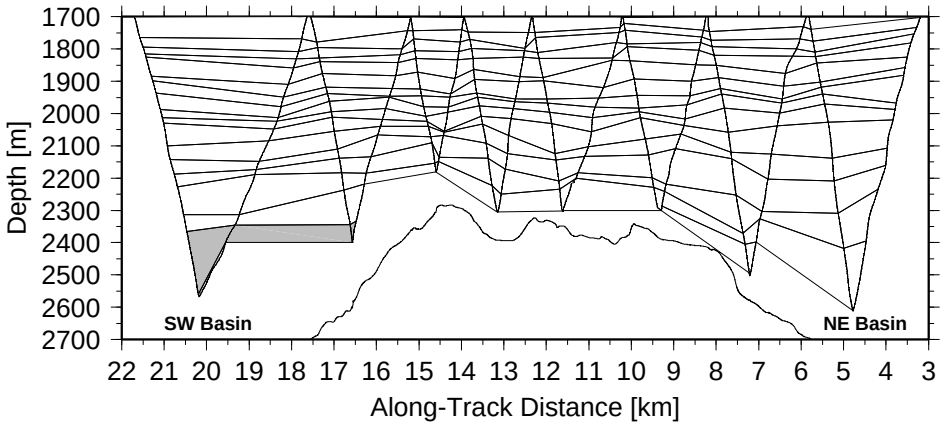

Fig. 3.11: Isopycnal contours from a tow-yo across *Rainbow Sill;* contour levels were chosen for uniform spacing with depth; the shaded area indicates $\sigma_2 > 36.945$, found in the NE basin only below 2600 m except for a few profiles close to *Rainbow Sill*.

Flow Across *Rainbow Sill*

Fig. 3.11 shows a selection of isopycnal contours from a tow-yo across *Rainbow Sill* (the black cross-sill tow of Fig. 2.1). The contour levels were chosen so that their mean depths are uniformly spaced; total density range is 36.874–36.949 (c.f. Fig. 3.6). The isopycnal surfaces of the densest water on the sill follow the topography descending into the NE basin, consistent with NE-ward cross-sill flow. Downstream of the sill saddle the isopycnal surfaces below 2000 m exhibit vertical spreading consistent with Fig. 3.6. This effect may indicate high rates of diapycnal mixing, similar to observations in cross-sill flows elsewhere (e.g. *Polzin et al.,* 1996). A second cross-sill tow-yo which was discarded because of instrument-calibration problems (section 2.1) also shows a horizontal density gradient below 2000 m caused by downsloping of the isopycnal surfaces in the NE basin.

The densest water observed on *Rainbow Sill* (Fig. 3.6) has a *(BRIDGET*-derived) σ_2 value of 36.947 which is indistinguishable within the instrument intercalibration uncertainties (section 2.1) from the (CTD-derived) potential density found within the deep basins on either side of the sill (Fig. 3.2). This observation, together with the virtually identical θ_2/S characteristics of the deep water in both basins (section 3.2.2), indicates that *Rainbow Sill* does not block the along-valley flow. The criterion (derived from laboratory and numerical experiments) for topographic blocking to occur in linearly stratified uniform flows across two-dimensional obstacles is that the dimensionless parameter (sometimes termed a Froude

number) $G = N_i h_b / U_i \gtrapprox 2$ for most obstacle shapes in non-rotating flows *(Baines,* 1987) and $G \gtrapprox 1.5$ for rotating flows over a Gaussian ridge *(Pierrehumbert and Wyman,* 1985). N_i, U_i and h_b denote the upstream buoyancy frequency, flow speed and the height of the obstacle, respectively. Using $N_i = 10^{-4}\,\mathrm{s}^{-1}$, $U_i = 0.05\,\mathrm{m \cdot s}^{-1}$ (typical LADCP-measured speed away from *Rainbow Ridge*), and $h_b = 700\,\mathrm{m}$ (height of *Rainbow Sill* above the SW basin floor), G becomes 1.4, i.e. close to the limiting value. The uplifting of deep upstream water is driven by the dynamic pressure reduction caused by the large flow velocities across the sill, a phenomenon sometimes called Bernoulli Aspiration (e.g. *Kinder and Bryden,* 1990).

The horizontal density gradient across *Rainbow Sill* is consistent with upstream influence of an obstacle which has been observed for values of G as low as 0.75 *(Pierrehumbert and Wyman,* 1985). The orientation of the corresponding pressure gradient implies a mean flow from the SW into the NE basin. The observation that the density distributions of the individual tows (e.g. Fig. 3.11) are consistent with the mean picture (Fig. 3.6) suggests that the overflow across *Rainbow Sill* can be considered quasi-steady on the survey time scale (24 days). Evidence for persistent flow on even longer time scales is provided by the current meter measurements (chapter 4), by the observation of a northward current on the western slope of *Rainbow Ridge* throughout an ROV dive lasting 26h in August 1996 *(German et al.,* 1996a), and by the along-segment hydrographic gradients, consistent with our data, observed between August and October 1992 *(Wilson et al.,* 1995).

In the case of an inviscid steady two-dimensional flow along a channel of slowly varying geometry a horizontally asymmetric density distribution (i.e. differing reservoir conditions) implies that the flow is (hydraulically) controlled *(Armi,* 1986). *Pratt* (1986) shows how the inviscid assumption of hydraulic models can be tested by evaluating the non-dimensional parameter $P = C_d l / h$ (indicating the relative importance of hydraulic acceleration and deceleration caused by bottom friction) where $C_d (= 10^{-3})$, l, and h are the drag coefficient, the horizontal distance over which the thickness of the active lower layer (see below) changes significantly, and the mean thickness of that layer, respectively. Conservatively estimating $l = 15\,\mathrm{km}$ and $h = 300\,\mathrm{m}$ from Fig. 3.11 results in an estimate of $P \approx 0.05$, indicating that frictional effects can be ignored. *Killworth* (1995) shows that the equivalence of hydraulic control and flow maximization known from non-rotating hydraulics holds for continuously stratified rotating flows controlled by sills and narrows of arbitrary topography as well. Therefore, a hydraulic model can be used to estimate the volume flux across *Rainbow Sill*. The simple

$1\frac{1}{2}$-layer reduced-gravity model (c.f. chapter 9) with zero upstream potential vorticity introduced by *Whitehead, Leetmaa, and Knox* (1974) is considered adequate for this purpose, mainly because it is the simplest model of rotating hydraulics which has been tested in the oceanographic context *(Whitehead,* 1997). (Without rotation it reduces to hydraulic flow over a weir.)

Layer models require estimates for the density differences between the individual layers which are assumed to be homogeneous. The separation of the water column into such layers is difficult except where there are sharp vertical hydrographic gradients coinciding with regions of high shear. In the *FLAME* profiles (e.g. Fig. 3.9) there are no clear indications for such layers. *Whitehead* (1989) proposes a simple and consistent method for dealing with this problem. It is based on the observation that in a hydraulically controlled stratified unidirectional flow the mean upstream/downstream density difference is generally confined below a well-defined depth (indicated by the horizontal lines in Figs. 3.6 and 3.7). This depth is termed the *bifurcation depth* and is taken to be the upstream level of the interface between the two model layers, which makes this method equivalent to defining the interface as the maximum density surface which remains horizontal over the sill (e.g. *Mercier and Bryden,* 1994). The density difference between the active lower and the passive upper layer is set to the maximal horizontal upstream-downstream density difference between the bifurcation depth and the sill depth. (This method yields correct values for homogeneous layers.) The respective values for the flow across *Rainbow Sill* are estimated from Figs. 3.6 and 3.7; they are 2000 m for the bifurcation depth and 4.5×10^{-3} for the density difference, resulting in a reduced gravity estimate of $g' \approx 4.5 \times 10^{-5}\,\mathrm{m\cdot s^{-2}}$. The vertical scale $h_u = 500\,\mathrm{m}$ of the flow between the bifurcation depth and the sill depth is consistent with the intensified current layer shown in Fig. 3.10.

In hydraulically controlled flows some suitably averaged velocity at the control is equal to a gravity wave speed so that the flow becomes critical (e.g. *Armi,* 1986). The only gravity waves possible in a $1\frac{1}{2}$-layer model are interfacial waves propagating with a speed of $(g'h)^{1/2}$. Defining the appropriate lower-layer depth h in a rotating system is not straightforward because it is not constant even across a flat-bottomed channel. However, if it is assumed that h_u is a representative depth, the wave speed becomes $0.15\,\mathrm{m\cdot s^{-1}}$ which is similar to the average flow speed of $0.17\,\mathrm{m\cdot s^{-1}}$ between 2000 m and 2500 m observed on *Rainbow Sill* (Fig. 3.9).

The model of *Whitehead, Leetmaa, and Knox* (1974) is now used to estimate the volume flux Q and the width w of the overflow current. The respective expressions for a sill which is wide compared to the internal Rossby radius of deformation are $Q = g' h_u^2/(2f)$ and $w = (2g' h_u)^{1/2}/f$. As suggested by *Whitehead* (1989), we use the sill width at the bifurcation depth for the comparison with the Rossby radius; the value of 7.5 km estimated from bathymetric charts (e.g. Fig. 4.9) is much larger than the Rossby radius $(g' h_u)^{1/2}/f \approx 1.7\,\mathrm{km}$ (where $f = 8.6 \times 10^{-5}\,\mathrm{s}^{-1}$ is the Coriolis parameter at 36°N). The volume-flux and current-width estimates become $Q \approx 65 \times 10^3\,\mathrm{m}^3\cdot\mathrm{s}^{-1}$ and $w \approx 2.5\,\mathrm{km}$, respectively. *Killworth* (1994) derived parameterizations for hydraulically controlled fluxes across sills of more realistic geometries and upstream conditions and showed the expression of *Whitehead, Leetmaa, and Knox* (1974) to be an upper bound. Using his expression for parabolic sills leads to a reduction of the flux estimate by 5% which is consistent with the observation that *Rainbow Sill* is wide compared to the Rossby radius. The Rossby number of the flow $\mathrm{Ro} = U/fl \approx 0.5$ (based on the half-width of *Rainbow Sill* between the two deep basins ($l \approx 5\,\mathrm{km}$) and a velocity scale of $0.2\,\mathrm{m}\cdot\mathrm{s}^{-1}$ estimated from Fig. 3.10) indicates that the model assumption of geostrophically adjusted flow across the sill is at least partially violated. Effects of steady or time-variable (e.g. tidal) barotropic forcing are ignored.

A Topographic Wake

The mean density profiles of the two deep basins (Fig. 3.6) suggest that the hydraulically controlled flow is confined to depths below 2000 m. Between this level and the peak of *Rainbow Ridge* at 1950 m the incident current, of order $0.05\,\mathrm{m}\cdot\mathrm{s}^{-1}$ (Fig. 3.10), flows over and around the topography. Evaluating G (see above) with $N_i = 10^{-3}\,\mathrm{s}^{-1}$ (Fig. 3.7) and $h_b = 50\,\mathrm{m}$ results in a value of 1.0, indicating that no blocking is expected. The characteristic half-width l of the top 50 m of *Rainbow Ridge* is 1–2 km. Because $l \gg U_i/N_i = 50\,\mathrm{m}$ non-hydrostatic effects may be ignored, while the corresponding Rossby number of ≈ 0.5 indicates that rotational effects are important.

The appropriate flow regime for these parameters is the *rotating wave regime* of *Queney* (1948) (see *Gill,* 1982). In this regime, lee waves radiate energy (group velocity) upwards and down-stream at an angle between 1° and 90° to the horizontal. The horizontal wavelength λ of the pattern of vertical stream-line displacement close to a bell-shaped ridge is $2\pi U_i/f$, which becomes $\approx 4\,\mathrm{km}$ using the *Rainbow* parameters. Because this is comparable to the width

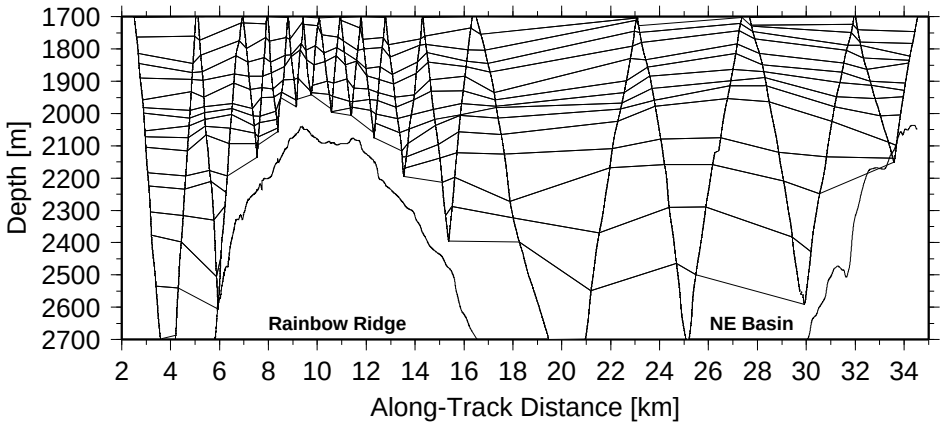

Fig. 3.12: Isopycnal contours of a tow-yo across *Rainbow Ridge*; contour levels are the same as in Fig. 3.11.

($2\,l$) of *Rainbow Ridge* large-amplitude lee waves are expected. Fig. 3.12 shows a selection of isopycnal contours from a tow across *Rainbow Ridge* (the black cross-ridge tow of Fig. 2.1). The pattern of isopycnal-surface displacement found in the lee of the ridge is consistent with the rotating wave regime because it appears to be confined in the quadrant upwards and downstream of the ridge peak and because the wavelength directly over the peak is $\approx 5\,\mathrm{km}$. (The doming of the isopycnals in the eastern part of the NE basin is not considered to be a topographic-wave pattern; it is consistent with tidal effects, however; see below.) Two additional *BRIDGET* tows across *Rainbow Ridge* show similar wave-like features although the patterns there are less clear because of decreased horizontal resolutions caused by larger towing velocities. These observations together with the horizontal extent of the lee-wave patterns ($\approx 10\,\mathrm{km}$) indicate that the topographic wake is most likely caused by the mean flow (a velocity of order $0.5\,\mathrm{m\cdot s^{-1}}$ would be required to propagate a disturbance over that distance in half a tidal period).

Hydrographic Variability on Tidal Time Scales

One of the main problems in interpreting hydrographic surveys like the one presented here is the difficulty in separating spatial and temporal scales, especially in the tidal range. (Based on re-sampling of the same region over the 24 days of data collection, a measurable shift of the hydrography over this time scale can be excluded.) The vertical displacement of the isopycnals shown in Fig. 3.12, for example, is caused by a combination of spatial and temporal

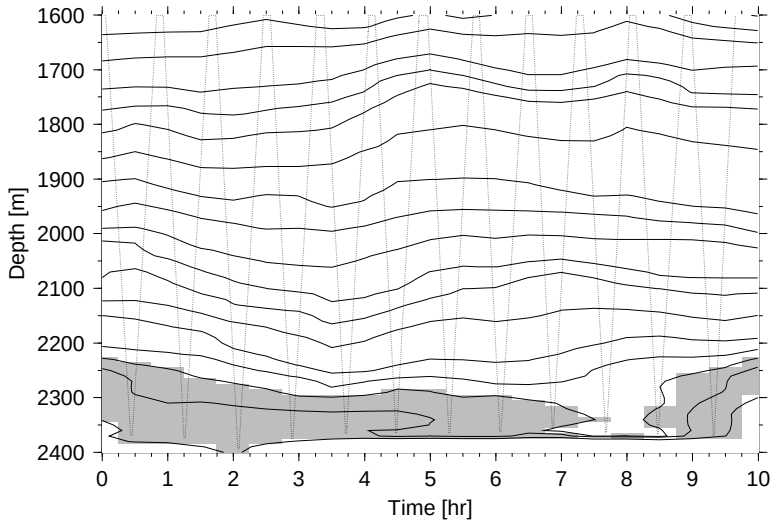

Fig. 3.13: Isopycnal contours of the 10 h CTD yoyo; contour levels and shading are the same as in Fig. 3.11; total density range is 36.845–36.948.

variability over the sampling time of 12 h. If the doming of the isopycnals in the NE basin were a spatial feature it would imply anticyclonic flow around the basin, which is inconsistent both with direct velocity measurements (e.g. Fig. 3.5) and with density observations from four additional tows crossing the same basin in different directions.

To investigate the temporal variability of the hydrography on tidal time scales a 10 h CTD yoyo (12 individual down-/up-casts) between 1600 m and the sea bed at 2400 m was done at a station close to *Rainbow Sill* (the black star with a white border of Fig. 2.1). Unfortunately, the LADCP failed during the cast. Fig. 3.13 shows the evolution of the isopycnal surfaces during sampling. Between the upper turning point at 1600 m and $\approx$2250 m the isopycnals show a wave-like structure consistent with the semi-diurnal tidal period. The phase of isopycnal displacement appears to vary with depth. The maximum amplitude near 1800 m is $>$100 m (similar to the observations of *Rudnicki et al.* (1994) at the TAG hydrothermal site) but values of order 50 m are more typical. Close to the sea floor the structure is more complex; the potential density inversions at 4.5 h, 7 h, and 8.5 h are not contouring artifacts. (There are indications from the CTD altimeter for some horizontal displacement during the cast.)

3.3 1998 Survey *(FLAME-2)*

3.3.1 Changes in the Rift-Valley Hydrography and Flow Regime Between 1997 and 1998

A plot of the pressure-averaged θ_2/S properties of the rift-valley stations occupied in 1998, the corresponding eastern background station, and the western background station occupied in 1997 (no western background station was occupied during *FLAME-2)* results in a figure which is visually indistinguishable from Fig. 3.3 except for slight changes in the Mediterranean signature of the eastern background station. The near-surface temperature was higher in 1998 (23°C vs. 19°C) while the corresponding salinity had decreased (from 36.3 psu to 36.2 psu). Because the depth of the 15°C isotherm had decreased as well (from 280 m to 205 m), the Azores Front is inferred to have been situated south of *AMAR* during the 1998 survey (c.f. section 3.2.1). This is supported by the observation (from the uncalibrated hull-mounted ADCP) that the strong currents in the top 300 m of the water column observed in 1997 had disappeared in 1998.

Fig. 3.14 shows the pressure-averaged rift-valley θ_2/S characteristics of the *Rainbow* region in 1997 and 1998 (10 stations) as well as those of the eastern background station occupied in both years. There is a slight difference between the eastern background properties of the two surveys at densities >36.9 (i.e. below ≈ 1750 m). Interestingly, the rift-valley hydrography of the 1998 data set appears more consistent with the eastern background properties of the 1997 survey. Below 4°C the hydrographic properties of the 1997 and 1998 rift-valley data are identical (within the measurement uncertainties). Above 4°C the θ_2/S properties of the 1997 data set diverge from the linear trend because of the interleaving signatures observed in the SW basin (section 3.2.2) whereas no similar effect is seen in the corresponding properties of the 1998 data set. Inspection of the individual profiles confirms that no interleaving structures were observed in 1998. The similarity of the corresponding θ_2/S properties below 4°C indicates that it is unlikely that the origin of the rift-valley water had changed between the surveys.

To assess possible changes in the rift-valley hydrography the density, temperature and salinity ranges of the two surveys were compared; Fig. 3.15 shows the temperature profiles. Depths >2500 m are not shown because the 1998 data set contains only 3 profiles from the *Rainbow* region extending below this limit. The temperature ranges are indistinguishable

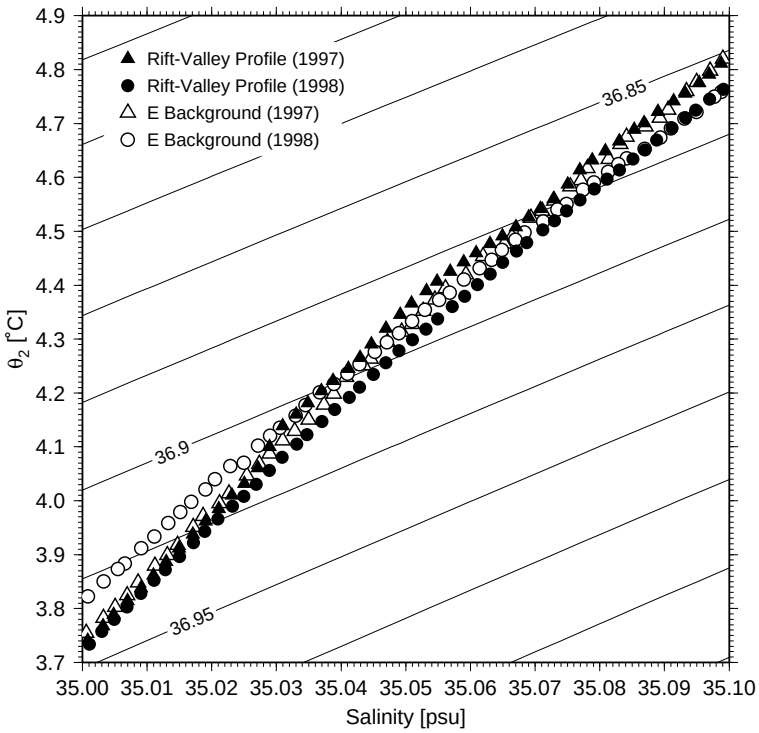

Fig. 3.14: θ_2/S comparison of the *FLAME* and *FLAME-2* data below $\approx$1600 m; the rift-valley profiles are derived from pressure-averaged CTD stations in the 1997 sampling region; the eastern background profiles of the two surveys are shown as well; σ_2 contour interval is 0.025.

within the variability encountered during each survey. The same observation holds for the salinity and for the density data.

While these comparisons indicate that changes in the rift-valley hydrography above 2500 m between 1997 and 1998 were small compared to the short-time-scale variability, Fig. 3.2 reveals that comparing the hydrographic properties at greater depths can reveal more precise answers. In the SW basin there is one CTD profile extending below 3200 m from each survey (the horizontal distance between the stations is 1.4 km); the corresponding deep θ_2/S properties are shown in Fig. 3.16. Extrapolating the temperature profiles to the seafloor at 3300 m yields minimum temperatures of 3.655°C *(FLAME)* and 3.597°C *(FLAME-2)*. This implies a cooling of the bottom water of order 0.06°C, a value significantly greater than the temperature calibration uncertainties (sections 2.1 and 2.2). The near-perfect agreement between the salinities is fortuitous (observed salinity differences between neighboring profiles of the 1998 data set are of order 3×10^{-3} psu, consistent with the salinity sensor accuracy).

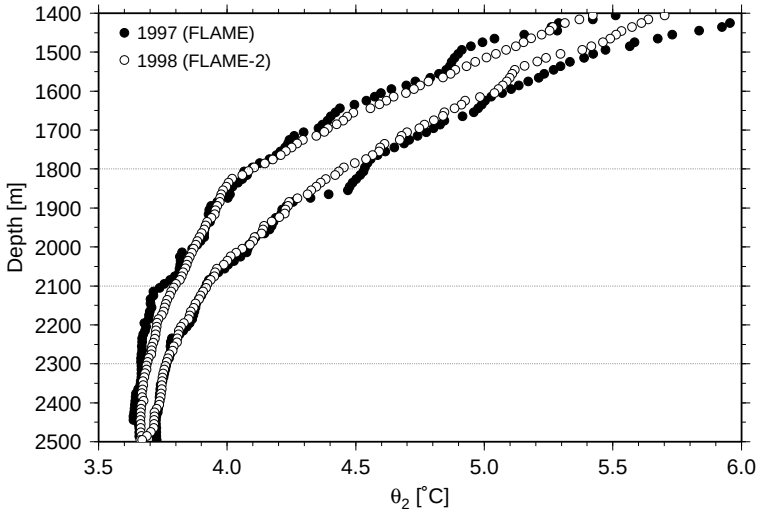

Fig. 3.15: Comparison of the potential temperature ranges (minimum and maximum values are plotted) observed during the 1997 and 1998 surveys; the horizontal lines indicate the nominal depths of the moored current meters (section 2.3).

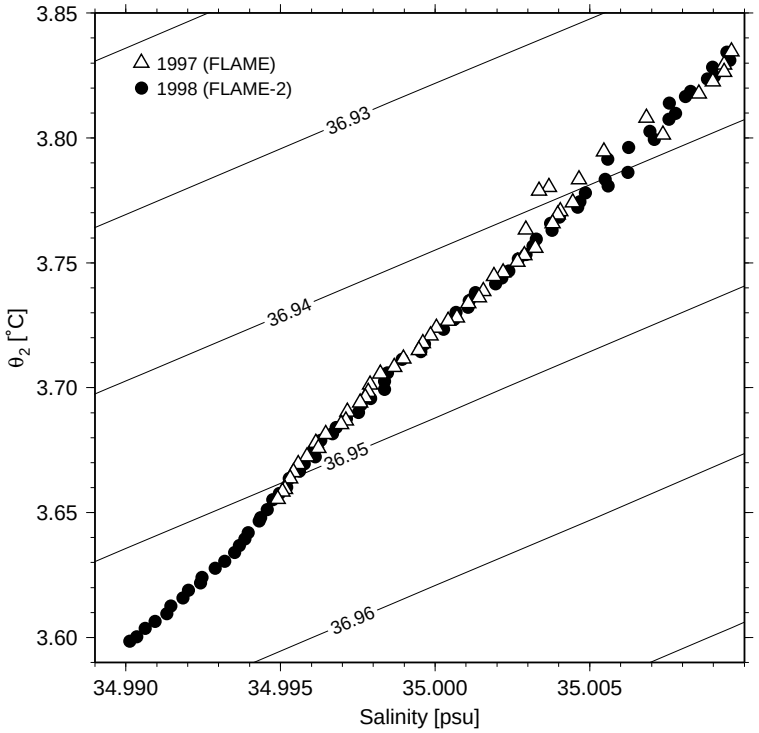

Fig. 3.16: θ_2/S comparison of a 1997 and a 1998 profile taken in the deep SW basin; both profiles are truncated at 3200 m; σ_2 contour interval is 0.01.

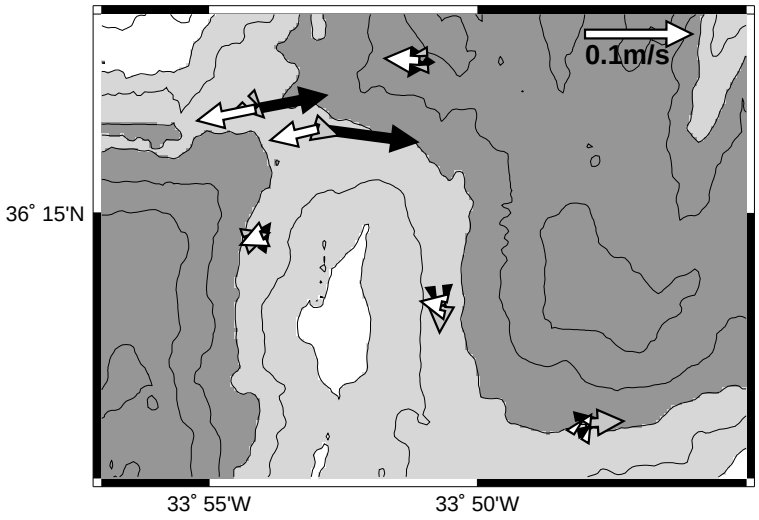

Fig. 3.17: Average current-meter velocities in the vicinity of *Rainbow Ridge* from the last full week of mooring deployment; shading of the arrows is determined by the instrument depths with black, gray and white indicating 2300 m, 2100 m and 1800 m, respectively; bathymetric shading is the same as in Fig. 1.2; contour interval is 250 m.

Fig. 3.17 shows the average velocities recorded during the last full week of current-meter deployment. Comparison with Fig. 3.8 indicates that the cross-sill flow below 2100 m was similar in 1997 and 1998 while it had reversed direction and increased in strength at 1800 m. The current meters from mooring "F", which is not shown in the figure, indicate NE-ward mean flow of 0.02–0.03 $\mathrm{m \cdot s^{-1}}$ below 2100 m (c.f. Fig. 8.2) and SW-ward flow of 0.02 $\mathrm{m \cdot s^{-1}}$ at 1800 m. Strong weekly-averaged SW-ward currents across *Rainbow Sill* at 1800 m had been recorded during the 2 preceding weeks as well, peaking during the penultimate week of mooring deployment (c.f. Fig. 4.6). The lack of interleaving signatures in the 1998 data is consistent with the reversed flow at 1800 m and provides further support for the hypothesis that the origin of the interleaving water in 1997 was west of *Rainbow Ridge* (section 3.2.2).

In the 1998 data set the mean density profiles from the NE and the SW basin do not show any patterns which can be related to the flow field. This is most likely because of the small number of stations occupied in the vicinity of *Rainbow Sill* (Fig. 2.2) which does not allow the calculation of representative mean hydrographic profiles.

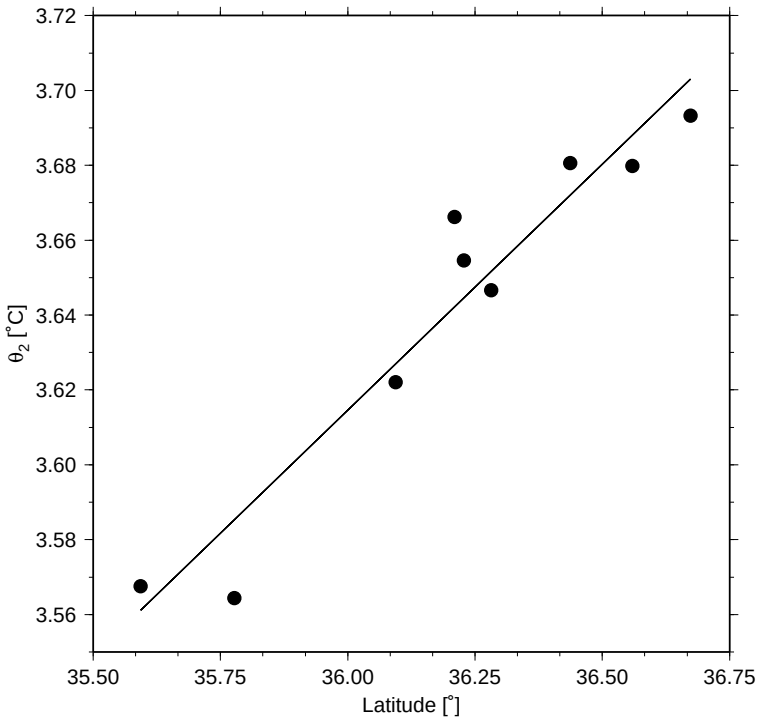

Fig. 3.18: Scatter plot and linear fit of the 1998 temperature measurements at 2550 m; the regression coefficient ($\pm 1\sigma$) and RMS error are $1.0(\pm 0.1) \times 10^{-3}$°C·km^{-1} and 1.3×10^{-2} °C, respectively; the correlation coefficient is $r = 0.96$.

3.3.2 Along-Segment Hydrographic Gradients

During the 1998 survey CTD stations were occupied along the entire length of the *AMAR* segments between 35°30′N and 36°40′N (Fig. 2.2). To assess along-segment gradients in the deep water all profiles extending below 2550 m were selected (north of *Rainbow Sill* there is only one profile extending below 2600 m). These deep stations are marked with black-and-white stars in Fig. 2.2. One profile with anomalous hydrographic properties below 2175 m (section 3.3.3) was removed from the data set. The θ_2/S properties of the remaining stations are indistinguishable within the measurement uncertainties below 2000 m, i.e. there are no indications for geothermal heating (the temperature differences are compensated by corresponding salinity differences). Fig. 3.18 shows a scatter plot and linear fit of the along-segment temperature observations at 2550 m. The regression coefficient ($\pm 1\sigma$) and RMS error are $1.0(\pm 0.1) \times 10^{-3}$°C·km^{-1} and 1.3×10^{-2} °C, respectively. (The data are plotted against latitude for easy location but the gradient is calculated in terms of distance to aid in comparison with other sites; total segment length is 150 km; section 1.3.3. For compari-

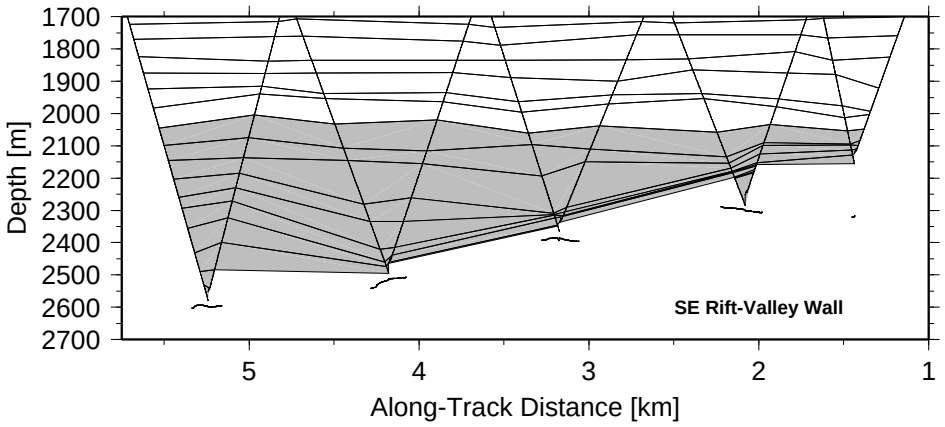

Fig. 3.19: Density section from the CTD tow-yo on the rift-valley side of the sill near 35°35′N/34°15′W (Fig. 2.2); the bathymetry is taken from the CTD altimeter; the shaded area ($\sigma_2 \geq 36.9449$) shows isopycnal downsloping and spreading consistent with inflow from the southeast; contour levels were selected for uniform spacing with depth in the final upcast.

son, the temperature gradient of segment "C" surveyed by *Saunders and Francis* (1985) is $\approx 0.8 \times 10^{-3}$°C·km^{-1}, estimated from the 0.1°C warming over 120 km horizontal distance.) The magnitude of the RMS error is consistent with the high-frequency variability at 2300 m recorded by the moored temperature sensors around *Rainbow Ridge* (section 4.4).

Applying the same analysis to the salinity measurements results in a gradient estimate and RMS error of $7.8(\pm 2.6) \times 10^{-5}$ psu·km^{-1} and 1.5×10^{-3} psu, respectively. The RMS error is consistent with the salinity fluctuations associated with the high-frequency variability, estimated from the temperature fluctuations and the θ_2/S properties. Finally, the along-segment density gradient and RMS error are $-1.0(\pm 0.1) \times 10^{-4}$ kg·m^{-3}·km^{-1} and 1.8×10^{-3} kg·m^{-3}, respectively.

3.3.3 Inflow Into *South AMAR*

As discussed in sections 3.2.2 and 3.3.1, the rift-valley θ_2/S properties of both surveys suggest inflow from the eastern ridge flank. The most likely location of the inflow is near the southern end of the *AMAR* segments where the densest water is found (section 3.3.2). This is consistent with the observed unidirectional NE-ward flow across *Rainbow Sill* (section 3.2.3 and chapter 4). The available bathymetry (Figs. 1.2 and 1.3, *Detrick et al.* (1995), and an unpublished *IFREMER* high-resolution bathymetric data set) indicate that the most likely inflow sill is located near 35°35′N/34°15′W. Fig. 3.19 shows a density section from the rift-

valley side of that sill; total sampling time of the CTD tow-yo was approximately 4 h. The down-sloping and spreading of the isopycnal surfaces in the shaded area is consistent with inflow from the southeast. The densest water observed in this section has a σ_2 value of 36.970 which corresponds to a depth of 2200 m in the eastern off-ridge profile, located approximately 50 km NE of the sill.

To estimate the volume flux into the *AMAR* segments the hydraulic model of *Whitehead, Leetmaa, and Knox* (1974) is used (c.f. section 3.2.3). Evaluating the non-dimensional parameter of *Pratt* (1986) yields a value of $P \approx 0.02$ (using $l = 5$ km and $h = 300$ m, estimated from Fig. 3.19), indicating that frictional effects may be ignored at this sill as well. In addition to the tow-yo section there was only one CTD station occupied near the sill (Fig. 2.2). Therefore, there is some uncertainty as to the bifurcation depth and the upstream/downstream density difference; the best estimates for the upstream interface height and reduced gravity are $h_u = 250$–300 m and $g' = 1.8 \times 10^{-4}\,\mathrm{m\cdot s^{-2}}$, respectively. At the bifurcation depth the sill is wide (12 km) compared to the Rossby radius of deformation ($\approx$2.5 km) and the volume flux estimate becomes 65–$95 \times 10^3\,\mathrm{m^3\cdot s^{-1}}$. Because of the good agreement between a similar calculation and direct flow observations at *Rainbow Sill* (section 3.2.3), the inflow velocity is estimated from the interfacial gravity wave speed of the $1\frac{1}{2}$-layer hydraulic model resulting in a value of $U \approx 0.2\,\mathrm{m\cdot s^{-1}}$.

Not all of the rift-valley water must necessarily flow in across a single sill. The θ_2/S properties below 2175 m recorded at a station near 35°40′N/34°20′W (Fig. 2.2) are characterized by a positive salinity offset of order 3×10^{-3} psu with respect to the remaining profiles of the 1998 survey. (Because the salinity offset is apparent in both the down- and the up-cast instrument problems can be excluded.) Whether the deep water at this station has a different origin or whether it is a remnant of an earlier inflow event across the same sill cannot be determined from our data. There are no similar signatures in any of the other profiles from either survey. We also occupied stations near two sills at the northern end of the *AMAR* segments (Fig. 2.2). The respective θ_2/S properties show no indications for different water masses which could indicate additional inflow across these sills (see also chapter 8).

3.4 Discussion

The two hydrographic surveys carried out in 1997 and 1998 are fully consistent with the observations of *Saunders and Francis* (1985). Within the rift valley of the *AMAR* segments the density and stratification are reduced in comparison to the water column on the ridge flanks. The θ_2/S properties of the rift-valley water suggest inflow from the east where the water is denser than at the same depth on the western ridge flank. In 1998 we observed along-segment hydrographic gradients consistent with inflow near the southern end of the segments. A density section from the most likely candidate sill connecting *South AMAR* to the eastern ridge flank indicate inflow of the right magnitude to account for the flow observations at *Rainbow Sill* (see also section 4.5).

While the 1997 survey did not allow along-segment gradients to be calculated, the mutual consistency of the rift-valley θ_2/S properties during the two surveys indicates that the situation was most likely similar in both years. Whereas the θ_2/S properties did not change, there are indications for a cooling of approximately 0.06°C at 3200 m. Such a change is consistent with time-varying inflow, e.g. caused by eddies or variable boundary currents *(Saunders and Francis,* 1985). Nevertheless, the weekly averaged current-meter records from the beginning and from the end of the mooring deployment show similar flow across *Rainbow Sill* below 2100 m indicating that the relationship between forcing and response should be investigated (c.f. chapter 9). Above 2500 m the high-frequency hydrographic variability is too high to determine any change between the two surveys.

The availability of high-quality hydrographic data along the entire *AMAR* segments allows the conceptual model of *Saunders and Francis* (1985) (section 1.3.1) to be extended. The rift-valley θ_2/S properties indicate that the observed along-segment temperature gradient is not (primarily) caused by geothermal heating (c.f. chapter 8). There are two different processes which can account for the observations:

Topographic Blocking. It is unlikely that topographic blocking plays a significant role because the gradient calculations are based on measurements at 2550 m which is shallower than the rift valley everywhere except for a 7 km stretch near 35°55′N (Fig. 1.2).

Diapycnal Mixing. The rough bathymetry of the MAR is known to be associated with high rates of diapycnal mixing (e.g. *Polzin et al.*, 1997; *Ledwell et al.*, 2000). It has been hypothesized that much of the energy available for diapycnal mixing on a

global scale is dissipated by breaking internal waves (e.g. *Polzin et al.,* 1995). The isopycnal variability on tidal time scales and the topographic wake observed in 1997 are therefore consistent with high rates of diapycnal mixing. Our observations furthermore suggest that hydraulically controlled sill flows may be common in the rift valley of the MAR. Direct measurements elsewhere have shown greatly enhanced dissipation in such overflows (e.g. *Wesson and Gregg,* 1994; *Polzin et al.,* 1996), providing an additional mechanism for enhanced diapycnal mixing on the MAR.

The mutual consistency between the hydrographic data from the two surveys indicates that the rift-valley flow had most likely not changed significantly between 1997 and 1998. This is supported by the average current-meter velocities recorded during the first and the last weeks of mooring deployment which show similar NE-ward flow below 2000 m across *Rainbow Sill*. Hydrographic data collected in the *AMAR* segments in 1992 *(Wilson et al.,* 1995) are consistent with the along-segment gradients of the *FLAME-2* data set. Additional evidence for persistent NE-ward flow near *Rainbow Ridge* is available for 1994 *(German et al.,* 1996c) and 1996 *(German et al.,* 1996a), suggesting that the along-segment flow and hydrographic gradients may not have changed significantly for years.

Unidirectional along-valley hydrographic gradients have been observed elsewhere, e.g. by *Saunders and Francis* (1985) in the MAR rift valley near 45°N and by *Ledwell et al.* (2000) in a canyon on the western flank of the MAR near 20°S, raising the possibility that insights gained from a study of the *AMAR* segments may be valid at other sites as well.

Chapter 4

Current-Meter Observations

4.1 Introduction

In this chapter the data from 21 moored current meters (section 2.3) are analyzed and interpreted. The main goal is to quantify the temporal variability of the transport across *Rainbow Sill* which is required to assess the uncertainties associated with along-valley flux estimates of hydrothermal tracers (e.g. chapter 7). Additionally, the analysis yields estimates for the temperature variance which can be compared to the hydrographic surveys (chapter 3), and allows the particle plume dispersal to be interpreted in the context of the background flow field (chapter 5).

In section 4.2 it is shown that the low-frequency (weeks to months) temperature fluctuations are dominated by a transient warming event lasting approximately 4 months with a strong signature in the *Rainbow Sill* overflow velocities. Simple spectral techniques are applied to investigate the contributions from different frequency bands to the overall flow energy (section 4.3). The current meter records show large temporal and spatial heterogeneity which make detailed interpretation difficult. Common properties include dominance of the clockwise-polarized rotary component decreasing with increasing depth, as well as the low frequencies and the semi-diurnal tidal band dominating the flow energy. (Where strong flow had been observed during the 1997 LADCP survey (section 3.2.3) the low-frequency component dominated throughout the year.) The transient warming event had a complex effect on the patterns of energy partition at all depths within the rift valley.

The temperature variability on time scales less than one week is analyzed in section 4.4. The results indicate that the RMS amplitudes remained approximately uniform throughout

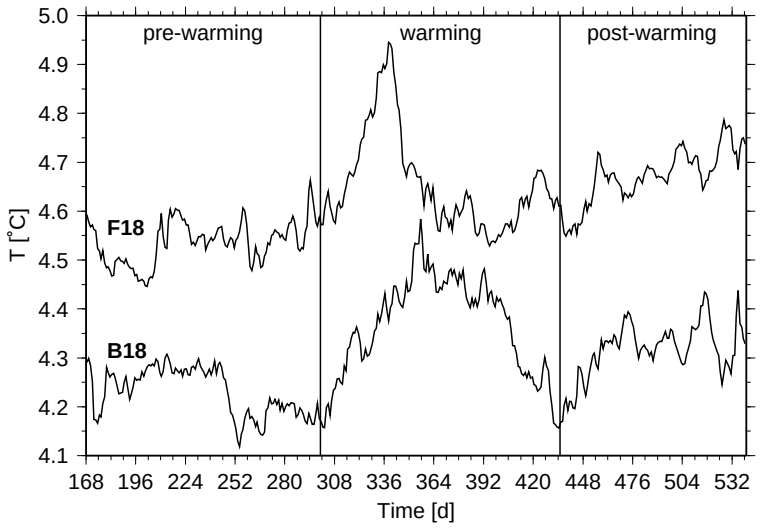

Fig. 4.1: Daily-averaged in-situ temperatures at 1800 m recorded at moorings B and F (the latter vertically offset by 0.2°C); time is given in days since the beginning of 1997; the vertical lines indicate separation into three temporal regimes (pre-warming, warming, post-warming); see Table 2.1 for instrument-naming convention.

the year with the variance decreasing with depth. In the vicinity of *Rainbow Ridge* the variability is higher than elsewhere and consistent in magnitude with the observations of the hydrographic surveys (chapter 3). The strong return flow at 1800 m across *Rainbow Sill* observed at the end of the mooring deployment coincides with a factor 2 decrease in the semi-diurnal temperature excursions of the affected instruments.

In section 4.5 the along-segment flow and the transport across *Rainbow Sill* are investigated. Somewhat surprisingly, the volume flux remained approximately constant during the entire year, in spite of the warming event. The chapter concludes with a discussion in section 4.6.

4.2 Warming Event

For a visual assessment of the instrument performance and to investigate non-periodic low-frequency signals poorly resolved by spectral methods (sections 4.3 and 4.4), daily averages were calculated from all current meter records. Fig. 4.1 shows the temperatures recorded at 1800 m on moorings B and F (see Fig. 2.3 for mooring positions). The temperature records from all instruments at 1800 m show a transient warming of 0.4°C, beginning near day 300.

(Current-meter time is referenced to the beginning of 1997.) With the exception of mooring F the temperature evolution is similar at all locations, lasting approximately until day 435. The salinity recorded by instrument B18 (the only working conductivity sensor at 1800 m, see Table 2.1 for instrument-naming convention and installed sensors) shows no indication for water of different hydrographic properties (the 0.4°C warming is accompanied by a salinity increase of 0.04 psu, consistent with the slope of the rift-valley θ_2/S properties, e.g. Fig. 3.14; salinity scatter is approximately 7×10^{-3} psu in the daily-averaged records). The temperature maxima indicate that the warming was recorded at mooring F 15 days before arriving at mooring E and 18–19 days before reaching the remainder of the instruments. The apparent propagation speed between moorings F and G (30 km apart) is $1.6\,\mathrm{km \cdot d^{-1}}$. There are no visually detectable velocity signals at 1800 m associated with the warming, neither in progressive vector diagrams (PVDs) nor in the weekly-averaged velocities but there is evidence for a relative increase of the anticlockwise-polarized energy component at 1800 m and at 2100 m during passage of the event (section 4.3.2). The consistency of the hydrographic properties recorded by instrument B18 during passage of the event with the mean properties observed during the hydrographic surveys indicates that the temperature increase is most likely a signature of isopycnal surface depression and that the hydrographic profiles from the two surveys can be used to estimate the amount of displacement, yielding a value of 150 ± 15 m. Combined with the apparent propagation speed and the relative increase of the anticlockwise (ACW) energy component, this suggests a cyclonic eddy moving across the *Rainbow* region but other interpretations may be possible.

The warming was recorded by the instruments below 2000 m as well. Fig. 4.2 shows the corresponding velocities and temperatures recorded on *Rainbow Sill* (mooring B). Warming of order 0.1°C at 2300 m (consistent with a 200 m downward displacement of the isopycnal surfaces) occurred at all moorings. At this depth the temperatures do not drop back to pre-event levels, i.e. the warming is persistent. At 2100 m the recorded data exhibit an intermediate behavior with warming of order 0.2°C followed by cooling of oder 0.1°C. The average temperatures of the first and the last weeks of mooring deployment indicate net increases ($\pm 1\sigma$) of $0.14(\pm 0.05)$°C at 2100 m and $0.04(\pm 0.01)$° C at 2300 m. It will be noted that no such warming had been observed when comparing data from the two hydrographic surveys (section 3.3.1). Close inspection of the temperature ranges shown in Fig. 3.15 indicate lower minimum temperatures at 2100 m and 2300 m in 1997 compared to 1998 whereas the

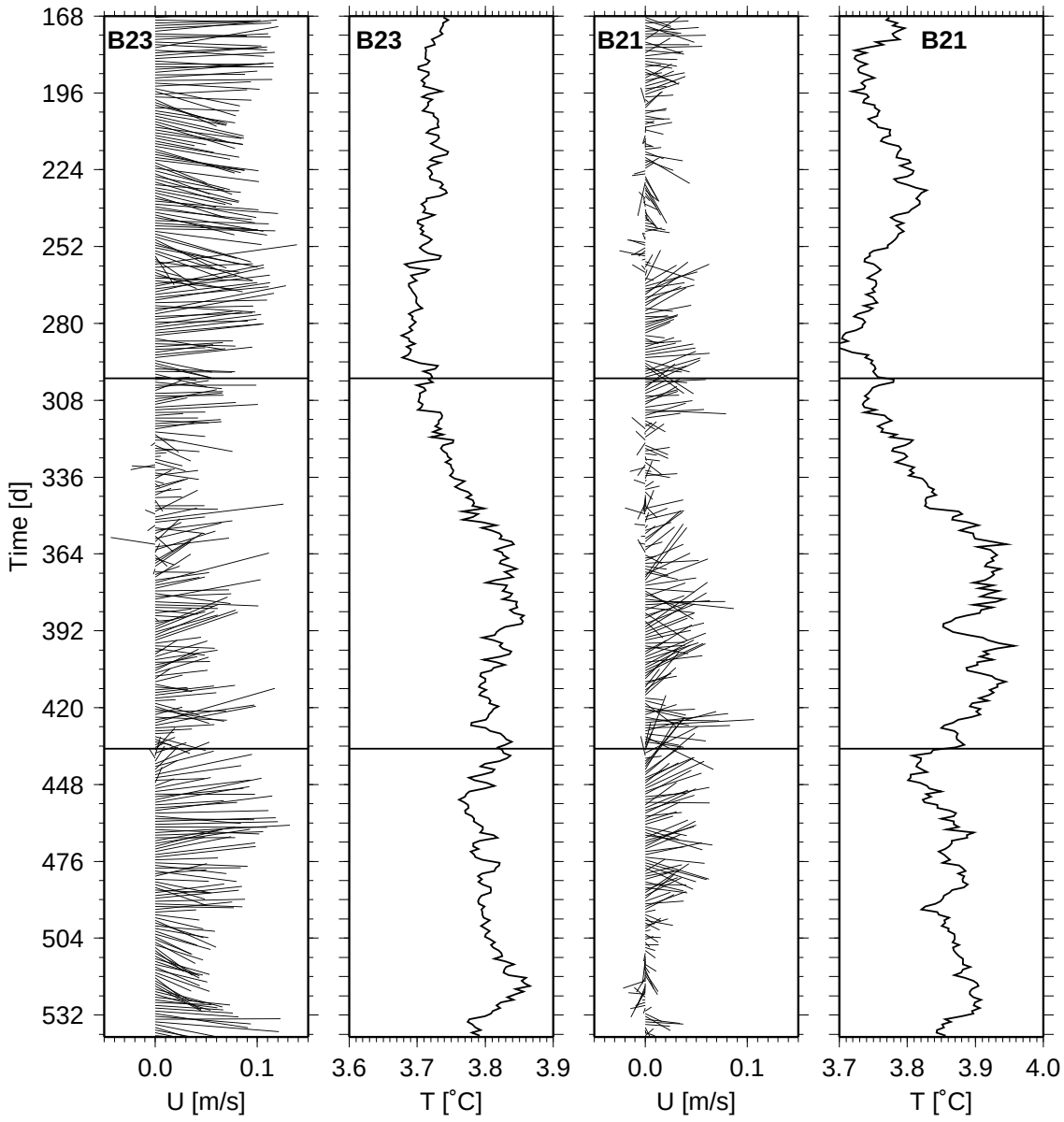

Fig. 4.2: Daily-averaged overflow velocities and temperatures recorded on mooring B (2100 m and 2300 m); flow speed is measured along the sticks; the horizontal lines indicate separation into the pre-warming, warming and post-warming regimes; time is given in days since the beginning of 1997.

maximum temperatures remained similar.

Fig. 4.2 also suggests that the pre-warming NE-ward flow across *Rainbow Sill* was persistent and strong whereas the variability increased during passage of the event with a few days when the mean flow was reversed. (The highest pre-warming variability is observed during the week following day 252 which coincides with the minimum temperature recorded by in-

strument B18, see Fig. 4.1.) The post-warming overflow variability displays an intermediate behavior. At 2100 m the overflow was less persistent than at 2300 m with the longest period of near-zero mean flow coinciding with the rising temperature flank of the warming event. The temperatures and flow velocities recorded on the second overflow mooring (D) are similar to the ones shown.

4.3 Energy Partition

4.3.1 Flow and Temperature Spectra

The daily-averaged overflow velocities shown in Fig. 4.2 are consistent with the conclusion of chapter 3 that during the 1997 survey (i.e. on a time scale of weeks) the deep flow across *Rainbow Sill* was quasi-steady. Outside the core of the overflow and on longer time scales a similar conclusion cannot be drawn, however. While averages can be calculated from any time series, mean velocities are only representative if the energetic time scales of the flow are sampled adequately; this can be assessed by comparing the integral time scales to the total length of the records *(Flierl and McWilliams,* 1978). To construct the lagged autocorrelations from which the integral time scales are derived high frequency deterministic oscillations are removed by filtering the data (e.g. *Saunders,* 1987). To determine the filtering frequency ranges discrete power spectra (periodograms) normalized to the mean squared amplitudes are calculated. Rotary spectral methods *(Mooers,* 1973; *Gonella,* 1972) are used for the velocity data because PVD observations (e.g. Figs. 5.2 and 5.8) and current meter animations indicate preferentially clockwise (CW) polarizations.

In the scope of this study no statistical analysis of the individual spectral peaks is required, implying that simple methods can be used. Because the flow energy at all frequencies is of interest the current spectra are calculated from the original data without applying any pre-conditioning (e.g. removing the mean, de-trending, pre-whitening, etc.) while the mean is removed from the temperature records before calculating the corresponding spectra. Tapering the data to decrease end effects and *leakage* as recommended by *Bendat and Piersol* (1971) was observed not to significantly change the spectra of our data sets; without tapering the summed periodograms are exactly equal to the mean squared amplitudes of the original data, providing a convenient consistency check.

Because the data sequences are not de-trended before applying the Fourier transforms

the resulting power spectra are contaminated by wrap-around discontinuities caused by the underlying periodicity assumption. Removal of (linear or higher-order) trends can decrease this problem in many cases but the effectiveness of de-trending depends on the properties of the original data and on the parametric choice of the trends to be removed. Because pre-conditioning methods such as de-trending and pre-whitening are high-pass filters they distort the low frequencies of the resulting spectra. Trends in the data (which are removed by pre-conditioning) can be caused by low-frequency oscillations which are insufficiently resolved, implying that integral time scales calculated from de-trended data can underestimate the true values and result in optimistic error estimates for the mean flow. In the case of rotary spectra there is an additional problem concerning the potential effects of pre-conditioning on the polarization properties of the modified spectra. (See *Hamming* (1989) for a discussion of additional problems which may arise when the data are pre-conditioned by removing means and trends.) In summary, the problem of how to pre-condition the data sequences before calculating power spectra is a complex one and there are opposing considerations to be taken into account. While it is acknowledged that the simple methods used here are sub-optimal for the analysis of individual spectral peaks the decision to use minimal pre-conditioning is based on the desire to preserve the energy distribution and polarization properties (section 4.3.2), and the integral time scales (section 4.5) derived from the spectra.

A simple radix-2 FFT algorithm is used to estimate the power spectra. The data sequences are shortened to the nearest power of two rather than padded with zeroes *(Hamming,* 1989). The reduction in spectral frequency resolution resulting from this truncation is not a major concern because the energy distribution is primarily analyzed in 5 frequency bands which are much wider than the resolution bandwidth of the individual spectra.

Fig. 4.3 shows the rotary flow spectra of the data recorded by instrument B23 during passage of the warming event (c.f. Fig. 4.2) as an example. The energy is characterized by a general decrease with increasing frequency with a number of superimposed significant peaks, the strongest of which are labeled. In addition to the tidal peaks at the K_1 and M_2 frequencies, there is increased energy in a number of additional bands within the internal-wave continuum between f and N, indicated below the spectra. (N is taken from Fig. 3.7, i.e. it is the mean buoyancy frequency of the SW basin during the 1997 hydrographic survey which may not accurately represent the upper frequency limit of the internal wave band at mooring B during passage of the warming event.) The peak at the sum of the inertial and the

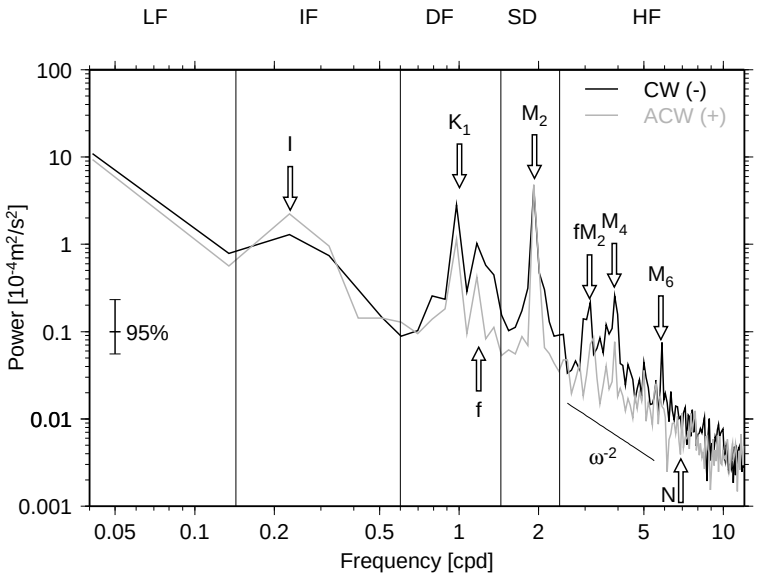

Fig. 4.3: Power spectra of the polarized energy components recorded by instrument B23 during passage of the warming event; frequency and power are in units of cycles per day and squared flow speeds, respectively; the vertical lines separate the frequency into 5 bands, labeled above the plots (c.f. Table 4.1); the arrows above the spectra indicate the main peaks at tidal frequencies (K_1, M_2, M_4, M_6), at a tidal-inertial interaction frequency (fM_2, see *Mihaly et al.,* 1998), and in the infra-diurnal band (I); ω^{-2} shows the roll-off of the GM72 model in the internal-wave continuum (between f and N, indicated below the spectra); resolution bandwidth is 9.4×10^{-2} cpd; the confidence interval is calculated with 16 degrees of freedom obtained from frequency averaging *(Bendat and Piersol,* 1971).

semi-diurnal tidal frequencies (labeled fM_2) is indicative of non-linear interaction between the two bands *(Mihaly et al.,* 1998). The M_4 peak, normally only found in shallow water, was recently observed near a mid-ocean ridge in the northeast Pacific *(ibid).* In some of the spectra the M_4 and the fM_2 peaks are as high as the peaks in the diurnal band. In the pre-warming (and in most of the post-warming) spectra there are no strong near-inertial peaks at 2300 m, but at 1800 m and 2100 m and in nearly all records during passage of the warming event they are significant at the 5% level. (Because the resolution bandwidth is of the order of the separation between K_1 and f the respective contributions are not always separated by spectral gaps.)

Fig. 4.4 shows the spectrum of the temperature fluctuations corresponding to the velocity data of Fig. 4.3. Most of the energy is contained in the low-frequency band, consistent with the 0.1°C warming observed during that part of the record (c.f. Fig. 4.2). The significant

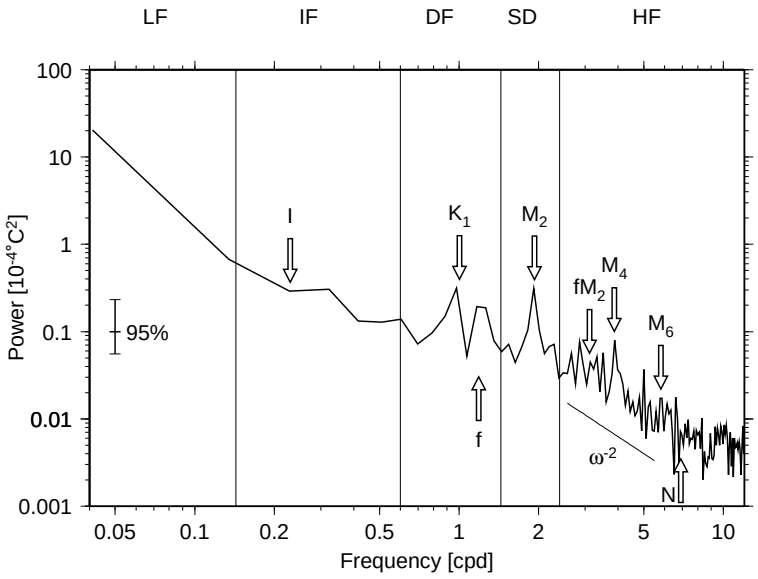

Fig. 4.4: Power spectrum of the temperature fluctuations measured by instrument B23 during passage of the warming event; power is in units of squared temperature; the annotations are the same as in Fig. 4.3.

peaks in the temperature spectrum have corresponding signatures in the flow spectral-energy distribution, especially at the main tidal frequencies and in the near-inertial band. The variability of the spectral-peak magnitudes from different instruments is high, however — in simultaneous spectra at the same depth derived from other instruments, the peak power of the temperature fluctuations in the semi-diurnal tidal band is more than an order of magnitude larger than the one shown without a corresponding increase in the flow spectral energy. This could be either because of more baroclinic structure of the flow (e.g. *Müller et al.*, 1978) or because of higher temperature stratification.

Comparison of the flow and temperature spectra reveals that some of the prominent spectral peaks in the former have only weak or no signatures in the latter. A notable case in point is the peak labeled I at 0.23 cpd. In the flow spectra plotted against a logarithmic frequency axis it appears as a broad and possibly only marginally significant feature. Its bandwidth of 0.3 cpd is in fact similar to that of the M_2 and K_1 peaks. This and similar oscillations are much easier to detect in autocorrelation plots (e.g. Fig. 4.7) than in power spectra.

The autocorrelations show a range of oscillations with periods greater than a day, varying in magnitude and frequency both in time and space. On *Rainbow Sill* (moorings B and

D) periodic motions with frequencies of 0.2–0.3 cpd are observed at 2300 m (and sometimes also at 2100 m but much less clearly so) during all three temporal regimes but they are much weaker after passage of the warming event. (Close inspection of Fig. 4.2 also shows a signature of this oscillation at 2300 m where the daily-averaged velocities are "bunched together" in groups of 4–6.) Near the high-frequency limit of the sub-diurnal band there is a well-defined oscillation with a frequency of 0.8 cpd on the eastern flank of *Rainbow Ridge* (mooring C) increasing with depth during both the pre-warming and the warming regimes and a similar one with a frequency of 0.5 cpd after passage of the event. The regular oscillation with the lowest observed frequency (corresponding to a period of 14 days) is manifest in the records from instruments C18, D18 and F21 during passage of the event. There does not appear to be any preferred polarization of the energy of these oscillations.

Given the enclosed nature of the rift valley below 2000 m it is assumed that at least some of the oscillations with periods greater than a day are free basin modes. Because of the complexity of the patterns this is difficult to confirm, however. Using a range of values for the effective depth of the rift valley and estimating corresponding reduced gravities from Fig. 3.2, the Rossby radius of deformation becomes 1–7 km, i.e. it is smaller than the width of the rift valley at the depth of the current meters, indicating that the effects of rotation cannot be ignored. For large rotation rates, i.e. $f \gg \omega$ where ω is the frequency of the observed oscillations, the free modes of enclosed rectangular or circular unstratified basins with vertical walls are similar to Kelvin waves propagating around the rims of the basins (e.g. *LeBlond and Mysak,* 1978). With the parameters used to estimate the Rossby radius the gravity wave speed becomes 0.1–0.5 $\mathrm{m \cdot s^{-1}}$ which, together with periods between 1 and 14 days, yields a range of horizontal scales of approximately 10–630 km. If the fastest (slowest) waves are assumed to be associated with the shortest (longest) periods this range reduces to 45–120 km which is consistent with the horizontal extent of the *AMAR* segments.

Another type of wave which can potentially account for some of the oscillations are short (compared to the Rossby radius of deformation) topographic planetary (or Rossby-) waves, possibly generated by the vorticity perturbation introduced into the water column by the hydrothermal plume. (Long topographic Rossby waves are barotropic which is inconsistent with the observations, whereas the short waves decay exponentially with distance from the sloping bottom.) The dispersion relation of short topographic Rossby waves in uniformly

Band	Frequency	Period	Significance
LF	0–0.143 cpd	$\geq$1 week	low frequencies
IF	0.143–0.6 cpd	40 h–1 week	free basin modes? topographic Rossby waves?
DF	0.6–1.44 cpd	16.7–40 h	diurnal band (including near-inertial range)
SD	1.44–2.4 cpd	10–16.7 h	semi-diurnal band
HF	2.4–12 cpd	2–10 h	high frequencies

Table 4.1: Current-meter frequency bands.

stratified basins with uniformly sloping bottom boundaries is

$$\omega = -\gamma N \frac{k_l}{(k_l^2 + k_x^2)^{1/2}} \tag{4.1}$$

(e.g. *LeBlond and Mysak,* 1978), where γ is the bottom slope, and k_l and k_x are the along-slope and the cross-slope wave numbers, respectively. The negative sign indicates that k_l is negative, i.e. that the waves propagate in the "topographic westward" direction (with the slope shallowing on their right). Assuming k_l and k_x to be of similar size, taking a value of $N = 5 \times 10^{-4}\,\mathrm{s}^{-1}$ from Fig. 3.7 at 2300 m, and estimating the representative slope of the rift valley at that depth to be approximately 0.1–0.2 (e.g. Fig. 4.9) yields a frequency range of 0.7–1.4 cpd, indicating that short topographic Rossby waves can account for some of the observed oscillations.

4.3.2 Bulk Energy Distribution

The primary goal of the current-meter analysis is an assessment of the variability of the along-valley flow. Inspection of the individual spectra, such as the ones shown in Fig. 4.3, suggests that the flow energy is dominated by contributions from a small number of frequencies, most notably within the low-frequency, the diurnal and the semi-diurnal tidal bands. Because the relative contributions from different frequencies are difficult to compare on log-log plots, the resolved frequency range is subdivided into 5 bands (Figs. 4.3 and 4.4, and Table 4.1). The boundaries between the frequency bands were chosen to coincide with spectral gaps in most records. The diurnal band contains both tidal frequencies and the near-inertial range. The limits of the IF band were selected to encompass the more energetic of the oscillations with periods greater than a day (section 4.3.1). Fig. 4.5 shows the energy partition of the

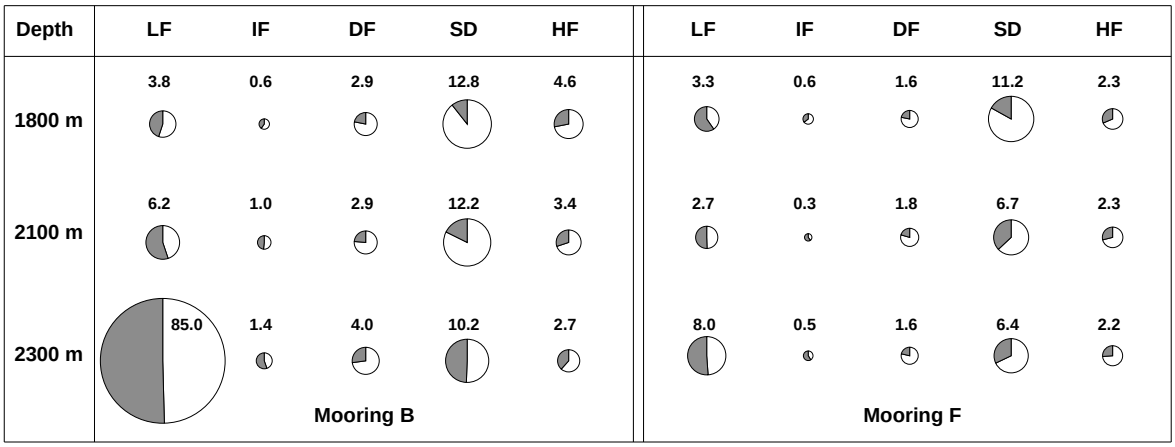

Fig. 4.5: Pre-warming energy partition of the current-meter records of moorings B and F; the limits of the frequency bands are listed in Table 4.1; pie areas are proportional to the energies which are also listed in units of $10^{-4}\,\mathrm{m^2 \cdot s^{-2}}$ above the pies; shading is determined by the relative polarizations with shaded sectors denoting the ACW components.

pre-warming velocities recorded on moorings B and F. Mooring F was selected because it represents the only record for the continuation of the along-valley flow 30 km NE of *Rainbow Sill* (Fig. 2.3).

In the pre-warming records the low-frequency components dominate in the overflow across *Rainbow Sill* (B23, D23), at 2300 m on mooring F, as well as at intermediate depths on the western slope of *Rainbow Ridge* (G21) and at the southernmost mooring in the NE basin (H21). While this pattern changed in a complex way during passage of the warming event, the post-warming energy distribution is similar to the pre-warming state. Within the core of the overflow the pre-warming low-frequency component is nearly an order of magnitude larger than the tidal flow. The oscillations in the IF band are not very energetic in the pre-warming records; during passage of the warming event their contributions become as high as half that of the low-frequency component in the *Rainbow Sill* overflow, however (e.g. Fig. 4.3).

The only current meter mooring deployed on the western slope of *Rainbow Ridge* (G) is also the one closest to (1.5 km north of) the hydrothermal vent field. The flow observations at mooring G indicate a baroclinic structure of the tidal oscillations with the lowest energy at 2100 m, the mean depth of the hydrothermal particle plume (chapter 5). A direct influence of the plume on the dynamics on the western slope of *Rainbow Ridge* cannot be excluded; LADCP observations (section 3.2.3), which can easily be correlated with hydrothermal par-

Depth	Pre-Warming	Warming	Post-Warming
1800 m	0.60	0.45	0.57
2100 m	0.35	0.28	0.35
2300 m	0.13	0.24	0.20

Table 4.2: Depth-averaged rotary coefficients C_r (see text for definition) of the flow observed during the three temporal regimes.

ticle signals, do not show any dynamical plume signatures however and, given the vertical range of the near-source plume observations of the 1997 survey (section 5.2.2) as well as the corresponding horizontal variability (section 5.2.1), it seems doubtful that there should be a strong signature at 2100 m close to the vent field. Topographic effects are therefore considered more likely explanations for the flow recorded on mooring G.

The energy polarization observed at all moorings resembles that shown in Fig. 4.5 with the dominance of the CW polarization decreasing with increasing depth and with decreasing frequency. Preferentially CW-polarized rotary currents at frequencies above approximately 1 cpd have been observed near mid-ocean ridges elsewhere (e.g. *Mihaly et al.,* 1998). The decreasing polarization with increasing depth observed in our data is consistent with topographic steering. The mean flow (and also the energy at the Nyquist frequency) is unpolarized by definition. Table 4.2 shows the mean polarizations during the three temporal regimes in terms of depth-averaged rotary coefficients of the entire spectra $C_r = (S_- - S_+)/(S_- + S_+)$, where S_- and S_+ are the CW- and the ACW-polarized rotary spectral components, respectively *(Gonella,* 1972). Consistent with the observations from individual moorings the mean rotary coefficients decrease with increasing depth. During passage of the warming event the CW dominance decreased at 1800 m and at 2100 m while it increased at 2300 m. (The rotary coefficients at 2300 m are dominated by the low-frequency component of the *Rainbow Sill* overflow.)

4.4 High-Frequency Temperature Variability

From the temperature power spectra RMS amplitudes were calculated for comparison with the temperature variability observed during the hydrographic surveys (chapter 3). Because of the sampling times of the surveys all frequencies outside the LF band were used (Table 4.1).

Depth	B	C	D	E	F	G	H	mean
1800 m	69	59	58	54	45	56	45	55
2100 m	27	32	27	29	24	35	22	28
2300 m	18	24	19	16	13	25	19	19

Table 4.3: RMS temperature amplitudes in units of 10^{-3}°C for periods less than one week.

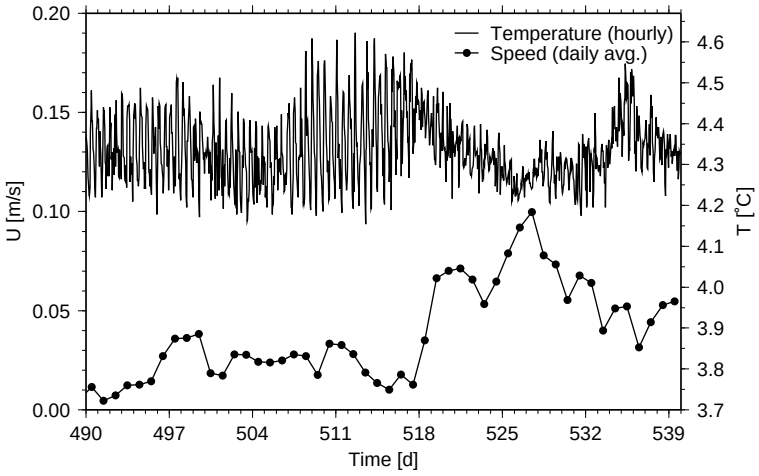

Fig. 4.6: Hourly temperatures and daily-averaged flow speeds of the last two months of mooring deployment recorded by instrument B18.

A comparison between the three temporal regimes indicates no significant differences. Therefore, the variances were calculated from the full records. Table 4.3 shows the resulting values for all instruments as well as depth averages. The temperature variance decreases everywhere with increasing depth and the magnitudes are consistent with the hydrographic surveys. The smallest overall variability is found on moorings F and H, i.e. away from *Rainbow Ridge*.

Fig. 4.6 indicates that the temperature variability was not temporally uniform everywhere, however. The increase in the daily-averaged flow speed between days 517 and 527 marks the onset of the SW-ward flow across *Rainbow Sill* at 1800 m (e.g. Fig. 3.17). In addition to the strong (approximately factor 2) decrease in the high-frequency temperature amplitude, the increase in flow speed is accompanied by a temperature drop of order 0.2°C. Inspection of the hourly velocity measurements reveals no apparent reduction in the high-frequency flow variability. The data recorded by instruments D18 and, to a somewhat lesser extent, G18 show similar features.

	pre-warming				warming				post-warming			
	$\overline{\text{dir}}$	$\overline{\text{U}}$	σ_l	σ_x	$\overline{\text{dir}}$	$\overline{\text{U}}$	σ_l	σ_x	$\overline{\text{dir}}$	$\overline{\text{U}}$	σ_l	σ_x
B21	088	2.1	1.7	1.0	079	3.1	2.1	1.1	081	2.5	2.3	1.5
B23	094	8.7	1.7	1.2	084	4.3	2.0	0.7	092	6.5	2.9	1.3
D21	066	1.1	1.4	0.8	055	2.4	2.8	1.5	066	1.8	2.3	1.4
D23	079	5.9	1.1	0.8	065	2.9	1.6	0.7	074	5.0	2.2	1.0
F21	046	1.1	0.8	0.9	018	0.9	1.5	1.5	055	1.3	1.7	1.3
F23	046	2.5	0.9	0.7	027	1.6	1.1	0.9	049	1.9	1.4	1.2
G21	046	3.6	2.9	1.3	036	4.3	2.6	0.8	044	2.8	3.0	1.1
G23	046	2.6	1.6	0.5	027	2.5	1.2	0.5	031	1.9	1.8	0.7

Table 4.4: Flow statistics for selected current meters; mean directions ($\overline{\text{dir}}$) are given in degrees CW from north; mean flow velocities ($\overline{\text{U}}$), and along-mean (σ_l) and cross-mean (σ_x) velocity standard deviations are listed in units of $10^{-2}\,\text{m}\cdot\text{s}^{-1}$.

4.5 Along-Segment Flow and Transport

4.5.1 Flow Statistics

To assess the characteristics of the along-segment flow a number of statistics were calculated as shown in Table 4.4 for selected instruments. Attention is restricted to depths below 2000 m at the overflow (moorings B and D), on the western flank of *Rainbow Ridge* (mooring G, 3 km upstream of *Rainbow Sill),* and 30 km downstream of *Rainbow Sill* (mooring F). In most records the mean flow direction was similar before and after the warming with some backing observed during the event. During its passage the mean flow across *Rainbow Sill* appears to have shifted upwards in the water column, i.e. it increased at 2100 m and decreased at 2300 m. The data from mooring F are consistent with bottom-intensified continuation of the unidirectional flow along the *AMAR* segments (c.f. chapter 8). The smaller velocities measured there most likely indicate that the flow is of greater lateral extent. The along-mean (σ_l) and cross-mean (σ_x) standard deviations do not show any striking patterns.

The reliability of the mean velocity estimates of Table 4.4 depend on the spectral characteristics of the flow. If there are energetic low-frequency oscillations which are not adequately resolved the calculated mean values may not be representative of the long-term averages. To estimate the energetic time scales of the flow the integral time scales τ_l are calculated by

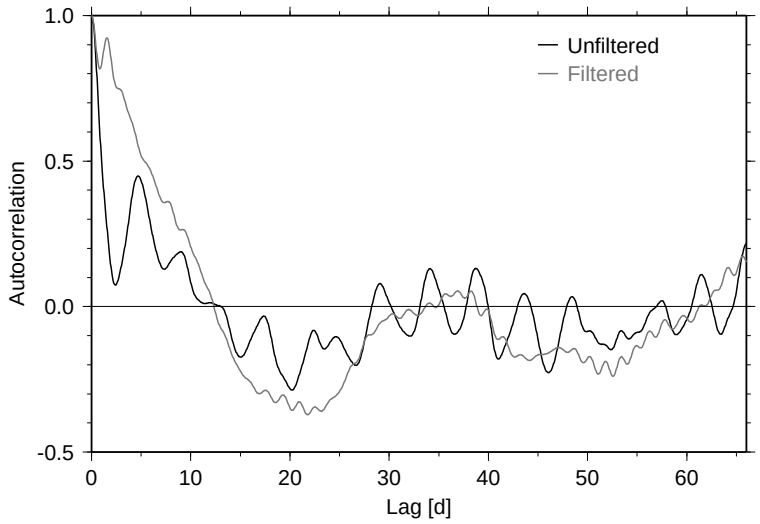

Fig. 4.7: Lagged autocorrelations of the pre-warming along-mean velocity component recorded by instrument B23; correlations for lags greater than half the record length are not shown; the "unfiltered" autocorrelation is derived from all spectral components with frequencies greater than 1 cpd while the frequencies in the IF band (section 4.3) were removed from that range to derive the "filtered" autocorrelation.

Instrument	pre-warming ($T_r = 132$)		warming ($T_r = 135$)		post-warming ($T_r = 105$)	
	τ_l	$\overline{U}$	τ_l	$\overline{U}$	τ_l	$\overline{U}$
B21	7.8	2.1 ± 0.6	8.5	3.1 ± 0.7	14.3	2.5 ± 1.2
B23	5.9	8.7 ± 0.5	4.1	4.3 ± 0.5	4.8	6.5 ± 0.9
D21	1.8	1.1 ± 0.2	8.1	2.4 ± 1.0	7.4	1.8 ± 0.9
D23	4.8	5.9 ± 0.3	4.8	2.9 ± 0.4	5.3	5.0 ± 0.7

Table 4.5: Overflow-mooring integral time scales (τ_l, in units of days) and along-mean velocities ($\overline{U}$, in units of $10^{-2}\,\mathrm{m{\cdot}s^{-1}}$); record durations of the three regimes (T_r, in units of days) are shown as well.

integrating the lagged autocorrelations of the low-pass filtered (to remove tidal fluctuations) along-mean velocity components to the first zero crossings (e.g. *Saunders,* 1987). *Flierl and McWilliams* (1978) show that for red spectra the expected error variance of the mean is (conservatively) approximated by

$$\epsilon = \frac{2\tau_l}{T_r}\sigma_l^2. \tag{4.2}$$

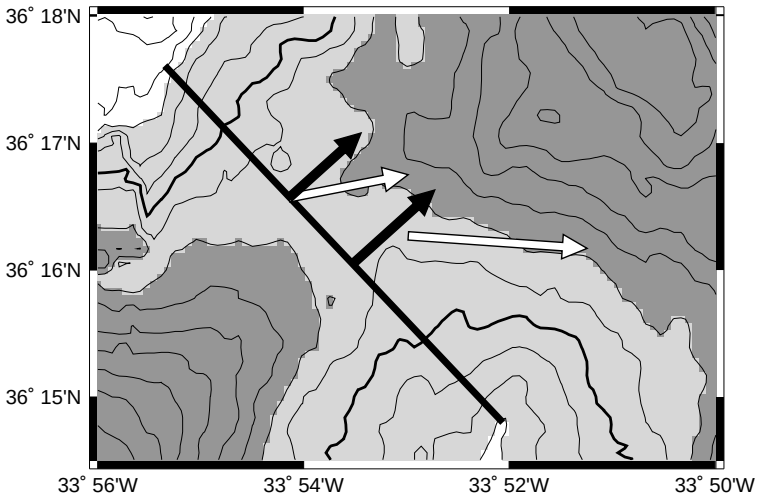

Fig. 4.8: Plan view illustrating the *Rainbow Sill* volume-flux calculations; white arrows show arbitrarily scaled pre-warming current meter measurements at 2300 m; black arrows show the corresponding translated and projected velocities; the heavy straight line indicates the along-sill section (c.f. Fig. 4.9); bathymetric shading is the same as in Fig. 1.2; contour interval is 100 m; the heavy contour marks the 2300 m isobath.

Fig. 4.7 shows the autocorrelation of the pre-warming B23 along-mean flow (labeled "unfiltered"). The deterministic oscillation with a frequency of 0.23 cpd indicates that the spectrum is peaked in violation of the assumptions underlying expression (4.2). Because sub-diurnal oscillations are present in many of the current meter records (section 4.3.1) these were removed by filtering the IF band (Table 4.1) from the "contaminated" records. The resulting "filtered" autocorrelation is shown in Fig. 4.7 as well. Integrating the (filtered where necessary) autocorrelations yields the integral time scales listed in Table 4.5 together with the mean flow velocities and the associated error estimates derived from expression (4.2). The integral time scales are relatively uniform at 2300 m throughout the sampling period while there are large variations at 2100 m. (For comparison, *Saunders* (1987) reports values around 3 days derived from flow measurements characterized by similar statistics in Discovery Gap.)

4.5.2 Volume Flux Across *Rainbow Sill*

The cross-sill velocities of Table 4.5 are now used to calculate volume-flux estimates for the *Rainbow Sill* overflow below 2000 m. To this purpose a section along the sill is defined between the northern tip of the 2000 m bathymetric contour of *Rainbow Ridge* and the western rift-valley wall, mooring B is translated along isobaths onto that section, and the velocities are

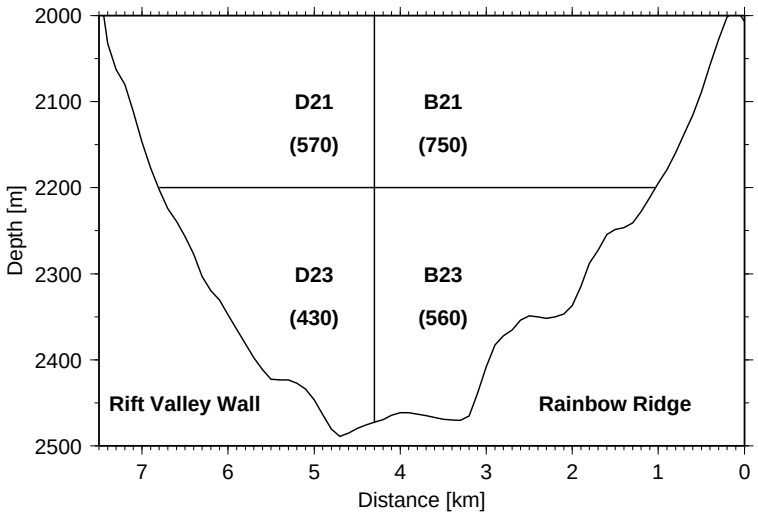

Fig. 4.9: *Rainbow Sill* cross-valley section (heavy line in Fig. 4.8); distance is measured from *Rainbow Ridge*; in addition to the instrument labels printed at the locations of the current meters the cross-sectional surface areas of the four boxes (in units of $10^3\,\mathrm{m}^2$) are given in parenthesis.

	pre-warming	warming	post-warming
best	$73.2(\pm 7.7) \times 10^3\,\mathrm{m}^3\cdot\mathrm{s}^{-1}$	$65.6(\pm 14.4) \times 10^3\,\mathrm{m}^3\cdot\mathrm{s}^{-1}$	$71.2(\pm 18.4) \times 10^3\,\mathrm{m}^3\cdot\mathrm{s}^{-1}$
upper	$92.1(\pm 9.7) \times 10^3\,\mathrm{m}^3\cdot\mathrm{s}^{-1}$	$73.1(\pm 16.2) \times 10^3\,\mathrm{m}^3\cdot\mathrm{s}^{-1}$	$84.3(\pm 21.2) \times 10^3\,\mathrm{m}^3\cdot\mathrm{s}^{-1}$
lower	$50.4(\pm 4.6) \times 10^3\,\mathrm{m}^3\cdot\mathrm{s}^{-1}$	$43.9\ (\pm 9.1)\ \times 10^3\,\mathrm{m}^3\cdot\mathrm{s}^{-1}$	$48.7(\pm 11.7) \times 10^3\,\mathrm{m}^3\cdot\mathrm{s}^{-1}$

Table 4.6: *Rainbow Sill* volume-flux estimates.

projected on the cross-sill direction (48°). These steps are illustrated with the pre-warming velocities at 2300 m in Fig. 4.8. The cross-valley section below 2000 m is divided into 4 boxes as illustrated in Fig. 4.9. There is one velocity estimate in each box which is taken to represent its mean velocity. The resulting transport estimates across *Rainbow Sill* are listed in the first row of Table 4.6, labeled "best".

In addition to the error bars of the transport estimates derived from the errors associated with the mean velocities (Table 4.5), there are additional uncertainties because of the small spatial sampling resolution and the details of the flux calculation. It can be argued that the flow recorded on mooring B should be anticlockwise rotated before projection because of possible flow curvature (following the isobaths) between the true and the translated mooring positions (Fig. 4.8). The appropriate amount of rotation is difficult to estimate but an upper

bound for the transport (assuming that there are no other effects low-biasing the estimates) can be derived by repeating above calculations using the along-mean velocities of mooring B without projection. The resulting volume-flux estimates are listed in the second row of Table 4.6, labeled "upper".

The assumption that each velocity estimate is representative of the mean within the corresponding cross-sectional box (Fig. 4.9) also results in considerable uncertainties associated with the volume-flux estimates. Because both current-meter moorings are located near the center of the channel, away from the lateral boundaries, the velocity estimates are most likely biased high. To derive a lower bound for the transport the cross-sill velocities are assumed to decrease linearly between the moorings and the lateral boundaries where they vanish. Between the moorings the velocities are assumed to vary linearly. The corresponding transport is calculated by partitioning the cross-valley section (Fig. 4.9) into 6 boxes with the moorings defining the lateral boundaries between the boxes. The velocities of the two central boxes are set to the mean (projected) velocities of the two instruments on either side and the velocities of the remaining 4 boxes are set to half the observed velocities of the single current meters on their boundaries. The resulting volume-flux estimates are listed in the third row of Table 4.6, labeled "lower".

The estimated range of the transport across *Rainbow Sill* is 40–100 $\times 10^3\,\mathrm{m}^3\cdot\mathrm{s}^{-1}$ during the entire year, consistent with the $65 \times 10^3\,\mathrm{m}^3\cdot\mathrm{s}^{-1}$ estimated from a hydraulic model (section 3.2.3). It is interesting to note that the "best" estimate is associated with the smallest overall temporal variability (10%).

4.6 Discussion

The array of moored current meters provide a vast amount of information on the variability of the flow in the vicinity of *Rainbow Ridge* on a range of time scales spanning hours to months. While the overall patterns of the hydrographic analysis are confirmed, the current meter data indicate that the situation is far more complex than the gross hydrographic patterns suggest. The main goal of the current meter data analysis in the context of this thesis is the characterization of the low-frequency variability and its influence on the advective transport of the hydrothermal tracers away from the vent field. (Detailed analysis of the high-frequency motions in our data set is outside the main focus of the project but there are many intriguing

observations which merit further investigation at a future stage.)

No dynamical signal unambiguously associated with the hydrothermal buoyancy flux was observed in our data. The complexity of the spatial and temporal patterns of the energetic motions in the rift valley preclude the application of simple tests and the problem of detecting plume signals appears even more difficult than on slow-spreading ridges where hydrothermal plumes rise well above the topography but where attempts at detecting dynamical signals associated with large plumes have only recently been successful, requiring velocity profiles from a moored ADCP *(Joyce et al.,* 1998). Within the rift valley of the MAR the problem is compounded by an apparent lack of theoretical, numerical and laboratory investigations into the behavior of buoyancy sources on steep slopes acting both as lateral and as bottom boundaries.

The estimates for the volume flux across *Rainbow Sill* are intriguing because they suggest that in spite of the flow variability on all observed scales the along-valley transport below 2000 m remained nearly constant throughout the year. (Overflow currents showing little variability over time scales of years have been observed elsewhere, e.g. by an array of current meters deployed for two years in the East Greenland Current downstream of Denmark Strait *(Dickson et al.,* 1990).) The estimates for the transport across *Rainbow Sill* agree well with the hydraulic calculations of chapter 3. These observations are used in chapter 8 to derive mass and heat budgets for the *AMAR* segments. If the quasi-steady view is correct, implying that the transient warming event in the overlying water column changed the flow patterns without strongly affecting the magnitude of the along-valley transport, the question concerning the forcing of the mean flow (c.f. section 3.4) becomes even more important. In chapter 9 this question is addressed with a simple analytical and numerical model.

Chapter 5

Hydrothermal Particle-Plume Observations

5.1 Introduction

In this chapter the particle-plume observations of the two quasi-synoptic surveys of the 1997 *FLAME* (section 2.1) and the 1998 *FLAME-2* (section 2.2) cruises are presented. The main goal is to investigate the horizontal and vertical distribution of the hydrothermal particle anomalies in the water column in the vicinity of the *Rainbow* vent field (Fig. 1.4).

When the first hydrothermal plumes were discovered in the Galapagos rift it was noted that some of the temperature anomalies were associated with small transmissometry signals *(Weiss et al.,* 1977). Subsequent discovery and investigation of high-temperature vent fields revealed that metal-rich hydrothermal effluents give rise to particle plumes, consisting primarily of precipitated metal sulfides and oxides (e.g. *Feely et al.,* 1987). Because high particle loads in the water column can readily be detected with transmissometers and nephelometers (measuring light scattering), these instruments are used extensively to track hydrothermal plume dispersal (e.g. *Baker et al.,* 1985), to prospect for new vent fields (e.g. *German et al.,* 1996b), and to investigate the temporal variability of hydrothermal plumes (e.g. *Baker,* 1994; *Rudnicki et al.,* 1994). More quantitatively, optical anomalies have been calibrated against total particle loads (e.g. *Baker et al.,* 1985) and against concentrations of hydrothermal geochemical tracers (e.g. *Nelsen et al.,* 1987).

There are a number of inherent problems associated with optical particle measurements,

however. Different instruments measure different optical properties such as light transmission and scattering at different angles and wavelengths. The optical properties of the water column depend on the total particle loads, the particle size fractions, and on the surface properties (shape, reflectance, etc.) of the particles (e.g. *Baker and Lavelle,* 1984). The surface properties of hydrothermal particles depend on the chemical composition of the source fluid. Therefore, separate calibrations are required for each study and every instrument. Optical instruments furthermore tend to 'fog' resulting in calibration shifts with time; this is especially problematic during long tow-yo casts (e.g. *Thomson et al.,* 1992).

Plume-dispersal studies based on optical particle observations are further hampered by variable particle behavior. Different studies have shown near-constant particle loads on time scales of months in some plumes (e.g. *Lupton et al.,* 1998), rapidly (order of days) decreasing particle concentrations because of sedimentation and dissolution in others (e.g. *Baker and Massoth,* 1987; *Kadko et al.,* 1990), and even increasing particle loads, presumably because of in-situ precipitation continuing for days after release of the effluents (e.g. *Baker et al.,* 1995). Particles settling out of hydrothermal plumes have been inferred to be recycled by re-entrainment (e.g. *German and Sparks,* 1991; *Lane-Serff,* 1995; *Rudnicki,* 1995) and sedimentation has been shown to be potentially important for the dynamics of non-buoyant plumes (e.g. *Hoyal et al.,* 1999).

In the vicinity of hydrothermal vent fields particle distributions in the water column are often highly inhomogeneous (e.g. *Nelsen et al.,* 1987; *Rudnicki and Elderfield,* 1992). Sometimes there are significant differences between a profile's down- and upcasts (e.g. *Radford-Knoery et al.,* 1998). Vertical structure in near-field hydrothermal particle distributions has been attributed to layering caused by multiple sources (e.g. *Rudnicki and Elderfield,* 1992), to time-varying buoyancy fluxes and background flow fields (e.g. *Thomson et al.,* 1989), and to turbulent plume structure (e.g. *Nelsen et al.,* 1987). Spatial variability in conjunction with contouring can lead to misinterpretations concerning the number of hydrothermal sources giving rise to observed particle distributions (e.g. *Rudnicki et al.,* 1995; *James et al.,* 1995).

The background particle load of the water column is not constant, with both biogenic inputs from the euphotic zone and sediment resuspension in the bottom boundary layer influencing the distributions (e.g. *Eittreim et al.,* 1976). Optical anomalies alone are therefore not necessarily reliable indicators for hydrothermal processes, especially in the presence of strong flows and in the vicinity of topography as is the case in the *AMAR* segments.

Because of these observations the particle distributions observed during the two quasi-synoptic surveys are analyzed qualitatively in this chapter (in chapter 6 the optical measurements are quantified by their associated hydrographic anomalies). In section 5.2 the light-scattering observations of the 1997 survey are presented. The hydrothermal particle plume rising into the boundary current flowing along the western slope of *Rainbow Ridge* is advected northwards away from the vent field, across *Rainbow Sill* and into the NE basin where it appears to detach from the eastern slope of *Rainbow Ridge* and to enter the NE basin interior. Optical anomalies consistent with the hydrothermal plume are detected up to the limit of the survey, 30 km from the vent field. Density-averaged nephelometry profiles show the particle anomaly distribution to be Gaussian in depth, even in the near-field where many of the individual profiles are characterized by multiple peaks.

In section 5.3 the light-scattering observations of the 1998 survey are presented. During the *FLAME-2* cruise the strongest particle anomalies were observed SW of the vent field away from *Rainbow Ridge* and approximately 100 m higher in the water column than during the 1997 survey, whereas the particles in the vicinity of *Rainbow Ridge* were observed further down in the water column. This bipartition of the hydrothermal particle plume is consistent with the current-meter observations which indicate strongly sheared flow in the vicinity of the vent field. The chapter concludes with a discussion in section 5.4.

5.2 1997 Survey *(FLAME)*

5.2.1 Horizontal Particle Distribution

Fig. 5.1 shows the horizontal distribution of the depth-integrated *BRIDGET* nephelometry profiles of the 1997 survey. (The entire data set is shown, including the tows with the faulty CTD instrument; see section 2.1). In the SW basin the plume signals are confined to the area north of the vent field, consistent with the currents recorded on mooring G during the first week of deployment, i.e. immediately after the end of the *FLAME* cruise (Fig. 5.2). A representative width of the plume is difficult to estimate but the value of 2 km given by *German et al.* (1998) is most likely good at least within a factor of two. Upstream of *Rainbow Sill* the horizontal variability between neighboring profiles is highest, whereas downstream, on the eastern slope of *Rainbow Ridge*, the depth-integrated plume signals are more uniform. The drop-off in signal strength away from the ridge (east of 33°50′W) is consistent with

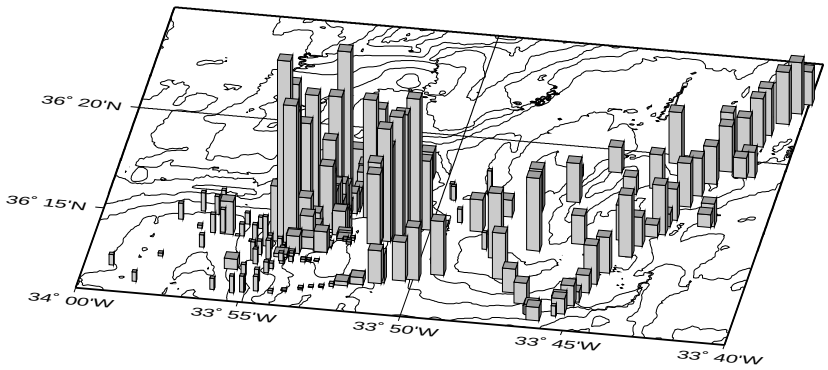

Fig. 5.1: Depth-integrated (1500–2500 m) nephelometry profiles of the 1997 *BRIDGET* data set (arbitrary vertical scale); bathymetric contour interval is 250 m; thin bars denote profiles without plume signals (from visual inspection).

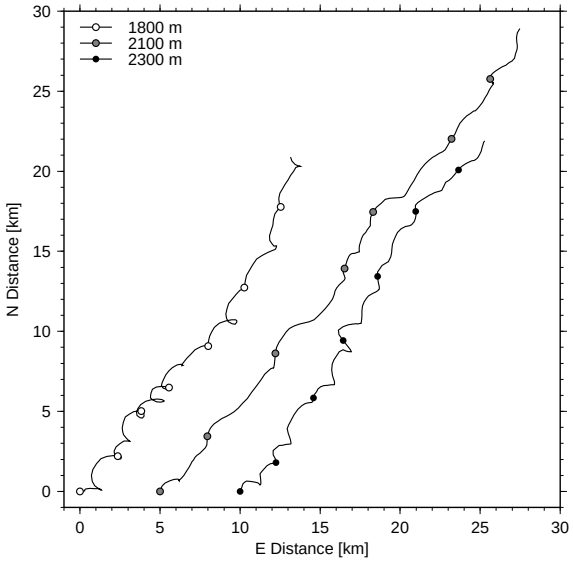

Fig. 5.2: Progressive vector diagrams showing the first week of hourly flow measurements at mooring G (Fig. 2.3); the 2100 m and 2300 m curves are horizontally offset by 5 km and 10 km, respectively; symbols are drawn at midnight GMT.

horizontal mixing (the drop-off coincides with the boundary between the ridge slope, where hydrographic interleaving was observed (section 3.2.2), and the basin interior, where no such structures are apparent). Particle settling and dissolution provide alternative mechanisms for the decrease in plume nephels — the small flow velocities in the NE basin (e.g. Fig. 3.5) are consistent with increased sedimentation rates. East of *Rainbow Ridge* the integrated plume signals decrease south of $\approx 36°15'$N, suggesting that the plume does not follow the isobaths

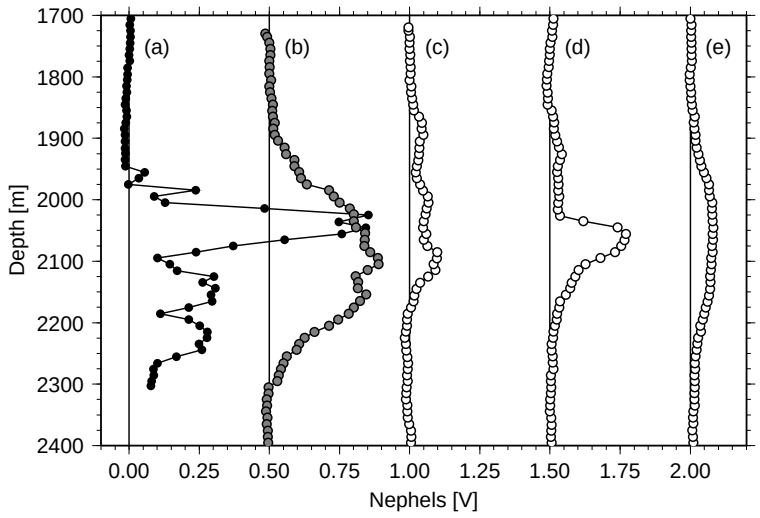

Fig. 5.3: Selected *BRIDGET* nephelometry profiles, including the one closest (< 200 m) to the vent field (a), one from the eastern slope of *Rainbow Ridge* (b), two adjacent ones from the same tow-yo near the center of the NE basin (c) & (d), and the one farthest away (≈ 30 km) from the vent field (e); successive profiles are horizontally offset by 0.5 V.

around the southern edge of the basin, consistent with the methane data shown by *German et al.* (1998).

A plot of the horizontal distribution of the nephelometry *maxima* is similar to Fig. 5.1, the main difference being a reduction in signal strength of approximately 50% across *Rainbow Sill* (c.f. Fig. 5.4), consistent with vertical mixing.

5.2.2 Individual Nephelometry Profiles

Based on the horizontal distribution of the nephelometry anomalies, the *BRIDGET* plume data (thick bars in Fig. 5.1) were separated into three regions: SW basin, eastern slope of *Rainbow Ridge*, and NE basin interior (east of 33°50′W). Fig. 5.3 shows nephelometry profiles from each of these regions, selected to illustrate the variability throughout the domain of observation.

In the near-source profiles (upstream of *Rainbow Sill)* the nephelometry anomalies are confined between 2300 m (the depth of the vent field) and 1900 m. They typically contain one to four peaks in the vertical with the signal between peaks often dropping to background values. In the *Rainbow* data sets, the individual nephelometry peaks cannot be correlated between profiles, suggesting that the horizontal scale of the coherent plume fluid structures

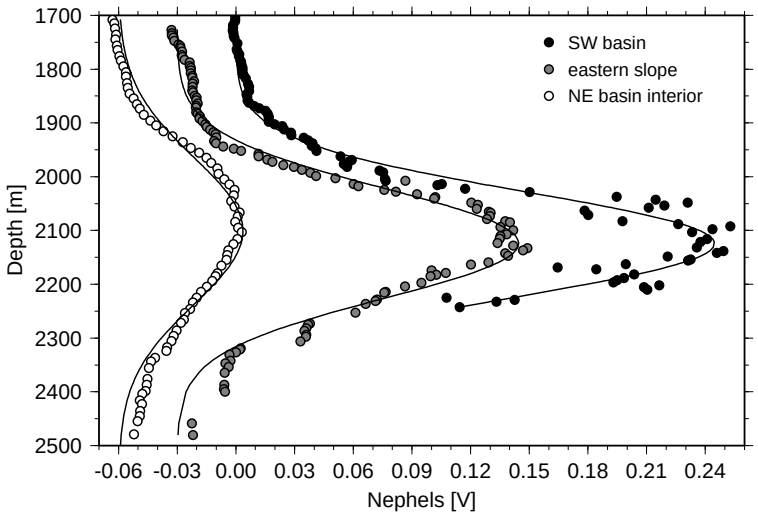

Fig. 5.4: Density-averaged *BRIDGET* plume nephelometry profiles and depth-fitted Gaussian curves for the SW basin (black), the eastern slope of *Rainbow Ridge* (gray, offset by -0.03 V) and the interior of the NE basin (white, offset by -0.06 V); the SW/slope/NE profiles are derived from 26/17/68 casts, respectively; the SW basin profile is truncated at 2250 m below which there are not enough data points (less than four per bin) to calculate meaningful averages.

is small (typical *BRIDGET* tow-yo spacing at plume depth is 1–2 km).

5.2.3 Mean Particle Plume

For each of the three regions (SW basin, eastern slope of *Rainbow Ridge*, and NE basin interior), a mean profile derived from the *BRIDGET* plume data set is shown in Fig. 5.4. Because of the variability of the hydrography on tidal time scales which has a vertical scale comparable to the thickness of individual near-source nephelometry peaks (section 3.2.3), averaging of both nephels and depth was performed in potential-density space with non-uniform bin sizes depending on the stratification. All three mean profiles are approximately Gaussian in depth, even the near-source one from the SW basin which is derived from vertically structured individual profiles such as profile (a) of Fig. 5.3. The Gaussian curve fitted to the SW basin profile is centered at $\mu = 2120$ m, with a thickness (one standard deviation) of $\sigma = 96$ m, a peak value of $\Delta n^* = 0.25$ V and an RMS error of 0.018 V; the respective values for the profile from the eastern slope of *Rainbow Ridge* are $\mu = 2120$ m, $\sigma = 102$ m, $\Delta n^* = 0.18$ V, and RMS error 0.009 V; and those for the NE basin interior profile are $\mu = 2100$ m, $\sigma = 137$ m, $\Delta n^* = 0.06$ V, and RMS error 0.004 V, respectively. The peak of the mean plume exhibits no

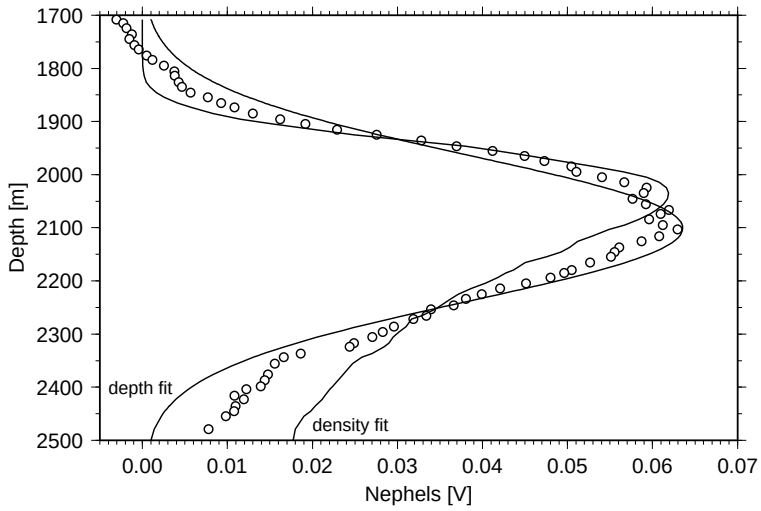

Fig. 5.5: Re-plot of the mean nephelometry profile and depth-fitted Gaussian of the NE basin interior (Fig. 5.4) with added Gaussian fitted in density-space.

vertical trend with distance from the source (neither in depth nor in density space), indicating that the profiles of Fig. 5.4 represent the *equilibrium plume* (neutrally buoyant without vertical momentum). The rise height measured at the mean nephelometry maximum is 200 m. There is no evidence for vertical overshoot (plume cap) near the source consistent with laboratory (e.g. *Helfrich and Battisti,* 1991) and numerical (e.g. *Lavelle,* 1997) experiments which show that both rotation and cross flows tend to suppress such an overshoot.

The two mean profiles from the NE basin (and, to a lesser extent, the SW basin profile as well) show consistent skews with respect to their depth-fitted Gaussians, with steeper vertical gradients at the top of the plume, indicating that it might be more appropriate to fit the Gaussians in density space — the curvature of density against depth is greater than that implied by the plume skew however, so that the mean plume lies between the two Gaussians as shown in Fig. 5.5 for the NE basin interior profile.

5.3 1998 Survey *(FLAME-2)*

During the 1998 survey 10 CTD stations were occupied in the *Rainbow* region (Fig. 2.2). The variability of the particle distribution observed in 1997 (Fig. 5.1) implies that the 1998 data set is not sufficient to derive an integrated view of the hydrothermal plume. Fig. 5.6 shows the horizontal distribution of the depth-integrated nephelometry profiles. Because of the different

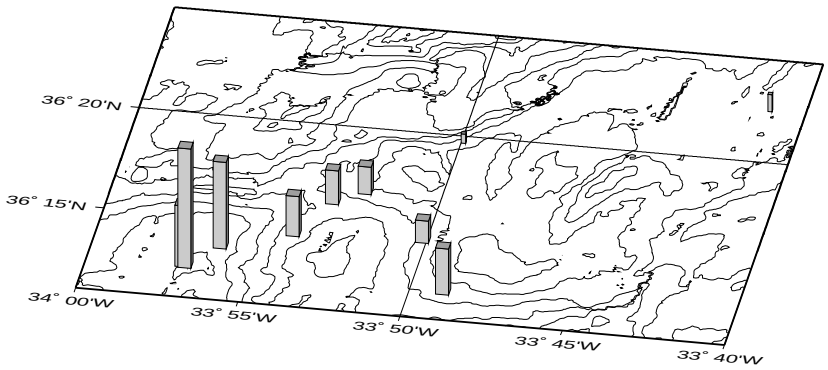

Fig. 5.6: Depth-integrated (1800–2500 m) nephelometry profiles of the *FLAME-2* (1998) data set (arbitrary vertical scale); bathymetric contour interval is 250 m; thin bars denote profiles without plume signals (from visual inspection).

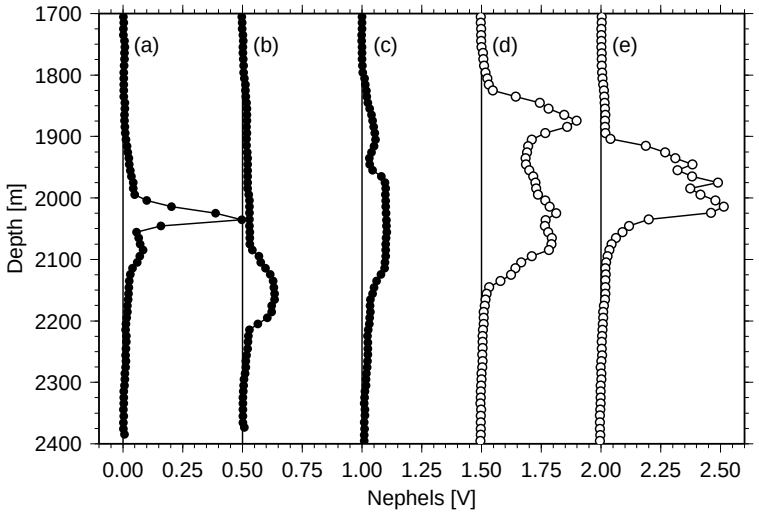

Fig. 5.7: Selected *FLAME-2* nephelometry profiles, including the one closest (1.5 km distance) to the vent field (a), one from the saddle of *Rainbow Sill* (b), one from the embayment east of *Rainbow Ridge* (c), and two from the interior of the SW basin (d) & (e); successive profiles are horizontally offset by 0.5 V.

instruments used during the two surveys (sections 2.1 and 2.2) the optical responses cannot be compared directly. Nevertheless, there are qualitative differences between the particle distributions observed during the two surveys. The strongest particle anomalies in 1998 were recorded SW of the vent field where no plume signatures had been observed in 1997 (c.f. Fig. 5.1). Fig. 5.7 shows a selection of the individual nephelometry profiles. The rise height of the plume is not well defined but the main particle anomalies NE of the vent field (a

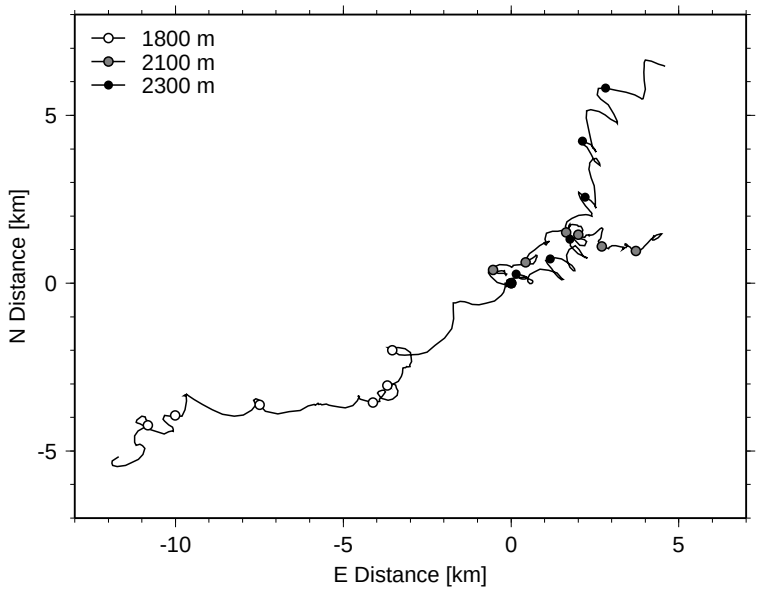

Fig. 5.8: Progressive vector diagrams showing the last full week of hourly flow measurements at mooring G (Fig. 2.3); symbols are drawn at midnight GMT.

and b) are observed below 2000 m whereas the plume in the interior of the SW basin (d and e) spans the depth range between 1800 m and 2150 m, i.e. up to 100 m shallower than the highest light-scattering anomalies observed in 1997. The current-meter data shown in Fig. 5.8 provide a plausible explanation for the observed particle distribution. In the week prior to the 1998 survey the velocity field near the plume source was strongly sheared with mean NE-ward and SW-ward flows at 2300 m and 1800 m, respectively. The buoyant plumes rising into this sheared current field were therefore bisected with only the upper (i.e. more buoyant) portions reaching the SW-ward flow regime. (It will be noted that profile c of Fig. 5.7 from the embayment east of *Rainbow Ridge* contains weak particle anomalies up to 1800 m. From our data the origin of these particles cannot be determined.) The limited sampling achieved during the 1998 survey is insufficient to determine the pathways of the particles beyond the immediate vicinity of *Rainbow Ridge*. It is also not clear if the range in magnitude of the observed light-scattering anomalies is representative, but it does not appear unreasonable that water parcels with the highest concentrations of hydrothermal effluents (indicated by high particle loads; c.f. chapter 6) rise highest, as Fig. 5.7 appears to suggest.

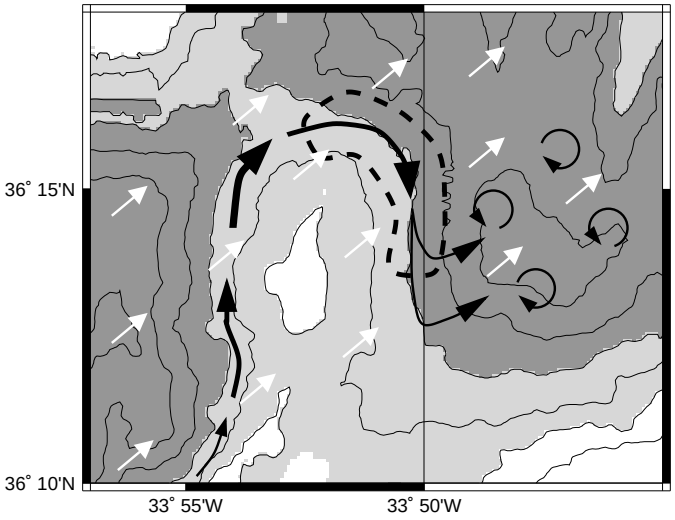

Fig. 5.9: Sketch of the mean flow regime around *Rainbow Ridge* during the 1997 survey; topographic shading is the same as in Fig. 1.2; contour interval is 250 m; black arrows represent the flow below 2000 m; the black dashed line indicates the region where enhanced mixing is expected; white arrows represent the flow above 2000 m.

5.4 Discussion

Using the hydrothermal particles as natural tracers allows the flow downstream of the vent field to be determined in greater detail than is possible from the hydrographic and direct flow observations alone (chapters 3 and 4). The data sets suggest a circulation in the vicinity of *Rainbow Ridge* during the 1997 survey as shown schematically in Fig. 5.9. The incident current below 2000 m flows along the western slope of *Rainbow Ridge* and across *Rainbow Sill* which acts as a hydraulic control point. Downstream of the sill the current descends into the NE basin while continuing to flow clockwise around the ridge. There is enhanced mixing in the downslope current which gradually decreases in strength. Eventually, it detaches from the eastern slope of the ridge, carrying particle-rich water into the interior of the basin. Above 2000 m, the mean incident current flows over the peak of *Rainbow Ridge*. Because the density-averaged plume observed in 1997 extended above the minimum depth of the blocking topography, a fraction of the near-source plume may have been advected over the peak of *Rainbow Ridge*.

During the 1998 survey the situation was similar at depth but the flow above 2000 m had reversed. The boundary current along the western slope of *Rainbow Ridge* was therefore

strongly sheared, bisecting the plume. Only its lower part followed the topography around *Rainbow Ridge* into the NE basin whereas the upper part was carried into the interior of the SW basin. The continuation of the SW-ward flow is not known but it appears possible that at least some of the hydrothermal effluents could have been advected across the rift-valley wall into the western North Atlantic.

Upstream of *Rainbow Sill*, close to the hydrothermal source, many nephelometry profiles of both surveys are characterized by multiple vertical peaks. Laboratory observations (e.g. *Papantoniou and List,* 1989) and numerical models (e.g. *Lavelle,* 1997) show that even plumes rising from single steady buoyancy sources into quiescent backgrounds are characterized by highly inhomogeneous near-source effluent concentrations, indicating that such variability is an intrinsic property of turbulent plumes. Our 1997 data show for the first time that a temporally and spatially averaged hydrothermal particle plume can be Gaussian in depth. This suggests that the particle distribution reflects turbulent plume structure (as opposed to layering caused by multiple sources or non-conservative particle behavior), consistent with the findings of chapter 6, where it is shown that the particle anomalies of the *Rainbow* hydrothermal plume are proportional to the hydrographic anomalies in the water column.

The density-averaged plume is not exactly Gaussian in depth, however. The slight but consistent skew with steeper gradients at the top of the plume is reminiscent of the tracer distributions shown by *Ledwell et al.* (2000), indicating that similar processes may have been responsible for the shape of the mean hydrothermal particle plume observed in 1997.

Chapter 6

Geothermal Hydrographic Anomalies

6.1 Introduction

In this chapter the hydrographic anomalies associated with the *Rainbow* hydrothermal plume are analyzed in detail. The main goal is to quantify the temperature anomalies which are used to calculate the high-temperature convective heat flux from the hydrothermal plume observations of 1997 (chapter 7).

Both conductive heating and hydrothermal circulation contribute to the geothermal heat flux to the ocean, with the latter dominating near the axes of mid-ocean ridges (e.g. *Stein and Stein,* 1994). Conductive geothermal heating increases the water temperature, which implies a decrease in density. Hydrothermal circulation introduces heat into the water column as well but the resulting hydrographic signatures are often complicated by salinity anomalies in the hydrothermal effluents. Depending on the buoyancy flux, the background stratification and the flow field, the effects of geothermal heating can be distributed in the water column by a combination of turbulent diffusion and convective plumes. Entrainment of background fluid into buoyant plumes results in vertical transport of heat and salt, further complicating the hydrographic signatures.

Geothermal hydrographic anomalies have been used to detect hydrothermal vent fields (e.g. *Rona et al.,* 1974; *Weiss et al.,* 1977), to calculate heat fluxes (e.g. *Baker and Massoth,* 1987; *Thomson et al.,* 1992; *Helfrich et al.,* 1998), to estimate effluent dilutions in hydrother-

mal plumes (e.g. *Lupton et al.,* 1985), to determine mid-depth circulation pathways (e.g. *Reid,* 1982), to estimate age differences of abyssal water *(Joyce et al.,* 1986), and to assess geothermal effects on basin-scale circulation patterns (e.g. *Stommel,* 1982; *Joyce and Speer,* 1987; *Hautala and Riser,* 1993; *Thompson and Johnson,* 1996).

In order to isolate the geothermal anomalies a *hydrographic background* must be defined. In regions of small temporal and spatial variability this background can be taken from stations which are free from the geothermal signatures being studied (e.g. *Helfrich et al.,* 1998). Where this is not feasible the background must be estimated from the geothermally modified profiles. Two methods which have been used for this purpose are based on the observation that geothermal processes produce anomalies in otherwise linear background T/S *(Weiss et al.,* 1977) and T/ρ *(Lupton et al.,* 1985) relationships. The resulting hydrographic anomalies will be called *isohaline* (in salinity space) and *isopycnal* (in density space), respectively. Interpretation of isopycnal and isohaline anomalies in the vicinity of hydrothermal vent fields is often difficult because the anomalies can be caused by the integrated effects of a range of geothermal processes, both local and distant in space and time. *Joyce et al.* (1986), for example, use the basin-scale distribution of isohaline temperature anomalies in the abyssal North Pacific to derive water-age differences of the order of 100 years while closely related isopycnal anomalies (section 6.3) are sometimes used to derive heat flux estimates for nearby hydrothermal vent fields, assuming that local effects dominate (e.g. *Baker and Massoth,* 1987). Even if the observed anomalies are caused entirely by processes associated with the nearby vent fields, the potential for plume-fluid re-circulation complicates their interpretation (e.g. *Thomson et al.,* 1992).

The total geothermal heat content of the water column is equal to the spatially integrated *isobaric* (in pressure or depth space) temperature anomalies. Spatially integrated isopycnal and isohaline anomalies, on the other hand, are not equal to the heat content, because of the geothermal effects on the density and salinity fields, respectively (e.g. *McDougall,* 1990). Sometimes, isohaline anomalies are used as a substitute for isobaric anomalies (e.g. *Joyce et al.,* 1986; *Thomson et al.,* 1995). Isohaline and isobaric anomalies are equal if there are no geothermal effects on the salinity field, i.e. in the absence of salinity anomalies in the hydrothermal effluents (if any) and without vertical salinity fluxes in convective plumes. Therefore, isohaline temperature anomalies are particularly useful for the calculation of conductive geothermal fluxes.

In section 6.2 the hydrographic effects caused by hydrothermal plumes are discussed using an expression derived by *McDougall* (1990) which indicates that both cold/fresh and warm/salty anomalies are possible independent of the sign of the background salinity stratification. In section 6.3, it is shown that methods based on T/S and T/ρ linearity are equivalent, and that isohaline temperature anomalies are equal to the corresponding isopycnal anomalies corrected with the expression of *McDougall* (1990). In section 6.4, a new anomaly definition (and an associated method) is presented which uses the limits of the hydrothermal particle anomalies to determine the hydrographic background properties of individual profiles. Applying the new method to the 1997 CTD data, the corresponding light-scattering and isopycnal temperature anomalies are found to be linearly correlated within individual profiles. This observation is used to develop a second new method which determines the hydrographic background from measurements within the hydrothermal particle plume (section 6.5). Close agreement of the vertical structure of the corresponding light-scattering and temperature anomaly profiles in the data sets from the two surveys and the mutual consistency of the near-field anomaly regressions indicate that the distribution of both properties in the *Rainbow* plume is determined by dilution of the hydrothermal effluents (section 6.6). A comparison of the hydrographic anomalies derived with the new methods to those defined as deviations from hydrographic trends in the water column overlying three Pacific plumes indicates that heat anomalies derived with the "traditional" method can be dominated by signatures not associated with hydrothermal particle plumes (section 6.7). The chapter concludes with a discussion in section 6.8.

6.2 Isopycnal Hydrographic Anomalies

Early hydrothermal plume studies were made in the Pacific where the *equilibrium plumes* (neutrally buoyant without vertical momentum) are characterized by positive isopycnal and isobaric temperature anomalies (e.g. *Weiss et al.*, 1977). Based on numerical experiments (e.g. *McDuff*, 1988; *Baker et al.*, 1989) it was soon realized that the relationship between the heat fluxes at the equilibrium level and at the source is non-trivial because it depends on the background hydrography as well as on the hydrothermal effluent properties. Observation of negative temperature anomalies in the Atlantic *(Rona and Speer*, 1989) prompted *Speer and Rona* (1989) to investigate this relationship. They showed that because of the unstable salinity

gradient in the deep Atlantic (e.g. Fig. 3.3) hydrothermal plumes rising from sources without salinity anomalies are characterized by cold/fresh hydrographic anomalies. *McDougall* (1990) extended their work by taking variable source salinities into account and derived an analytical expression for the resulting isopycnal hydrographic anomalies. (In an earlier study, *Turner and Campbell* (1987) had investigated the condition for buoyancy reversal in rising plumes caused by the non-linearity of the equation of state at high temperatures *(Bischoff and Rosenbauer,* 1985) to occur, finding that large positive source salinity anomalies are required.) If the T/S relationship of the fluid entrained into the buoyant plume is linear, the equilibrium-plume temperature anomaly flux $Q_e\overline{\Delta\theta_e}$ is related to the corresponding source temperature anomaly flux $Q_i\overline{\Delta\theta_i}$ by

$$\frac{Q_i\overline{\Delta\theta_i}}{Q_e\overline{\Delta\theta_e}} = -\frac{R_\rho - 1}{1 - R_\rho/R_\rho^i} \tag{6.1}$$

(from expression (22) of *McDougall,* 1990). Q_i and Q_e denote the volume fluxes at the source and in the equilibrium plume, respectively; $\overline{\Delta\theta_i}$ and $\overline{\Delta\theta_e}$ are the corresponding mean temperature anomalies; $R_\rho = \alpha\theta_z/(\beta S_z)$ is the stability ratio of the water column (with α and β denoting the linear thermal expansion and haline contraction coefficients evaluated at the reference pressure of potential temperature, respectively); $R_\rho^i = \alpha\overline{\Delta\theta_i}/(\beta\overline{\Delta S_i})$ is the density-anomaly ratio of the hydrothermal source fluid (with $\overline{\Delta S_i}$ denoting the mean effluent salinity anomaly). The stable (unstable) salinity stratification in the deep Pacific (Atlantic) implies $R_\rho < 0$ ($R_\rho > 0$). Even though *McDougall* (1990) assumes the vertical gradients of background potential temperature and salinity to be constant, this is not used in his derivation of expression (6.1) — it is sufficient to assume that R_ρ is constant, i.e. that the background T/S relationship is linear. (*Lavelle et al.* (1998) arrive at the same conclusion using a different derivation.) Typical values for the stability ratio are $R_\rho = -2$ in the Pacific and $R_\rho = 2$ in the Atlantic (using the background stratifications of *Speer and Rona* (1989), as well as $\alpha = 1.47 \times 10^{-4}\,^\circ\mathrm{C}^{-1}$ and $\beta = 7.53 \times 10^{-4}\,\mathrm{psu}^{-1}$ at 4°C, 2000 dbar and 35 psu, taken from *Gill* (1982)).

Expression (6.1) indicates that hydrothermal equilibrium plumes may be cold/fresh or warm/salty independent of the sign of R_ρ. Fig. 6.1 shows the possible hydrographic-anomaly regimes in R_ρ/R_ρ^i space. In the hydrothermal context the source temperature anomalies are positive by definition, implying that the sign of R_ρ^i is determined by the source salinity anomalies (salinity excesses implying $R_\rho^i > 0$, with small values corresponding to large anomalies); the plumes rising from sources with zero salinity anomalies investigated by *Speer*

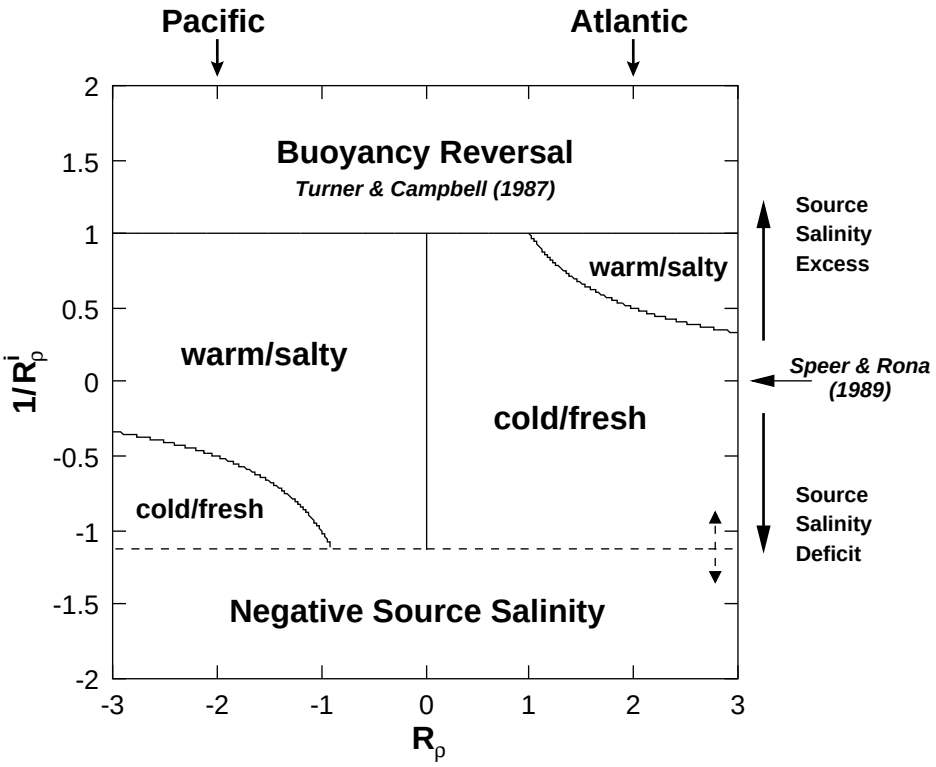

Fig. 6.1: Isopycnal hydrographic-anomaly regimes of hydrothermal equilibrium plumes; hydrographic background properties are characterized by the stability ratio R_ρ; effluent property anomalies are characterized by the density-anomaly ratio R_ρ^i; the parameters are not limited to the ranges shown.

and Rona (1989) are represented by $R_\rho^i \to \pm\infty$.

The regime labeled "Negative Source Salinity" covers the unphysical parameter range where the salinity deficit of the source fluid is greater than the background salinity S_b, i.e. $-\alpha\overline{\Delta\theta_i}/(\beta S_b) < R_\rho^i \leq 0$. The regime labeled "Buoyancy Reversal" ($0 \leq R_\rho^i \leq 1$) is not covered by the plume model because in this parameter range the linear equation of state implies negative (or neutral) buoyancy at the source. The thermal expansion coefficient α of the real equation of state is significantly increased at the high temperatures typically observed in hydrothermal sources *(Bischoff and Rosenbauer,* 1985) so that the effluents can initially be buoyant and reverse their buoyancy on mixing with background sea water *(Turner and Campbell,* 1987).

The areas labeled "cold/fresh" and "warm/salty" cover the hydrographic-anomaly regimes of hydrothermal equilibrium plumes. The curves dividing the positive and negative R_ρ half spaces into cold/fresh and warm/salty regimes indicate $R_\rho = R_\rho^i$ where the hydrographic

anomalies vanish. (The sign of the equilibrium-plume hydrographic anomalies is determined by the location of the source-fluid density-anomaly ratio R_ρ^i in relation to the linear bisection of the T/S space defined by the stability ratio of the background water column (R_ρ), because the T/S properties of the buoyant plume cannot cross the background properties as long as the linear equation of state applies; see *McDougall* (1990) for details.) In addition to the "classical" Atlantic cold/fresh and the Pacific warm/salty cases there are also Atlantic warm/salty ($R_\rho > R_\rho^i > 1$) and Pacific cold/fresh ($R_\rho < R_\rho^i \leq -\alpha\overline{\Delta\theta_i}/(\beta S_b)$ regimes. While these have not been observed in the context of hydrothermal plumes the effluent properties listed by *Von Damm* (1995) suggest that they may be possible. (Cold/fresh anomalies have long been known to result from "fresh" sewage input into the ocean, independent of the sign of R_ρ; e.g. *Fischer* (1971).)

6.3 Relationship Between Isopycnal and Isohaline Anomalies

From a hydrographic perspective, hydrothermal equilibrium plumes are neutrally buoyant intrusions with characteristic isopycnal temperature and salinity anomalies $\Delta_\rho T$ and $\Delta_\rho S$. Neutral buoyancy requires the temperature anomalies to be compensated by corresponding salinity anomalies, satisfying

$$\alpha\Delta_\rho T = \beta\Delta_\rho S, \tag{6.2}$$

where $\alpha = -\frac{1}{\rho}\frac{\partial\rho}{\partial T}\Big|_{S,p}$ and $\beta = \frac{1}{\rho}\frac{\partial\rho}{\partial S}\Big|_{T,p}$. Therefore, the hydrographic signatures of isopycnal intrusions can be characterized by a single variable (the "q" of *Stommel* (1962)) usually called *spice* or *spiciness (Munk,* 1981). In the following the isopycnal temperature anomaly of a water parcel will be used to characterize its spiciness.

Calculating geothermal isopycnal anomalies as deviations from linear background T/ρ trends *(Lupton et al.,* 1985) implies that the deviations are caused solely by geothermal processes. To evaluate this assumption it is useful to investigate the relationship between the T/ρ and the T/S spaces. The typical rise height of hydrothermal plumes (ignoring large event plumes) is a few hundred meters. The small gradients of temperature and salinity characteristic of the water column in the vicinity of deep hydrothermal vent fields indicate that the hydrographic contrasts outside the buoyant plumes are small. Therefore, the linear equation of state expanded about the reference properties S_0, T_0, p_0 is a valid approximation,

i.e.

$$\rho(S,T) = \rho_0 \left(1 - \alpha_0(T - T_0) + \beta_0(S - S_0)\right), \tag{6.3}$$

with $\rho_0 = \rho|_{S_0,T_0,p_0}$, $\alpha_0 = \alpha|_{S_0,p_0}$, and $\beta_0 = \beta|_{T_0,p_0}$. The gradient of density with respect to temperature is

$$\frac{\partial \rho}{\partial T} = \rho_0 \left(\beta_0 \frac{\partial S}{\partial T} - \alpha_0\right), \tag{6.4}$$

i.e. the relationship between the T/S and the T/ρ spaces is linear, which implies the equivalence of T/S linearity ($\partial S/\partial T = \text{const.}$) and T/ρ linearity ($\partial \rho/\partial T = \text{const.}$).

In addition to geothermal heating other processes, such as lateral intrusions and differential diffusion of heat and salt, can change linear T/S relationships, resulting in non-geothermal isopycnal hydrographic anomalies defined as deviations from linear background T/ρ relationships. (Lateral intrusions are common in the rift valley of the MAR, e.g. section 3.2.2.)

From expressions (6.2) and (6.3) it follows that the constant factor relating the isopycnal to the corresponding isohaline temperature anomalies ($\Delta_S T$) observed in regions of linear background T/S relationships (e.g. *Thomson et al.,* 1995) can be calculated from the background stratification of temperature and salinity. The constant of proportionality is

$$\frac{\Delta_S T}{\Delta_\rho T} = 1 - \frac{\alpha_0}{\beta_0}\frac{\partial T}{\partial S} = 1 - R_\rho. \tag{6.5}$$

Using the T/S slopes given by *Thomson et al.* (1995) together with the corresponding values for α_0 and β_0 (evaluated at the reference pressure of potential temperature and density) the constant of proportionality becomes 0.52 which compares well with the value of 0.54 ± 0.04 calculated from their table 2, confirming that the linear equation of state is a valid approximation in deep-sea hydrothermal environments.

Combining expressions (6.1) and (6.5) reveals that the isohaline temperature anomalies associated with hydrothermal equilibrium plumes rising from sources without salinity anomalies are equal to the source temperature anomalies scaled by dilution. (The expressions can be combined because they are both based on the same two assumptions, namely neutral density and linear background T/S relationships; $\overline{\Delta\theta_e}$ of expression (6.1) corresponds to $\Delta_\rho T$ of expression (6.5).) Using spatially integrated isohaline temperature anomalies to estimate the geothermal heat content of the water column (e.g. *Thomson et al.,* 1995) is therefore equivalent to using isopycnal anomalies corrected with the expression of *McDougall* (1990) and assuming zero source salinity anomalies.

Expression (6.5) implies that entrainment into buoyant plumes is not required for the cold/fresh isopycnal anomalies observed in regions of unstable background salinity stratification. If the bottom water is conductively heated (and assuming that the heating is gradual enough so that no convective instabilities develop) its density is reduced without an associated change in salinity. Compared to background water of the same density the geothermally modified water is fresh and expression (6.2) implies that it is cold. Entrainment and vertical transport *are* required for isobaric cold/fresh anomalies, however.

6.4 Plume-Bracketing Method

In the Pacific ocean geothermal temperature anomalies are often calculated as deviations from background T/ρ or T/S trends. A number of different methods are used to estimate the background trends, effectively resulting in different anomaly definitions. *Lupton et al.* (1980), for example, use a visual method based on the observation of abrupt changes in the T/S trend at the top and bottom of a layer characterized by hydrothermal helium anomalies; *Lupton et al.* (1985) use a similar method in T/ρ space with the additional assumption of a linear background relationship. In other studies the backgrounds are defined by extrapolating the hydrographic trends observed above bottom layers characterized by hydrothermal particle and chemical anomalies to the sea floor (e.g. *Baker et al.,* 1990; *Baker and Lupton,* 1990). This method will be called the *extrapolation method.* Following *Thomson et al.* (1995), the geothermally modified bottom layer will be called the *geothermal boundary layer (GBL).*

There are two potential problems associated with hydrographic anomalies defined as deviations from T/ρ or T/S trends extrapolated into the GBL, namely the lack of separation of the hydrographic effects caused by different geothermal processes (e.g. *Thomson et al.,* 1992) and the anomalies caused by non-geothermal hydrographic variability (e.g. *Baker and Hammond,* 1992). To solve these problems additional information is required to separate the geothermal signals from "hydrographic noise". Light-scattering and transmissometry anomalies are often used in conjunction with hydrographic measurements to detect and map hydrothermal plumes and to limit the volume integrals from which the geothermal heat content of the water column is calculated (e.g. *Baker and Hammond,* 1992; *Helfrich et al.,* 1998).

Fig. 6.2 shows a sketch illustrating a new anomaly definition and method (related to that of *Lupton et al.* (1985)) which incorporates nephelometry or transmissometry data to

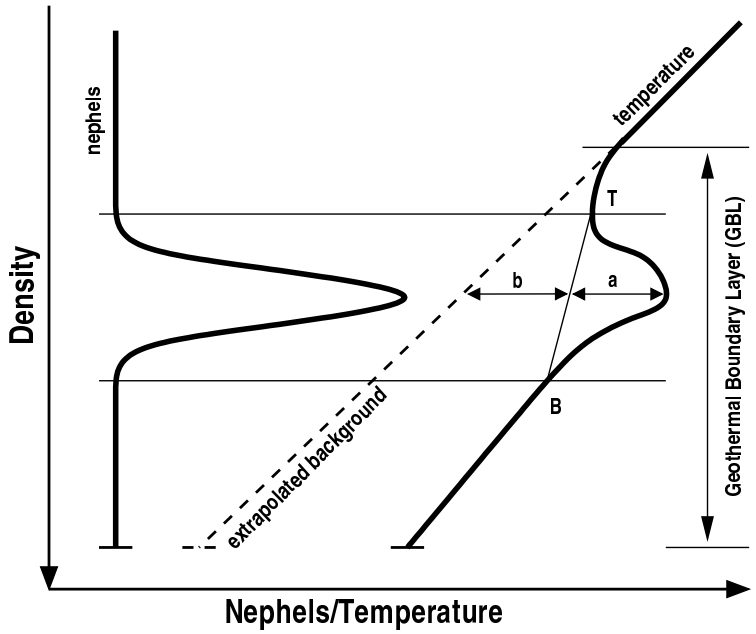

Fig. 6.2: Illustration of two methods for estimating isopycnal hydrographic anomalies; thick lines represent nephelometry and temperature profiles in density space. The straight line connecting the temperature profile between the top (T) and the bottom (B) of the particle peak shows the linear approximation to the background T/ρ relationship relative to which the temperature (spice) anomalies of the plume-bracketing method (a) are defined. The dashed line shows the extrapolation of the T/ρ trend of the water column overlying the plume into the GBL, defining the temperature anomalies of the extrapolation method (a+b).

constrain the hydrographic anomalies associated with the hydrothermal particle plume. The background T/ρ relationship within the particle layer of a single profile is approximated by linearly interpolating the measured T/ρ properties between the top (T) and the bottom (B) of the particle layer. Above T and below B, the anomalies are set to zero. This method will be called the *plume-bracketing method.* For comparison, the extrapolation method is shown as well.

To test the plume-bracketing method it was applied to the CTD data set from the 1997 survey (section 2.1). Because of the small vertical separation between the observed interleaving structures (section 3.2.2) and the particle plume the extrapolation method cannot be used. Fig. 6.3 illustrates the plume-bracketing method applied to the two profiles with the largest (1.3 V) and the smallest (0.4 V) nephelometry peak values where the corresponding thermal anomalies are distinguishable from temperature scatter (see below). The deviations

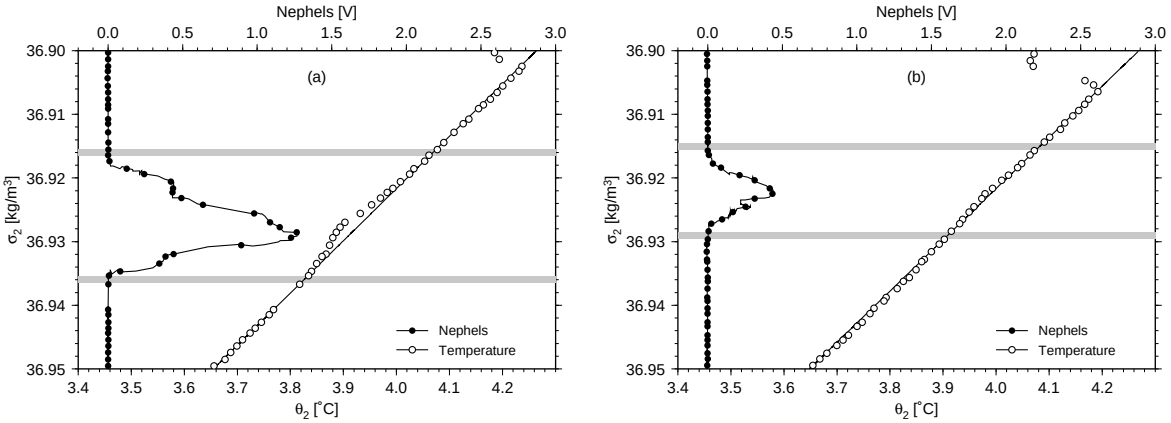

Fig. 6.3: Application of the plume-bracketing method to two profiles of the 1997 CTD data set.

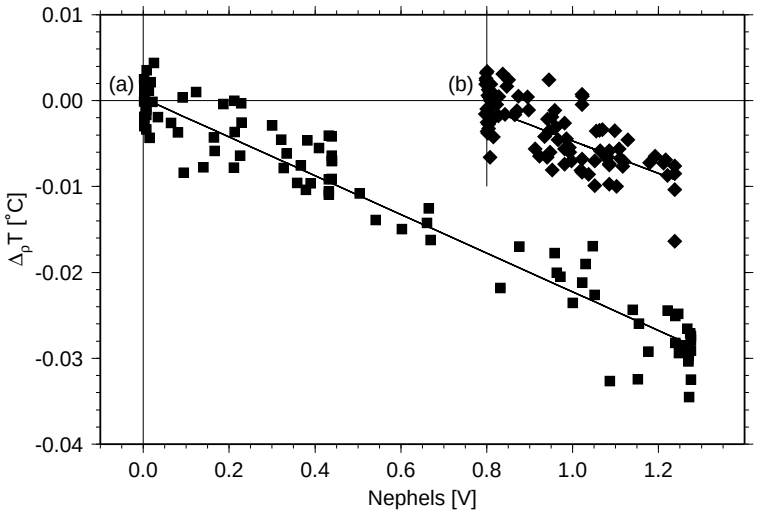

Fig. 6.4: Spice vs. nephel scatter plots and linear regressions derived from the particle peaks of the profiles shown in Fig. 6.3; the origin of profile (b) is horizontally offset by 0.8 V; correlation coefficients are $r = -0.97$ and $r = -0.69$, regression slopes $-2.3 \times 10^{-2}\,^{\circ}\mathrm{C}\cdot\mathrm{V}^{-1}$ and $-1.9 \times 10^{-2}\,^{\circ}\mathrm{C}\cdot\mathrm{V}^{-1}$, and RMS errors $2.9 \times 10^{-3}\,^{\circ}\mathrm{C}$ and $2.7 \times 10^{-3}\,^{\circ}\mathrm{C}$, respectively.

from the near-linear T/ρ trends at the top of the temperature profiles are signatures of the interleaving structures. The bands bracketing the nephelometry peaks were positioned visually and span 10^{-3} σ_2 units each. Fig. 6.4 shows the scatter plots and linear regressions of the resulting spice vs. nephel anomalies. The respective correlation coefficients are $r = -0.97$ and $r = -0.69$, and both RMS errors are $< 3 \times 10^{-3}\,^{\circ}\mathrm{C}$.

Out of the 31 *FLAME* CTD profiles containing particle-plume signatures, 16 do not extend below the plume (they are *truncated),* implying that the plume-bracketing method

cannot be applied. It was found that the method failed to establish correlations in 4 of the remaining profiles, all of which have nephelometry peak values $<0.3\,\mathrm{V}$. (Using a regression slope estimate of $-2\times10^{-2}\,^{\circ}\mathrm{C}\cdot\mathrm{V}^{-1}$, this corresponds to peak temperature anomalies of less than twice the RMS error.) The weighted mean ($\pm1\sigma$) correlation coefficient of the remaining 11 profiles is $r=-0.84(\pm0.03)$.

6.5 Bilinear Method

The results from the plume-bracketing method applied to the 1997 CTD data indicate that the isopycnal hydrographic anomalies associated with the *Rainbow* particle plume are linearly correlated with the corresponding nephelometry anomalies within individual profiles. Keeping the assumption of a linear background T/ρ relationship, the temperature profile within a particle peak can therefore be written as

$$T(z)=A+B\rho(z)+C\Delta n(z), \tag{6.6}$$

where the nephelometry anomalies are denoted by Δn. Expression (6.6) defines a bilinear model which can be fitted to simultaneous profiles of temperature, density, and nephelometry anomalies. The regression coefficients A and B define the background T/ρ relationship within the particle layer (similar to the linear interpolation between T and B of the plume-bracketing method), and the isopycnal temperature anomalies are given by

$$\Delta_\rho T(z)=C\Delta n(z)=T(z)-(A+B\rho(z)). \tag{6.7}$$

To fit expression (6.6) to a particle peak, the χ^2 merit function

$$\chi^2=\sum_{k=1}^{N}\left(\frac{T_k-(A+B\rho_k+C\Delta n_k)}{\sigma}\right)^2 \tag{6.8}$$

(where T_k, ρ_k and Δn_k are the individual temperature, density, and nephelometry anomaly measurements) is minimized using a generalized least-squares algorithm (e.g. *Press et al.*, 1993). This method will be called the *bilinear method*.

Minimizing expression (6.8) yields the same regression coefficients regardless of the (assumed constant) value of σ which quantifies the combined measurement uncertainties (expected RMS error). If the residuals are normally distributed σ is the corresponding standard deviation which can be used to calculate confidence intervals for the regression coefficients.

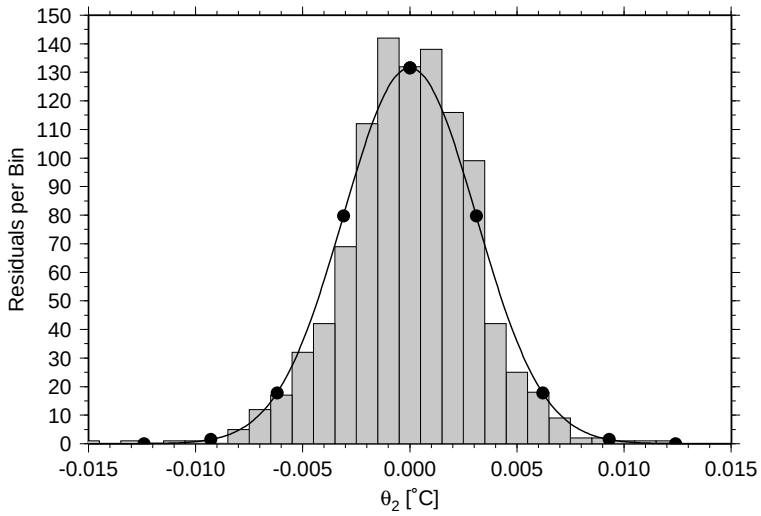

Fig. 6.5: Distribution of the residuals resulting from the bilinear method applied to the *FLAME* CTD data set; histogram bin size is 10^{-3}°C (twice the temperature sensor resolution); the curve shows the corresponding normal distribution with bullets plotted at multiple standard deviations ($\sigma = 3.1 \times 10^{-3}$ °C) from the mean.

To determine the distribution of the residuals, a frequency histogram was derived from the *FLAME* CTD data set (Fig. 6.5). The distribution is approximately normal with standard deviation $\sigma = 3.1 \times 10^{-3}$ °C. (The residuals of the plume-bracketing method are similarly distributed with standard deviation $\sigma = 3.5 \times 10^{-3}$ °C.)

In profiles where the spice and the nephelometry anomalies are linearly correlated and where the background T/ρ relationships within the particle layers are linear the bilinear and the plume-bracketing methods are equivalent. This is confirmed in the case of the 11 *FLAME* CTD profiles to which the plume-bracketing method had been applied (section 6.4). The weighted mean ($\pm 1\sigma$) spice vs. nephel correlation coefficient of the bilinear method is $r = -0.87(\pm 0.03)$ and the respective 68.3% confidence intervals of the individual regression-slope estimates derived with the two methods overlap.

Strictly speaking the two new methods are only equivalent if they are applied to the same subset of a given profile. Because the background hydrographic properties of the bilinear method are calculated from the entire plume peak the brackets do not have a "thickness" and can be selected in depth or in pressure space. The results from the 1997 CTD data set (see section 6.6 below) indicate that the background T/S slope was slightly different above and below the hydrothermal plume, indicating that the particle peaks should be tightly bracketed.

To avoid inconsistent application of the method the depth of the particle peak limits were rounded to the next 25 m outside the peaks.

In contrast to the plume-bracketing method, the bilinear method can be applied to truncated profiles (section 6.4). Out of the 16 truncated *FLAME* CTD profiles only 2 have nephelometry peak values >0.3 V (both are <0.7 V). The resulting weighted mean spice vs. nephel correlation coefficient is $r = -0.75$ and the respective slopes and RMS errors are consistent with the remainder of the data set (see Fig. 6.7).

Expression (6.6) cannot be fitted unambiguously to profiles characterized by (nearly) linear relationships between $\rho(z)$ and $\Delta n(z)$ because the data do not constrain both regression coefficients B and C independently in this case. In practice this can happen when the bilinear method is applied to the upper half of a particle peak, i.e. in truncated profiles which do not extend significantly below the particle maxima. To assess the independence of the estimates for B and C, the cross-correlation coefficient r_{BC} can be inspected. In the case of the 1997 CTD profiles $-0.4 < r_{BC} < 0.1$, while $r_{BC} < -0.8$ when the bilinear method is applied to the same profiles artificially truncated at the nephelometry maxima.

Minimizing expression (6.8) does not constrain the temperature anomalies to vanish at the top and at the bottom of the particle plume. Non-zero values can result if one of the linearity assumptions is violated or if the nephelometry anomaly profile is offset by a constant amount, i.e. non-zero values indicate failure of the bilinear method. This is used in section 6.7 to determine the appropriate nephelometry origin of a profile where the choice is ambiguous.

6.6 Spice Anomalies of the *Rainbow* Hydrothermal Plume

6.6.1 1997 Survey *(FLAME)*

Fig. 6.6 shows a selection of the 1997 CTD nephelometry profiles, scaled by the respective spice vs. nephel regression slopes and overlaid on the corresponding spice profiles; (a) and (b) are the ones shown in Fig. 6.3 while (c) and (d) were selected for their vertically structured particle layers. The agreement between the plume signatures of the corresponding profiles is striking and indicates that the temperature and particle anomalies are signatures of the same physical processes.

By definition the temperature anomalies outside the particle peaks are zero (section 6.4). The extended profiles shown in Fig. 6.6 allow some interesting observations, however. Except

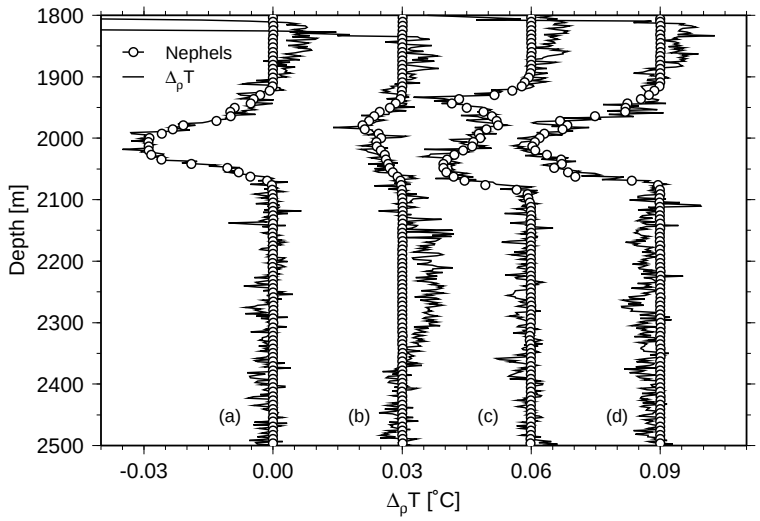

Fig. 6.6: Overlays of scaled nephelometry and spice profiles of the *FLAME* CTD data set; successive profiles are horizontally offset by 0.03°C; profiles (a) and (b) are the ones shown in Fig. 6.3.

in profile (b) between 2130 m and 2350 m, the anomalies below the particle peaks remain close to zero, indicating that the new methods estimate background T/ρ properties consistent with the water column below the hydrothermal equilibrium plume. Above the particle peaks the slopes of the T/ρ relationships are different, resulting in the positive anomalies increasing upwards until intersecting the interleaving structures which give rise to the large negative spice anomalies at the top of the profiles. The temperature anomalies are similarly biased towards the hydrography *below* the particle peaks in all profiles of the 1997 CTD data set, consistent with the view that the equilibrium plume is a mixture of hydrothermal effluents and fluid entrained during plume rise. Profile (b) illustrates the effect of a non-linear T/ρ relationship below the particle peak (see also Fig. 6.3) — the positive anomalies between 2130 m and 2350 m are of the same order of magnitude as the negative anomalies associated with the particle layer, indicating that it would not have been possible to establish the relevant background from hydrographic data alone.

In the left panel of Fig. 6.7, labeled "(CTD)", the spice vs. nephel regression slopes from the *FLAME* CTD data set are plotted against the corresponding horizontal distances from the vent field. (In two of the profiles it was possible to calculate independent values from separate particle peaks, resulting in the total of 15 estimates from 13 profiles.)

The *BRIDGET* hydrographic profiles are characterized by comparatively large scatter in

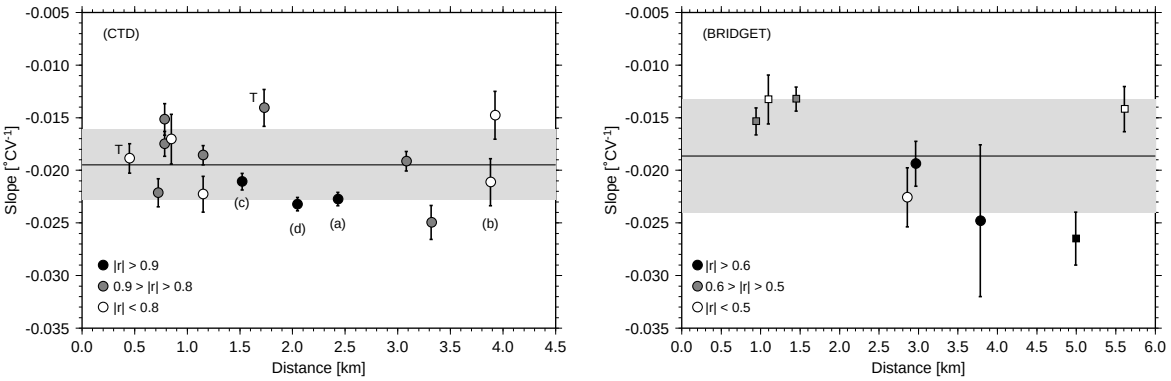

Fig. 6.7: Spice vs. nephel regression slopes (bilinear method) of the 1997 CTD and *BRIDGET* data sets plotted against the corresponding horizontal distances from the *Rainbow* vent field; error bars show the 68.3% confidence intervals; shading of the symbols (different for the two data sets) is determined by the correlation coefficients; the horizontal bands indicate the mean ($\pm 1\sigma$) slopes. Profiles (a)—(d) of the CTD data set are those shown in Fig. 6.6; the two truncated CTD profiles (section 6.5) are annotated with a T. The different symbols (squares and circles) of the *BRIDGET* data set indicate profiles derived from the two separate but identical CTD instruments (section 2.1).

the conductivity measurements, contaminating the density data. Out of the 24 *BRIDGET* profiles with nephelometry peak values > 0.3 V the bilinear method failed in 16 cases, either because no correlation could be established (the limiting criterion $|r| \geq 0.4$ was chosen by inspection of the individual spice vs. nephel scatter plots) or because the cross-correlation coefficients r_{BC} fell outside the range $[-0.8...0.2]$ (section 6.5). In the right panel of Fig. 6.7, labeled "(BRIDGET)", the remaining spice vs. nephel regression slopes are plotted against the corresponding horizontal distances from the vent field.

Other studies (e.g. *Baker et al.*, 1995) indicate that correlations between hydrothermal particle and temperature anomalies can vary with plume age because of non-conservative particle behavior. No trends are apparent in the *FLAME* data, possibly because of the short distances considered here. Using the mean along-valley advection velocity at plume depth ($0.1\,\mathrm{m\cdot s^{-1}}$, from Fig. 3.10) the 1997 profiles have nominal plume ages < 17 h. To a first approximation, the near-source spice vs. nephel regression slopes can therefore be considered constant with mean values ($\pm 1\sigma$) of $-1.9(\pm 0.3) \times 10^{-2}\,^{\circ}\mathrm{C\cdot V^{-1}}$ (CTD) and $-1.9(\pm 0.5) \times 10^{-2}\,^{\circ}\mathrm{C\cdot V^{-1}}$ *(BRIDGET)*. Fig. 6.7 indicates that the similarity of the two estimates is somewhat fortuitous, but it is consistent with the similar response characteristics of the different nephelometers used on the two platforms (section 2.1).

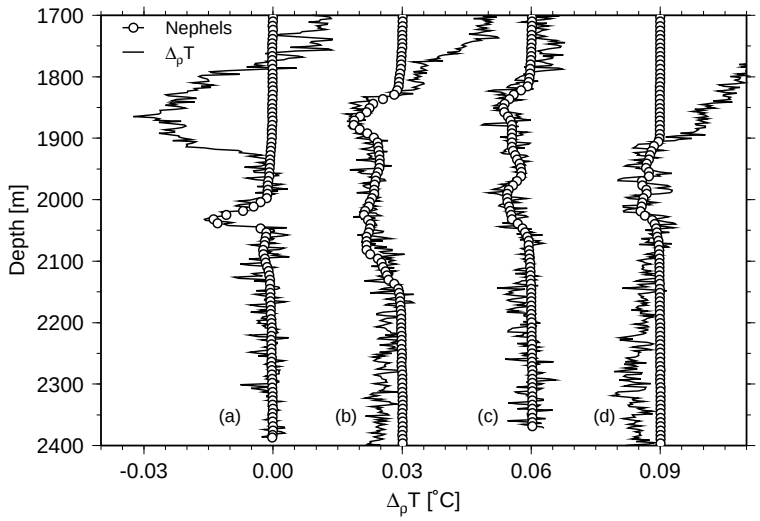

Fig. 6.8: Overlays of scaled nephelometry and spice profiles of the *FLAME-2* data set; successive profiles are horizontally offset by 0.03°C; profiles (a), (b) and (d) correspond to profiles (a), (d) and (e) of Fig. 5.7.

6.6.2 1998 Survey *(FLAME-2)*

The bilinear method was applied to the data set from the 1998 survey as well. Because different nephelometers were used during the two cruises the magnitudes of the light-scattering peaks cannot be compared directly (c.f. chapter 5). Based on initial observations, 4 out of the 8 profiles with plume signals (thick bars in Fig. 5.6) have detectable temperature anomalies associated with the nephelometry peaks, defining the lower limit of detectability in this data set as a nephelometer response of 0.2 V. The corresponding spice and scaled nephelometry anomalies of the 4 profiles are shown in Fig. 6.8. To allow direct comparison with Fig. 6.6 the same temperature scale is used. The maximal temperature anomalies of the 1998 data set are of order -0.015°C, i.e. approximately half of those observed in 1997. There is again a general agreement between the vertical structures observed in the light-scattering and in the corresponding spice profiles. As is the case in the 1997 data sets, the bilinear method is biased towards the hydrography below the particle plume.

Using the same criterion applied to the 1997 data for consistency (i.e. spice vs. nephel $|r| \geq 0.4$) the bilinear method fails in the case of profile (d), most likely because of the weakness of the plume signatures and because the particle layer coincides with a change in the background T/S slope. The remaining profiles yield spice vs. nephel regression slopes, correlation coefficients and RMS errors of $-2.8(\pm 0.3) \times 10^{-2}\,°\mathrm{C}\cdot\mathrm{V}^{-1}$, -0.83 and $2.7 \times 10^{-3}\,°\mathrm{C}$ (a);

$-2.8(\pm 0.2) \times 10^{-2}\,^{\circ}\mathrm{C}\cdot\mathrm{V}^{-1}$, -0.73 and $2.7 \times 10^{-3}\,^{\circ}\mathrm{C}$ (b); and $-2.7(\pm 0.4) \times 10^{-2}\,^{\circ}\mathrm{C}\cdot\mathrm{V}^{-1}$, -0.59 and $2.6 \times 10^{-3}\,^{\circ}\mathrm{C}$ (c), respectively. As is the case in the 1997 data sets, the regressions are mutually consistent. The near-equality of the RMS errors of the CTD data sets from the two surveys is consistent with the similarity of the two instruments (sections 2.1 and 2.2).

Expression (6.1) indicates that differences in the equilibrium-plume temperature anomalies can be caused by changes in the background hydrography (R_ρ) or in the hydrothermal effluent properties (R_ρ^i). The stability ratio of the water column R_ρ is calculated from the near-source CTD profiles in the depth range of plume rise (1900–2300 m in 1997 and 1800–2300 m in 1998), with $\alpha = 1.47 \times 10^{-4}\,^{\circ}\mathrm{C}^{-1}$ and $\beta = 7.53 \times 10^{-4}\,\mathrm{psu}^{-1}$ at 4°C, 35 psu and 2000 dbar taken from *Gill* (1982). The respective values are $R_\rho = 2.36(\pm 0.11)$ for 1997 and $R_\rho = 2.24(\pm 0.04)$ for 1998, i.e. the difference is less than 5%, indicating that changes in the magnitude of the hydrographic anomalies would primarily be caused by changes in the hydrothermal source fluid. However, the small number of profiles taken during the 1998 survey does not permit a mean plume to be derived so that no change in the effluent properties can be inferred from our data.

6.7 Spice Anomalies of Pacific Hydrothermal Plumes

Fig. 6.2 indicates that the temperature anomalies calculated with the new methods are related to the ones derived using the extrapolation method. (In the following, "bilinear" and "extrapolated" will be used to distinguish results from the two methods.) To compare the different anomaly definitions, the bilinear method was applied to three profiles (generously provided by Ed Baker) from Pacific hydrothermal sites (Fig. 6.9) where the "extrapolated" anomalies were calculated as deviations from quadratic (a and c) and linear (b) trends (E.T. Baker, *pers. comm.)*. Interpretation of individual profiles without knowledge of their associated contexts is tenuous, but the Pacific profiles have some features in common with each other (and with the *Rainbow* data) which are worth pointing out.

The particle anomalies of profile (a) from the East-Pacific Rise are restricted to a well defined peak, similar to the *Rainbow* data. The "bilinear" temperature anomalies vanish at the top and at the bottom of the particle layer, and the profile shows the familiar bias towards the hydrographic properties below the plume. Correlation between the particle and the temperature anomalies within the shaded area is higher for the "bilinear" anomalies ($r =$

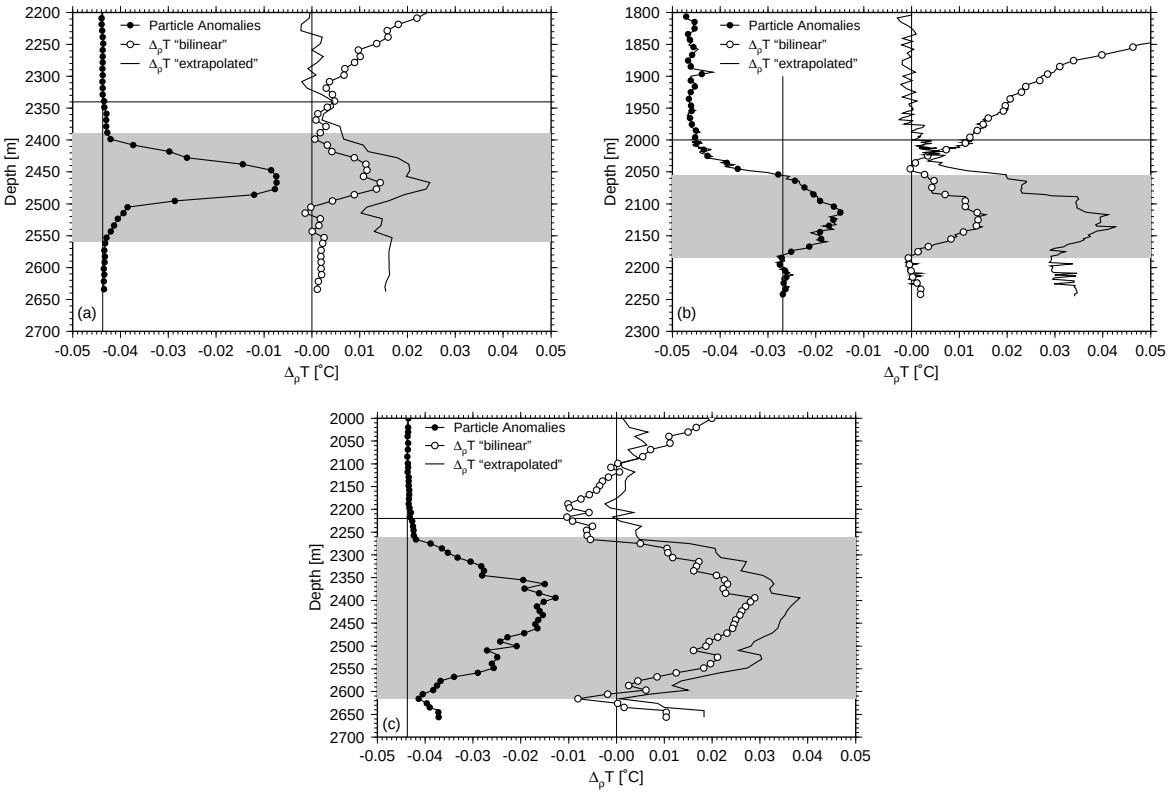

Fig. 6.9: Particle and temperature anomaly profiles of Pacific hydrothermal plumes; (a) & (c) from 17°S on the East-Pacific Rise, and (b) from the Juan de Fuca Ridge; the "extrapolated" anomalies were calculated as deviations from extrapolated T/ρ relationships of the water overlying the plumes; the "bilinear" profiles were derived from the particle peaks (shaded); horizontal lines show the upper limits of the GBLs; vertical lines indicate the origins of the temperature and the (arbitrarily scaled) particle anomaly axes; data courtesy of Ed Baker.

0.95, RMS error 1.6×10^{-3} °C) than for the "extrapolated" anomalies ($r = 0.85$, RMS error 2.7×10^{-3} °C). The vertically integrated "extrapolated" temperature anomalies of the GBL (i.e. below the horizontal line, determined by the depth where the "extrapolated" anomalies depart from zero) are 4.4 times larger than the corresponding integrated "bilinear" anomalies (noting that the latter are zero outside the particle plume by definition).

Profile (b) from the Juan de Fuca Ridge is characterized by a qualitatively similar "extrapolated" temperature anomaly profile, while the particle distribution is different from that of profile (a). Compared to the water column above the GBL, there are significant particle anomalies extending to the bottom of the cast. Below the main particle peak they remain approximately uniform, consistent with an elevated background particle concentration below the equilibrium plume. There are therefore two reasonable choices for the origin of the par-

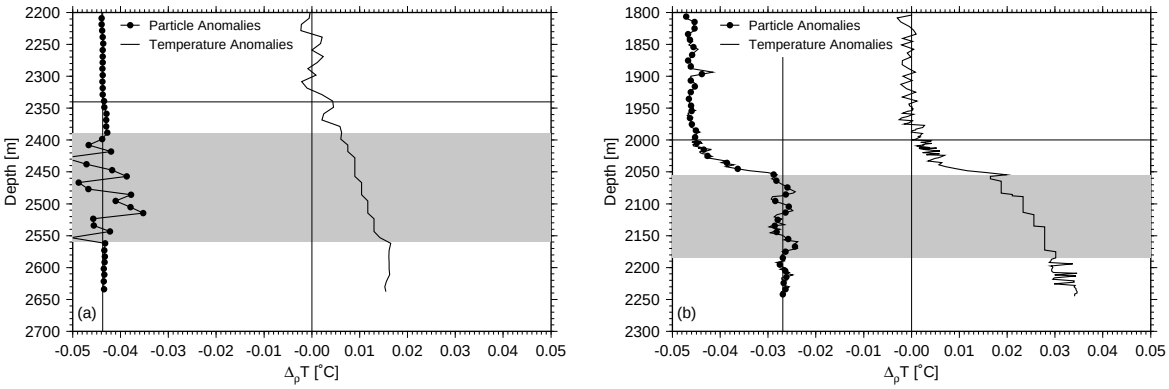

Fig. 6.10: Residual particle and temperature anomalies of Pacific profiles (a) and (b); the shaded regions and the horizontal and vertical lines are the same as in Fig. 6.9.

ticle anomalies, namely the level in the water column above the GBL and the level near the bottom of the profile. The "bilinear" temperature anomalies shown in Fig. 6.9 were derived by choosing the latter. Physically, this is motivated by considering the equilibrium plume to be a mixture of hydrothermal effluents and background fluid entrained during plume rise, consistent with the hydrographic bias of the new methods. (Applying the bilinear method to the same profile with the particle anomalies referenced to the water column above the GBL results in a temperature anomaly profile offset by 0.02°C but otherwise identical to the one shown.) Compared to the "extrapolated" anomalies, the "bilinear" ones reduce the RMS error of the temperature vs. particle anomaly correlation within the shaded area by more than 50% (from $4.5 \times 10^{-3}\,^{\circ}$C to $1.9 \times 10^{-3}\,^{\circ}$C) while the corresponding correlation coefficient increases from $r = 0.71$ to $r = 0.92$. The vertically integrated "extrapolated" temperature anomalies of the GBL are 6.1 times larger than the corresponding integrated "bilinear" anomalies.

In profile (c) from the East-Pacific Rise the particle plume occupies nearly the entire GBL. The "bilinear" temperature anomalies associated with the particle plume are virtually identical to the "extrapolated" anomalies offset by -0.01°C. Statistically, the temperature vs. particle anomaly correlations are indistinguishable ("extrapolated": $r = 0.95$, RMS error $2.8 \times 10^{-3}\,^{\circ}$C; "bilinear": $r = 0.95$, RMS error $2.7 \times 10^{-3}\,^{\circ}$C). Without additional information it is not clear which of the two anomaly definitions is more appropriate in this case.

Combining the results from the bilinear and the extrapolation methods allows the plume particle and the corresponding temperature anomalies to be removed from the respective profiles. The residual temperature anomalies shown in Fig. 6.10 were derived by subtracting

the "bilinear" from the "extrapolated" profiles, while the corresponding residual particle anomalies $\Delta_r n(z)$ were calculated using

$$\Delta_r n(z) = \Delta n(z) - \Delta_\rho T(z)/C. \tag{6.9}$$

The residual particle anomalies within the shaded plume layers fluctuate around zero, as expected from expression (6.6). The large scatter in profile (a) is caused by the small magnitude of the temperature vs. particle-anomaly regression slope C which is approximately 25 times smaller than the corresponding value of profile (b). The residual temperature anomalies increase towards the sea bed, similar to geothermally modified profiles without hydrothermal particle plume signatures (e.g. *Thomson et al.*, 1995).

6.8 Discussion

The two new methods developed to calculate hydrographic anomalies associated with hydrothermal particle plumes correspond to two new anomaly definitions which are equivalent if the particle and spice anomalies are linearly correlated and if the background T/S relationship in the particle plume is linear, as is the case in the data from the two quasi-synoptic surveys. The plume-bracketing method is equivalent to the method of *Lupton et al.* (1985) if the T/S background outside the particle plume is linear and both are equivalent to the extrapolation method if the T/S background above the plume is linear, apparently implying that the extrapolation method is equivalent to the method of *Lupton et al.* (1985). Because extrapolation requires much stricter adherence to linearity than interpolation, methods based on the latter are preferable. If the particles within a given peak of a single profile behave non-conservatively (implying either reaction timescales which are shorter than the sampling timescale or separate unmixed constituents making up the peak) the bilinear method cannot be used. If, on the other hand, there are background anomaly gradients coinciding with the particle peak, as was argued for Pacific profile (b), the plume-bracketing method cannot be used.

The near-source particle distribution of the *Rainbow* hydrothermal plume closely mirrors the corresponding hydrographic anomalies calculated with the new methods. The linear correlations between the light-scattering and the spice anomalies indicate that the nephelometry anomalies of individual profiles behave conservatively. Similar correlations were obtained by applying the bilinear method to three Pacific profiles while the corresponding temperature

anomalies derived with the extrapolation method result in significantly lower correlations in two of the three profiles. The linear relationships resulting from the application of the new methods (and the corresponding new anomaly definitions) imply that both temperature and particle anomalies reflect the amount of dilution of the hydrothermal effluents with background fluid entrained during plume rise. Mixing as the dominant physical process governing the distribution of both types of anomalies is consistent with the bias of the new methods towards the background hydrographic properties and particle loads below the equilibrium plumes, and with the Gaussian shape of the density-averaged nephelometry profiles of the 1997 *BRIDGET* data set (section 5.2).

All three data sets of the *Rainbow* hydrothermal plume yield mutually consistent (within each data set) spice vs. nephel relationships, indicating that the conservative behavior of the hydrothermal particles is not limited to the short time scales associated with individual profiles. Linear correlations between particle, chemical and hydrographic anomalies of hydrothermal plumes have been observed at other sites, most notably in event plumes, while the corresponding relationships in *steady-state* (i.e. non-event) plumes are usually reported to be more variable (e.g. *Baker and Massoth,* 1987; *Chin et al.,* 1994). The results shown here indicate that this variability may be caused partially by uncertainties in the estimates of the background properties relative to which the hydrographic anomalies are defined. This has important consequences for the interpretation of anomaly ratios. The observed temporal and spatial variability of "extrapolated" hydrographic vs. particle (e.g. *Baker,* 1994) and vs. chemical anomalies (e.g. *Lupton et al.,* 1999) may be caused partially by background variability, for example.

Comparing the results from the different methods applied to the Pacific profiles indicates that heat anomalies derived with the extrapolation method can be dominated by contributions from processes which are not associated with the equilibrium particle plumes rising from high-temperature hydrothermal vent fields. This may be one of the reasons for the large difference between heat flux estimates calculated from "extrapolated" temperature anomalies and those derived from measurements at black-smoker vent orifices and in buoyant plumes on the Juan de Fuca Ridge, discussed by *Ginster et al.* (1994). Because of the similarity of the residual temperature anomaly profiles with GBL observations without associated particle plume signatures (e.g. *Thomson et al.,* 1995) and because of the lack of alternative process candidates which could cause the observed isopycnal warming, it appears reasonable

to assume that the residual profiles are signatures of geothermal heating. Not much can be concluded from only two profiles but it is noteworthy that the residual temperature anomalies extend above the equilibrium particle plumes in both cases. Therefore, it appears unlikely that they are caused entirely by low-temperature (or "diffuse") hydrothermal circulation and heat conduction in the nearby vent fields.

Chapter 7

Convective Heat Flux from the *Rainbow* Hydrothermal Vent Field

7.1 Introduction

In this chapter heat flux estimates for the *Rainbow* hydrothermal vent field are derived. In section 7.2 estimates are calculated from the rise heights of the particle plumes observed during the two quasi-synoptic surveys (chapter 5). It is shown that the point-source assumption required for this approach is not valid at the *Rainbow* site, indicating that the estimates are not representative of the total high-temperature fluxes. In section 7.3 a better estimate for the 1997 heat flux is derived from the advective flux of the temperature anomalies in the equilibrium plume. The chapter concludes with a discussion in section 7.4.

7.2 Height-Of-Rise Method

A simple method for estimating heat fluxes from hydrothermal plumes is based on source buoyancy flux estimates derived from height-of-rise observations and more or less elaborate models of the buoyant plumes. Even the most advanced of current numerical models cannot resolve plumes from individual sources within a vent field and must rely on the assumption of a single point (or line) source (i.e. the length scale associated with the source area is assumed to be much smaller than the plume rise height) *(Lavelle,* 1997). If this assumption is violated the buoyancy flux estimated from the rise height of the model plume can significantly underestimate the true buoyancy flux because the effects of plume interaction at some height

above the sources are ignored. The individual vent chimneys of the *Rainbow* hydrothermal field (located near the 2300 m isobath) are distributed over an area of 100 m×250 m *(Fouquet et al.,* 1998), indicating that the extent of the integrated plume source is of the same order as the mean rise height of 200 m observed during the 1997 survey (section 5.2).

To estimate the buoyancy flux required to propel a plume to the observed height-of-rise the buoyant time-averaged plume is modeled by solving conservation equations for mass, heat, salt and momentum, i.e.

$$\frac{\partial}{\partial z}(XW) = \Lambda X^{1/2} W \tag{7.1}$$

$$\frac{\partial}{\partial z}(TXW) = \Lambda T_b X^{1/2} W \tag{7.2}$$

$$\frac{\partial}{\partial z}(SXW) = \Lambda S_b X^{1/2} W \tag{7.3}$$

$$\rho_0 \frac{\partial}{\partial z}(XW^2) = g(\rho - \rho_b) X \tag{7.4}$$

(e.g. *Speer and Rona,* 1989), where X and W are the cross-sectional area and the vertical velocity of the plume, and T_b, S_b and ρ_b denote the hydrographic properties of the background water column. The effects of plume-generated turbulence are represented by an *entrainment assumption* which states that the amount of background fluid mixed into the plume is proportional to the vertical plume velocity *(Morton, Taylor, and Turner,* 1956). The entrainment coefficient $\Lambda = 0.415$ is taken from *Turner* (1986). A linear equation of state (with $\alpha = 1.47 \times 10^{-4}\,^{\circ}\mathrm{C}^{-1}$ and $\beta = 7.53 \times 10^{-4}\,\mathrm{psu}^{-1}$ at 4°C, 2000 dbar and 35 psu, taken from *Gill* (1982)) is used *(Turner and Campbell,* 1987). The initial conditions are taken from the observed effluent properties of the *Rainbow* vent field *(Fouquet et al.,* 1998) and by choosing source buoyancy fluxes — in effect combinations of representative source velocities (e.g. $0.4\,\mathrm{m \cdot s^{-1}}$; *Speer and Rona,* 1989) and areas — so that the maximum height reached by the model plume (where W becomes negative) matches the observed height-of-rise. The approach followed here is similar to that of *Rudnicki and Elderfield* (1992) but individual nephelometry peaks are not assumed to be superimposed plumes from separate sources (chapter 5).

Numerically solving equations (7.1)–(7.4), using the mean 1997 SW basin hydrography for T_b, S_b and ρ_b, results in a source buoyancy flux estimate of $0.1\,\mathrm{m^4 \cdot s^{-3}}$ corresponding to the observed maximum rise height of 400 m (section 5.2). This yields a heat-flux estimate of 0.3 GW (using the low-temperature specific heat $c_p = 4.2 \times 10^3\,\mathrm{J \cdot kg^{-1} \cdot K^{-1}}$; *Turner and Campbell,* 1987). The total rise time of the model plume is of order 1 h and the temperature anomaly at the level of neutral buoyancy is −0.05°C, an order of magnitude larger than

the peak temperature anomalies associated with the Gaussian near-field plume (section 7.3). (Based on unpublished data from a dye-release experiment the rise time of individual parcels of hydrothermal plume fluid can be much shorter (of order minutes) than the mean rise time predicted by bulk plume models; A. Schultz, *pers. comm.)*

Applying the height-of-rise method to the particle plume observations of the 1998 survey (maximum rise height 500 m; section 5.3) and using the corresponding hydrographic profiles results in a heat-flux estimate of 0.6 GW. The total rise time of the model plume is again of order 1 h and the temperature anomaly at the level of neutral buoyancy is -0.04°C. The apparent increase in heat flux, compared to 1997, is not considered significant, primarily because the mean 1998 hydrography of the SW basin is derived from only 4 profiles and because of the strongly sheared flow on the western slope of *Rainbow Ridge* bisecting the plume (section 5.3). Given this strong shear it is not *a-priori* clear if the model of *Morton, Taylor, and Turner* (1956) is applicable or if background turbulence affects the plume rise as is often the case in the atmospheric environment (e.g. *Priestley,* 1956).

The height-of-rise method as used here is closely related to estimating the source buoyancy flux B_i from the maximum height z^* attained by a plume rising from a point source into a linearly stratified stagnant background, using

$$z^* = 3.8 B_i^{1/4} N^{-3/4} \tag{7.5}$$

(e.g. *Turner,* 1986). The source buoyancy flux therefore depends on the fourth power of the rise height and on the third power of the buoyancy frequency, indicating that even in the absence of the problems mentioned above, heat fluxes derived from buoyancy flux estimates based on height-of-rise modeling are associated with large uncertainties (e.g. *Speer and Helfrich,* 1995).

The effects of the Earth's rotation have been ignored in above calculations. Direct effects on rising plume fluid can be disregarded because of the short rise times which are small compared to the inertial period of 20 h. (Laboratory experiments of thermals rising into stratified stagnant backgrounds indicate that rotational effects can be ignored as long as $N/f < 0.6$ *(Helfrich,* 1994); in the *AMAR* segments $N \approx 10^{-3}\,\mathrm{s}^{-1}$ (section 3.2.3), implying that $N/f \approx 0.1$.) The numerical experiments of *Speer and Marshall* (1995) show that the rise height of starting plumes can be influenced indirectly by rotational effects because of the cyclonic flow set up around the buoyant plumes if the buoyancy sources persist longer

than an inertial period. Direct velocity observations in the vicinity of the *Rainbow* vent field (section 3.2.3 and chapter 4) indicate that the dynamics are dominated by the along-valley flow without any indications for a plume-driven cyclonic circulation. Therefore, it appears reasonable to assume that the hydrothermal effluents rise into "pristine" background water carried to the vent field by the along-valley flow, implying that rotational effects on plume rise can be ignored.

7.3 Advective Flux in the 1997 Particle Plume

To derive an estimate which does not depend on any of the assumptions required for the height-of-rise method (section 7.2), an alternative approach based on the advective flux of the equilibrium plume temperature anomalies $\Delta\theta_e$ is used *(Baker and Massoth,* 1987). The Gaussian shape of the density-averaged plume observed in 1997 (section 5.2) supports the assumption of quasi-steadiness, so that the equilibrium temperature-anomaly flux can be defined as

$$Q_e\overline{\Delta\theta_e} = \int \Delta\theta_e U_n dE \tag{7.6}$$

where Q_e is the volume flux carrying the spatially averaged temperature anomaly $\overline{\Delta\theta_e}$ away from the "source" (which in this context is the region where the buoyant plumes become neutrally buoyant). The integral is evaluated over a suitably defined section E across which the entire equilibrium plume is advected with velocity U_n (normal to E) away from the source. For a plume trapped in and advected unidirectionally along the rift valley any cross section down-stream from the source can be chosen for E (background fluid advected across the section has zero temperature anomalies by definition and does therefore not contribute to the total flux).

If the T/S relationship of the fluid entrained into the buoyant plumes is linear the equilibrium temperature-anomaly flux $Q_e\overline{\Delta\theta_e}$ is related to the corresponding source temperature-anomaly flux $Q_i\overline{\Delta\theta_i}$ by expression (6.1). The stability ratio for the 1997 data $R_\rho = 2.36$ is taken from section 6.6 and the source-fluid density-anomaly ratio $R_\rho^i \approx 5.4$ is estimated from the effluent properties measured in the *Rainbow* hydrothermal vent field approximately one month after the *FLAME* cruise *(Fouquet et al.,* 1998). The source heat flux H is calculated using

$$H = \rho_i c_p Q_i \overline{\Delta\theta_i}, \tag{7.7}$$

where ρ_i is the "asymptotic" source-fluid density, i.e. calculated with the linear equation of state expanded at background temperature and salinity, and c_p is the corresponding low-temperature specific heat *(Turner and Campbell,* 1987).

Using the mean slope of the spice vs. nephel regressions of the 1997 *BRIDGET* data set $C = -0.019°\mathrm{C}\cdot\mathrm{V}^{-1}$ (section 6.6.1) to re-scale the near-source Gaussian light-scattering plume shown in Fig. 5.4 yields the temperature-anomaly profile

$$\Delta\theta_e(z) = C \times \Delta n^* \times \exp\left(-\frac{(z-\mu)^2}{2\sigma^2}\right) \tag{7.8}$$

with $\Delta n^* = 0.25\,\mathrm{V}$, $\mu = 2120\,\mathrm{m}$, and $\sigma = 96\,\mathrm{m}$ taken from the SW basin profile. The peak temperature anomaly becomes $-4.8 \times 10^{-3}\,°\mathrm{C}$, an order of magnitude less than the anomalies predicted by the bulk plume model (section 7.2).

The heat flux is now estimated using expressions (7.6) and (7.7). The plume width is taken to be 2 km (section 5.2) and the mean near-source velocity profile (Fig. 3.10) is approximated by

$$U_n(z) = U_0 + \frac{\partial U}{\partial z}(z - z_0), \tag{7.9}$$

with $U_0 = 0.05\,\mathrm{m}\cdot\mathrm{s}^{-1}$, $\partial U/\partial z = 2.5 \times 10^{-4}\,\mathrm{s}^{-1}$, and $z_0 = 1900\,\mathrm{m}$. Integrating $\Delta\theta_e(z)U_n(z)$ between 1900 m and 2300 m across the plume width yields $Q_e\overline{\Delta\theta_e} \approx -230°\mathrm{C}\cdot\mathrm{m}^3\cdot\mathrm{s}^{-1}$. The source temperature-anomaly flux becomes $Q_i\overline{\Delta\theta_i} \approx 550°\mathrm{C}\cdot\mathrm{m}^3\cdot\mathrm{s}^{-1}$, corresponding to a heat flux estimate of 2.3 GW. (Using this flux to force the bulk plume model of section 7.2 results in a predicted maximum rise height of 600 m.) Considering the number of assumptions and estimates the heat-flux value is based on it is difficult to determine a confidence interval. In contrast to the rise-height method, none of the parameters is raised to a power greater than one, however, and those with the greatest uncertainties, namely the width of the plume and the mean current speed, are most likely accurate at least within a factor of two. Therefore, the lower and upper bounds of the heat flux are estimated to be 1 GW and 5 GW, respectively.

7.4 Discussion

Two estimates for the heat flux associated with the hydrothermal particle plume of the 1997 data set differing by an order of magnitude have been calculated. Because the plume rise height is not significantly larger than the horizontal extent of the hydrothermal vent field the point-source assumption required for the height-of-rise estimate is violated and the resulting 0.3 GW are not considered to be accurate.

The hydrographic anomalies associated with the near-source particle plume together with the boundary current observations from the western slope of *Rainbow Ridge* allow the heat flux to be estimated using an alternative method. Because of the simplicity of the near-source flow field advecting the plume unidirectionally along the western slope of *Rainbow Ridge* and because of the consistency of the relationship between the temperature and the nephelometry anomalies in the near-source profiles, implying accurate temperature-anomaly estimates, the value of 2.3 GW derived with this method is much more likely to represent the integrated high-temperature heat flux from the vent field during the 1997 survey.

The factor-10 difference between the two estimates is interesting. *Fouquet et al.* (1998) describe the distribution of the vent chimneys at *Rainbow* as *"about ten major groups of extremely active black smokers"*. The two heat-flux estimates are mutually consistent if the plumes from the different groups coalesce high enough in the water column so that they have already lost much of their buoyancy, i.e. the height-of-rise method yields a heat flux consistent with a single group of vents.

A third method to derive a rough estimate of the heat flux consists in taking a "canonical" value expected for a single vent chimney (0.05 GW, e.g. *Speer and Rona,* 1989; *Lupton,* 1995) and extrapolating that value to a group of vents (4–5, estimated from a video tape recorded during a submersible dive at the *Rainbow* hydrothermal site), resulting in a value of 0.2–0.25 GW, close to the value derived from height-of-rise modeling. Extrapolating this value to the entire vent field (10 groups of chimneys) yields 2–2.5 GW, consistent with the estimate derived from the advective temperature-anomaly flux.

Hydrothermal vent fields are commonly composed of numerous individual sources, indicating that heat fluxes derived using the height-of-rise method at other sites may be underestimates as well. The simplicity of the flow field in the vicinity of the *Rainbow* vent field allows the advective temperature-anomaly flux to be calculated with a high degree of confidence. At other sites (e.g. TAG, where there is no strong mean flow) this method may not be as useful, indicating that it can be extremely difficult to estimate heat fluxes from physical measurements in the equilibrium plumes.

Chapter 8

Mass and Heat Budgets of the *AMAR* Segments

8.1 Introduction

In this chapter mass (volume) and heat budgets of the *AMAR* segments are calculated. The main goals are to investigate the pathways of the rift-valley water, to infer the amount of mixing required to sustain the observed along-segment hydrographic gradients, and to assess the importance of geothermal heating within the rift valley. A steady-state assumption is made, motivated by the hydrographic and flow observations (chapters 3 and 4). To simplify the discussions the sills below 2000 m are labeled as shown in Fig. 8.1 (e.g. *Rainbow Sill* is called sill "R").

In section 8.2 the heat budget beneath an isopycnal surface grounding within the rift valley is calculated. While known geothermal contributions (including the heat flux from the *Rainbow* hydrothermal vent field) do not have a significant impact, a bulk diapycnal diffusivity (K_v) of order $5 \times 10^{-3}\,\mathrm{m^2 \cdot s^{-1}}$ is required to supply sufficient heat to the water beneath the grounding isopycnal. Mass budgets for the rift valley below 2000 m are calculated next (section 8.3). The pathways of the rift-valley water are associated with considerable uncertainties but the observations suggest that approximately half of the water entering *South AMAR* below 2000 m flows into the *FAMOUS* segment. The remainder is most likely "lost" either by outflows across additional sills or by "entrainment" into the overlying water column. Using the volume budgets together with hydrographic data, heat budgets for the

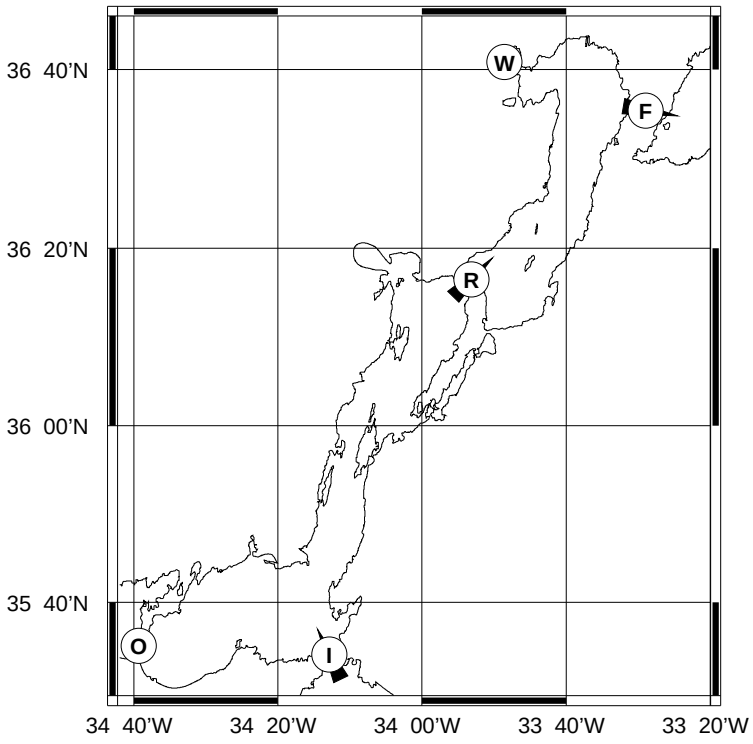

Fig. 8.1: 2250 m bathymetric contours of the *AMAR* rift valley and locations (and inferred flow directions where available; c.f. section 8.3) of the sills below 2000 m.

along-segment flow below 2000 m are calculated. Bulk diapycnal-diffusivity estimates calculated from these heat budgets are of order $5 \times 10^{-3}\,\mathrm{m^2 \cdot s^{-1}}$ for both *AMAR* segments, i.e. consistent with the value calculated in section 8.2. The chapter concludes with a discussion in section 8.4.

8.2 Heat Budget Beneath a Grounding Isopycnal

Fig. 8.2 shows an along-segment density section of the rift valley between sills "I" and "F". The shaded area indicates densities corresponding to the water flowing into *South AMAR* below 2000 m (i.e. the lower layer of the hydraulic calculation of section 3.3.3). Apart from sill "I" the rift valley is closed below 2200 m (section 1.3.3), indicating that lower-layer water does not flow out of *AMAR* north of 36°N. South of 36°N there may be outflow across sill "O" connecting *South AMAR* to the *North Oceanographer* segment. (The hydrographic sections of *Wilson et al.* (1995) appear more consistent with flow from *North Oceanographer* into *AMAR*, however.) Extrapolating the depth trend of the interface between the inflow

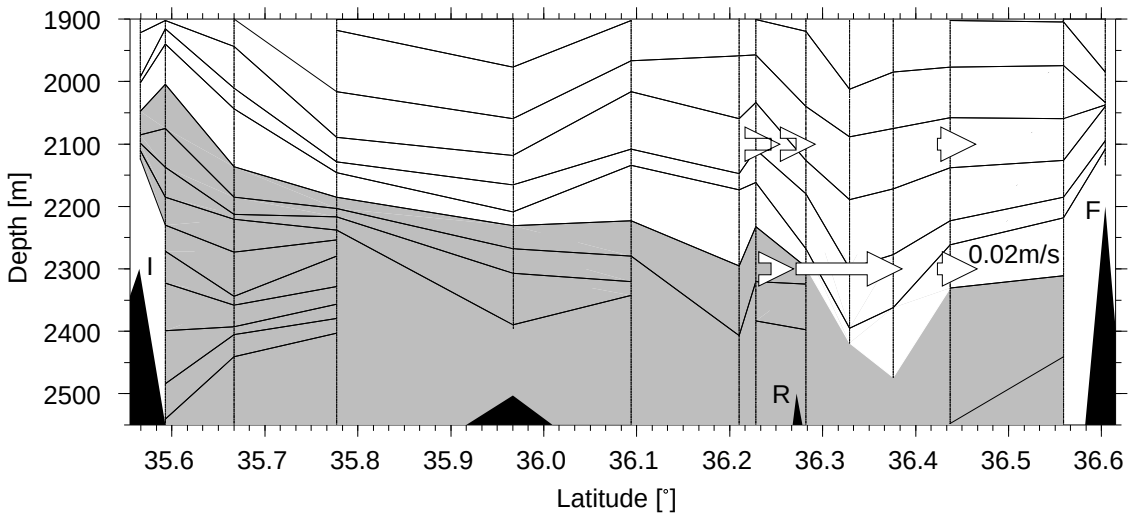

Fig. 8.2: Rift-valley density section of the *AMAR* segments and current meter observations (mean along-valley velocities recorded at moorings G, B and F during the final week of deployment); black triangles indicate the bathymetry rising above 2550 m; sills are labeled as in Fig. 8.1; shading ($\sigma_2 \leq 36.9449$) and non-uniformly spaced contours are the same as in Fig. 3.19 (p.42).

(2000 m) and the westernmost station (2134 m) occupied during the 1998 survey (Fig. 2.2) to sill "O" yields a value of 2320 m, i.e. below the sill depth of 2200 m. It is therefore tentatively assumed that there is no outflow of lower-layer water from the *AMAR* segments, i.e. the isopycnal associated with the interface at the inflow grounds within the *AMAR* segments. Even if this assumption is violated, the volume flux estimates across sills "I" (section 3.3.3) and "R" (sections 3.2.3 and 4.5) indicate that it is unlikely that more than a third of the water entering *South AMAR* below 2000 m is lost across sill "O" (see also section 8.3).

The heat budget beneath the grounding isopycnal is given by

$$\rho_0 c_p Q_i \overline{\Delta\theta} = H_c + H_p + \rho_0 c_p A_\rho K_v \theta_z \tag{8.1}$$

(e.g. *Saunders,* 1987), where Q_i is the lower-layer volume flux entering *South AMAR* and $\overline{\Delta\theta}$ denotes the mean temperature by which the inflowing water must be heated to cross the grounding isopycnal. H_c and H_p are the conductive and convective geothermal heat fluxes into the lower layer. A_ρ is the horizontal area of the interface, and θ_z is the mean vertical temperature gradient at the grounding isopycnal. The mean lower-layer temperature deficit $\overline{\Delta\theta} = 0.13°\mathrm{C}$ is taken from the CTD tow-yo at sill "I" assuming an interface depth of 2000 m (section 3.3.3). With the corresponding volume flux estimate $Q_i = 95 \times 10^3\,\mathrm{m^3 \cdot s^{-1}}$

the heat flux which must be supplied by geothermal heating and diapycnal diffusion becomes 5.2×10^{10} W.

The conductive heat flux $H_c \approx 328 \times 10^6$ W is calculated from the near-axial heat flow value of 131×10^{-3} W·m^{-2} *(Stein and Stein,* 1994) and $A_\rho = 2.5 \times 10^9$ m^2, estimated from the area enclosed by the 2250 m bathymetric contour (Fig. 8.1), the mean depth of the grounding isopycnal. The small contribution of H_c to the overall budget of expression (8.1) is consistent with the lack of geothermal heating signatures in the along-segment hydrographic properties (section 3.3.2). Near *Rainbow Sill* the depth of the grounding isopycnal is approximately 2300 m (Fig. 8.2), implying that the bulk of the convective heat flux from the *Rainbow* hydrothermal vent field (at 2300 m) does not contribute to the heat balance of the lower layer (c.f. Fig. 5.4). Even the entire convective heat flux of 2.5×10^9 W calculated from the 1997 data (section 7.3) does not significantly change the balance of expression (8.1), indicating that geothermal contributions have a minor impact on the heat budget of the *AMAR* segments, provided there are no additional major undetected heat sources such as significant low-temperature hydrothermal circulation. The mean temperature gradient at the interface $\theta_z = 6.2 \times 10^{-4}$ °C·m^{-1} is estimated from 100 m-thick layers centered at the grounding isopycnal in the deep rift-valley profiles of the 1998 survey (section 3.3.2). Using these estimates expression (8.1) yields $K_v = 8.4 \times 10^{-3}$ m^2·s^{-1}. This value is reduced by half if the lower bound of the volume flux estimate at sill "I" (section 3.3.3), and a correspondingly re-defined mean lower-layer temperature deficit $\overline{\Delta\theta} = 0.10$°C, is used (i.e. assuming an interface depth of 2050 m) or if it is assumed that half of the inflow across sill "I" is lost by outflow across sill "O".

The same method has been used to estimate diapycnal mixing coefficients before, e.g. by *Whitehead and Worthington* (1982) for Antarctic Bottom Water (AABW) in the North Atlantic ($K_v = 0.7 \times 10^{-4}$ m^2·s^{-1} and $K_v = 3.7 \times 10^{-4}$ m^2·s^{-1} based on two different volume flux estimates), by *Hogg et al.*(1982) for AABW in the Brazil Basin ($K_v = 3$–4×10^{-4} m^2·s^{-1}), and by *Saunders* (1987) for the water flowing through Discovery Gap into the Iberian Abyssal Plane ($K_v = 2 \times 10^{-4}$ m^2·s^{-1}). Using a different method based on a vertical advection/diffusion balance *Read and Pollard* (1999) calculated a basin-wide diffusivity average $K_v = 10^{-3}$ m^2·s^{-1} from the hydrography of the Mozambique basin. In regions of strong flow much higher mean values are possible as shown by *Polzin et al.* (1996) who estimated a mean vertical diffusivity $K_v = 1.5 \times 10^{-2}$ m^2·s^{-1} from temperature microstructure profiles in the rapidly flowing (0.1–0.5 m·s^{-1}) bottom layer of the Romanche Fracture Zone.

8.3 Rift-Valley Mass and Heat Budgets

To calculate heat budgets of the rift valley below 2000 m the corresponding mass (volume) budgets are required. Based on the hydraulic volume flux estimates across sills "I" (section 3.3.3) and "R" (section 3.2.3) the volume budget of *South AMAR* below 2000 m is characterized by inflow from the eastern ridge flank of $95 \times 10^3\,\mathrm{m^3 \cdot s^{-1}}$ and outflow across *Rainbow Sill* of $65 \times 10^3\,\mathrm{m^3 \cdot s^{-1}}$, leaving a deficit of $30 \times 10^3\,\mathrm{m^3 \cdot s^{-1}}$. While outflow across sill "O" can balance this budget, the hydrographic sections of *Wilson et al.* (1995) appear more consistent with inflow. Furthermore, there are other potential sinks for the rift-valley water entering *South AMAR* (see below).

Deriving a similar budget for *AMAR* is associated with even greater uncertainties. The deepest sill near the northern end of the segment connects the rift valley to the *FAMOUS* segment at 2200 m (sill "F"). The available bathymetry does not rule out an additional sill (sill "W") connecting *AMAR* to the western ridge flank at some depth above 2100 m. The northernmost rift-valley profiles of both hydrographic surveys indicate higher densities at 2100 m than in a western ridge-flank background profile, with differences $< 10^{-2}\,\mathrm{kg \cdot m^{-3}}$. Applying the hydraulic model of *Whitehead, Leetmaa, and Knox* (1974) (c.f. section 3.2.3, with assumed sill and interface depths of 2100 m and 2000 m, respectively) yields volume flux estimates $< 6 \times 10^3\,\mathrm{m^3 \cdot s^{-1}}$, i.e. less than 10% of the water entering *AMAR* across *Rainbow Sill* below 2000 m.

The most likely pathway out of the segment for the bulk of the water flowing across *Rainbow Sill* into *AMAR* is therefore across sill "F". (The hydrographic sections of *Wilson et al.* (1995) appear consistent with this view.) Fig. 8.3 shows data from a station occupied directly on that sill. Between 2020 m and 2040 m the density profile is characterized by a steep gradient. The corresponding θ_2/S properties rule out instrument problems and suggest that the water above and below the density step is most likely of the same origin, i.e. eastern North Atlantic water. (The slight change in the θ_2/S slope near 4.2°C is consistent with other rift-valley profiles of the 1998 survey, e.g. Fig. 3.14.) The available bathymetric data sets indicate that the *FAMOUS* segments are closed below 2000 m with the exception of sill "F" and an additional sill on the eastern rift-valley wall near 36°25′N/32°55′W with a minimum depth between 2000 m and 2100 m. Inflow of eastern ridge-flank water into *FAMOUS* and overflow across sill "F" into *AMAR* is therefore as consistent with the θ_2/S observations of Fig. 8.3

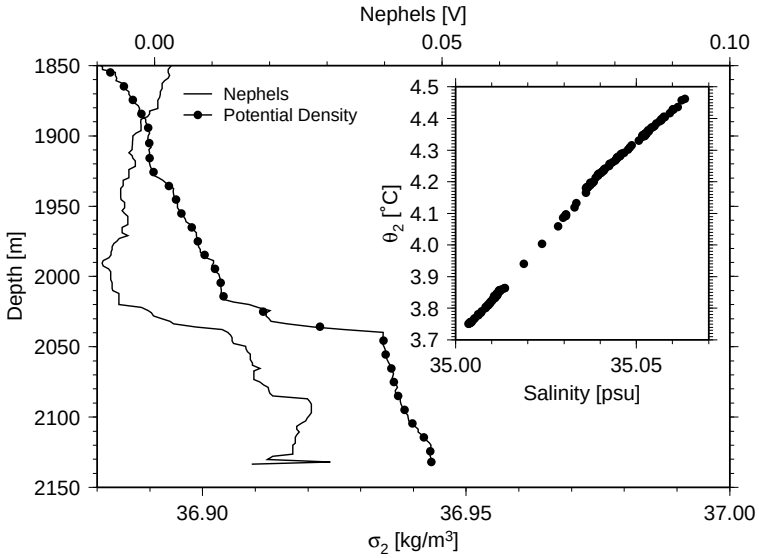

Fig. 8.3: Hydrographic and light-scattering observations from sill "F" connecting the *AMAR* and *FAMOUS* segments; in the main panel the potential density and nephelometry profiles are plotted; the inset shows the corresponding θ_2/S properties.

as is flow from *AMAR* into *FAMOUS*. The increased light-scattering signals observed below the density step suggest two layers of water, possibly flowing in different directions. While no light-scattering data is available from *FAMOUS* the observed nephelometry signal is consistent with the rift-valley properties of the *AMAR* segments where nearly all nephelometry profiles contain weak maxima of 0.01–0.02 V near 2100 m.

Attempting to infer the flow direction below 2000 m across sill "F" from Fig. 8.2 does not lead to unambiguous conclusions either. The density patterns near the northern and southern ends of the *AMAR* segments are similar, i.e. consistent with inflow from *FAMOUS* into *AMAR*. The current-meter measurements on the other hand indicate northward mean flow into the region of the upsloping isopycnal surfaces (c.f. section 4.5.1). Isopycnal uplifting upstream of *Rainbow Sill* was observed in 1997 (section 3.2.3) and there are indications for the same effect in Fig. 8.2. Our data do therefore not allow to infer a mean flow direction across sill "F" with confidence. It is nevertheless tentatively assumed that the flow is from *AMAR* into *FAMOUS*, primarily because added inflow into *AMAR* would require a large outflow, presumably across sill "W", which does not appear consistent with our density observations.

The volume flux across sill "F" is estimated with the hydraulic model of *Whitehead, Leetmaa, and Knox* (1974) (c.f. section 3.2.3). No cross-sill density section is available, implying

	South AMAR			*AMAR*		
	Q	$\overline{\theta_2}$	$\rho_0 c_p Q \overline{\theta_2}$	Q	$\overline{\theta_2}$	$\rho_0 c_p Q \overline{\theta_2}$
	$[\mathrm{m^3 \cdot s^{-1}}]$	$[^\circ\mathrm{C}]$	$[\mathrm{W}]$	$[\mathrm{m^3 \cdot s^{-1}}]$	$[^\circ\mathrm{C}]$	$[\mathrm{W}]$
Inflow	95×10^3	3.634	1.45×10^{12}	65×10^3	3.777	1.03×10^{12}
Outflow	-65×10^3	3.777	-1.03×10^{12}	-50×10^3	3.904	-0.82×10^{12}
Deficit	-30×10^3	3.710	-0.47×10^{12}	-15×10^3	3.841	-0.24×10^{12}
Balance			4.79×10^{10}			3.08×10^{10}

Table 8.1: Volume and heat budgets of the *AMAR* segments; volume fluxes (Q) are taken from sills "I", "R" and "F"; average temperatures below 2000 m ($\overline{\theta_2}$) are taken from CTD profiles; "Balance" denotes the amount of heat required to close the budgets (LHS of expression (8.1)).

that the interface height and density difference between the two layers must be estimated with an alternative method. Using the density step observed on the sill (Fig. 8.3) to derive a reduced gravity and interface height yields $g' = 3 \times 10^{-4}\,\mathrm{m \cdot s^{-2}}$ and $h_u = 170\,\mathrm{m}$ (from the altimeter at 2030 m, the center of the density step). The Rossby radius of deformation corresponding to these values is 2.6 km, less than the sill width of 5 km at 2000 m, indicating that the hydraulic model can be applied as before, yielding a volume flux estimate of $50 \times 10^3\,\mathrm{m^3 \cdot s^{-1}}$. The corresponding flow velocity estimated from the interfacial wave speed is $0.23\,\mathrm{m \cdot s^{-1}}$. The most likely volume budget for the *AMAR* segment is therefore characterized by inflow across *Rainbow Sill* of $65 \times 10^3\,\mathrm{m^3 \cdot s^{-1}}$ and outflow into *FAMOUS* of $50 \times 10^3\,\mathrm{m^3 \cdot s^{-1}}$, leaving a deficit of $15 \times 10^3\,\mathrm{m^3 \cdot s^{-1}}$.

It will be noted that the apparent volume flux deficits of the *AMAR* segments are proportional to the lengths (or areas) of the segments. While additional outflows across sills "O" and "W" can balance the budgets it appears also possible that some of the rift-valley water is lost to the overlying water column (see below). Using the horizontal area of the *AMAR* segments at 2000 m (calculated from the mean rift-valley width of 20 km at 2000 m and the length of the segments, i.e. 100 km for *South AMAR* and 50 km for *AMAR),* the apparent volume-flux deficits imply a vertical velocity of $1.5 \times 10^{-5}\,\mathrm{m \cdot s^{-1}}$. (For comparison, *Read and Pollard* (1999) estimated a value of $10^{-5}\,\mathrm{m \cdot s^{-1}}$ for the entire Mozambique basin.)

Combining the volume flux budgets of the *AMAR* segments with hydrographic data from the 1998 survey, heat budgets are calculated as shown in Table 8.1. The average temperatures of the overflows below 2000 m are taken from the CTD tow-yo across sill "I" (Fig. 3.19), from

the 1998 CTD stations occupied in the vicinity of *Rainbow Ridge* (Fig. 2.2), and from the profile shown in Fig. 8.3, respectively. The temperatures associated with the volume flux deficits are set to the average values of the inflows and outflows. From these heat balances diapycnal-diffusivity estimates are calculated using expression (8.1) with $\theta_z = 1.3 \times 10^{-3}\,^{\circ}\mathrm{C}\cdot\mathrm{m}^{-1}$, estimated from 100 m-thick layers centered at 2000 m (c.f. section 8.2). The known geothermal contributions (H_c and H_p) again have a minor impact on the budgets. The estimates for the diapycnal diffusivities become $K_v = 4.1 \times 10^{-3}\,\mathrm{m}^2\cdot\mathrm{s}^{-1}$ *(South AMAR)* and $K_v = 5.6 \times 10^{-3}\,\mathrm{m}^2\cdot\mathrm{s}^{-1}$ *(AMAR)*. Taking a conservative approach by assuming that the apparent volume flux deficits are caused by overestimates of the inflowing volume fluxes (which is more conservative than assuming that the deficits are caused by additional outflows across sills "O" and "W") yields $K_v = 3.3 \times 10^{-3}\,\mathrm{m}^2\cdot\mathrm{s}^{-1}$ *(South AMAR)* and $K_v = 4.8 \times 10^{-3}\,\mathrm{m}^2\cdot\mathrm{s}^{-1}$ *(AMAR)*. If the flow below 2000 m across sill "F" is from *FAMOUS* into *AMAR* no heat budgets and corresponding diffusivities can be estimated for the *AMAR* segment.

8.4 Discussion

Diapycnal-diffusivity estimates for the *AMAR* segments calculated from heat budgets result in bulk values of $3\text{–}8 \times 10^{-3}\,\mathrm{m}^2\cdot\mathrm{s}^{-1}$. There are significant uncertainties associated with the budgets, primarily because the pathways of the rift-valley water are not well constrained by our data, but even with conservative assumptions the diffusivities remain of order $5 \times 10^{-3}\,\mathrm{m}^3\cdot\mathrm{s}^{-1}$. Circumstantial evidence for strong diapycnal mixing in the rift valley of the *AMAR* segments was presented in chapters 3, 4 and 5. Without confirmation from more direct measurements, such as microstructure profiles, the diffusivity estimates (and, hence, the following discussion) must remain associated with some doubt. The consistency of the picture which emerges from the volume and heat budgets is encouraging, however. It is difficult to see how an alternative view, e.g. additional inflow from *FAMOUS*, could yield similarly consistent results.

The heat budgets indicate that the known geothermal contributions to the rift-valley water column of the *AMAR* segments are not significant in relation to other processes, even in the presence of the large heat flux from the *Rainbow* hydrothermal vent field. This is consistent with the mutual consistency of the rift-valley θ_2/S properties along the *AMAR* segments (section 3.3.2) and with the apparent lack of plume-related dynamical signatures

in the LADCP (section 3.2.3) and current-meter data (section 4.3.2), implying that the rift-valley hydrography and dynamics are dominated by processes which are not associated with the hydrothermal plume. The observation that mixing within the rift valley of the MAR can have a much stronger effect on the density field than a large hydrothermal plume supports the conclusion of *Talley and Johnson* (1994) that hydrothermal plumes may not be the (primary) driving mechanism for the westward mid-depth flows observed in the Pacific and in the Atlantic ocean, and provides a plausible explanation why hydrographic exploration of the MAR rift valley has failed to detect even large hydrothermal plumes (e.g. *Wilson et al.*, 1995).

The mass budgets derived for the *AMAR* segments suggest that not all the water entering the rift valley below 2000 m flows out across the deepest sills. There are three possibilities to account for the observations:

- uncertainties in the volume-flux estimates can result in false apparent deficits;
- the deficits can be caused by outflows across additional sills;
- rift-valley water can be lost to the overlying water column.

Our data do not rule out any of these possibilities. Hydraulically controlled outflows across sills can balance the inflows if there are sufficient density gradients in the off-ridge water column between the inflows and the outflows to compensate the along-segment hydrographic gradients within the rift-valley. Our profiles (e.g. Fig. 3.2) as well as other data (e.g. *Fukumori et al.*, 1991) indicate that there is a (possibly persistent) cross-MAR density gradient near 36°N which favors inflow into the rift-valley from the east and outflow towards the west. The magnitude of the cross-ridge density difference at 2000 m is of order $3 \times 10^{-2}\,\mathrm{kg \cdot m^{-3}}$ implying that an along-segment flow of approximately 300 km can be driven if the observed rift-valley density gradient of $10^{-4}\,\mathrm{kg \cdot m^{-3} \cdot km^{-1}}$ (section 3.3.2) is representative. Nevertheless, the deep rift-valley water must be uplifted to any such outflow sill because below 2200 m even the water on the western ridge flank is denser than the rift-valley water at the same depth (Fig. 3.2). If vertical transport is required it does not seem unreasonable to suggest that some of the rift-valley water may be mixed ("entrained") into the overlying water column, providing a "diffuse" pathway for the water and the associated hydrothermal tracers out of the *AMAR* segments.

Chapter 9

A Simple Basin/Sill Model

9.1 Introduction

In this chapter the low-frequency (with time scales of weeks or longer) response characteristics of a simple basin/sill system (intended to represent the rift valley of the $AMAR$ segments) are investigated with an analytical and numerical model. In section 9.2 the $1\frac{1}{2}$-layer model consisting of a deep basin and a hydraulically controlled overflow is formulated. In section 9.3 the governing equation is solved analytically for steady inflow into the lower layer. The solutions show that adjustment of the outflow to abrupt changes at the inflow takes place over timescales of weeks to months when using parameters representative of the $AMAR$ segments. Numerical solutions (section 9.4) show that the model basin acts as an effective low-pass filter for oscillatory and event-like disturbances at the inflow. The chapter concludes with a discussion in section 9.5.

9.2 Model Formulation

Fig. 9.1 illustrates the simple 2-dimensional (along-valley and vertical) $1\frac{1}{2}$-layer (reduced-gravity) model intended to investigate the low-frequency along-valley flow within the $AMAR$ segments. The rift valley is represented as a flat-bottom basin of length l and depth d. The model is forced by prescribing a volume flux Q_i into the lower layer. Fluid can leave the model basin across an outflow sill (Q_o) and across the horizontal interface (Q_u). The interface height above the outflow sill is denoted by $h \geq 0$. Ignoring thermal expansion, conservation

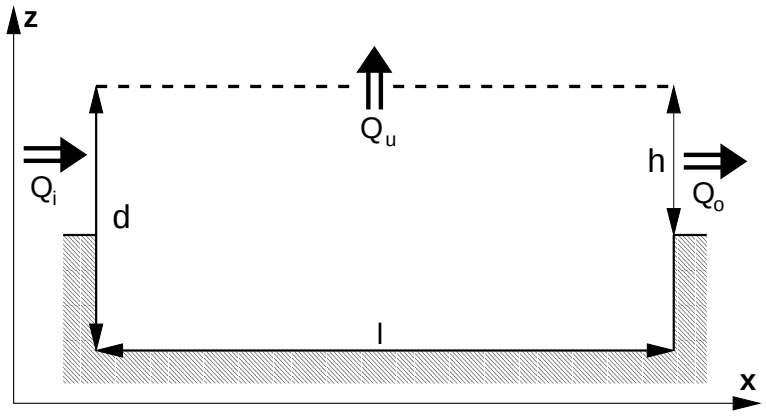

Fig. 9.1: Sketch of the $1\frac{1}{2}$-layer model consisting of a square basin of length l and depth d; the model is forced by inflow Q_i into the lower layer; fluid can leave the basin across an outflow sill (Q_o) and across the dashed horizontal interface (Q_u); the interface height above the outflow sill is denoted by h.

of volume becomes

$$l\frac{\mathrm{d}}{\mathrm{d}t}h = Q_i - Q_u - Q_o. \tag{9.1}$$

The dynamics of the flow within the basin are not resolved, implying that the model is only valid for time scales much longer than it takes transients to propagate along the entire length of the basin. Using the length ($l = 100\,\mathrm{km}$) and the mean depth below 2000 m ($d = 500\,\mathrm{m}$) of the *South AMAR* segment (Fig. 1.2) as well as reduced-gravity estimates from the hydraulic calculations at the inflow and at *Rainbow Sill* ($g' = 0.5\text{–}1.8 \times 10^{-4}\,\mathrm{m\cdot s^{-2}}$; sections 3.2.3 and 3.3.3) yields a time scale of 4–7 days for long gravity waves to propagate between the two sills. On longer time scales the interface adjusts instantaneously to changes at the inflow. (The model does not support slower waves such as higher-mode baroclinic gravity waves and topographic Rossby waves (c.f. section 4.3), i.e. it is assumed that the dynamically important transients in the rift valley are Kelvin waves which propagate with the same speed as long interfacial gravity waves (e.g. *Gill,* 1982).)

The outflow Q_o is parameterized using the wide-sill hydraulic model of *Whitehead, Leetmaa, and Knox* (1974) adapted to the 2-dimensional case, and representing the effect of outflow across multiple sills by a scale factor $\kappa \geq 1$, i.e.

$$Q_o = \kappa\frac{g'h^2}{2fw}, \tag{9.2}$$

where w is the width of the model basin. Substituting expression (9.2) into (9.1) yields

$$l\frac{\mathrm{d}h}{\mathrm{d}t} = Q_i - Q_u - \kappa\frac{g'h^2}{2wf}. \tag{9.3}$$

In this framework the apparent volume-flux deficits of the *AMAR* segments (chapter 8) can be represented as follows:

volume flux is conserved (i.e. the apparent deficits are caused by uncertainties in the volume-flux budgets) $\Rightarrow Q_u = 0$, $\kappa = 1$;

outflow across multiple sills $\Rightarrow Q_u = 0$, $\kappa = Q_i^*/Q_o^*$, where Q_i^* and Q_o^* are the observed volume fluxes taken from Table 8.1, i.e. $\kappa = 1.5$ *(South AMAR)* and $\kappa = 1.3$ *(AMAR);*

"entrainment" into the upper layer $\Rightarrow Q_u = (Q_i^* - Q_o^*)/w$, $\kappa = 1$, where $w = 20\,\mathrm{km}$ is the mean rift-valley width at 2000 m (Fig. 1.2).

Expression (9.3) implies that the effect of loss of lower-layer fluid across the interface (i.e. $Q_i = Q_i^*/w$, $Q_u = (Q_i^* - Q_o^*)/w$) is equivalent to the case where the model is forced with a reduced inflow (i.e. $Q_i = Q_o^*/w$, $Q_u = 0$).

9.3 Steady Forcing

The steady-state solution of expression (9.3) yields the equilibrium interface height

$$h_{eq} = \left(\frac{2(Q_i - Q_u)wf}{\kappa g'}\right)^{1/2}, \tag{9.4}$$

which is real for $Q_i \geq Q_u$. To investigate the model response to abrupt changes from an initial condition specified by h_0 expression (9.3) is solved analytically for two cases of steady forcing:

$Q_i - Q_u \geq \kappa g' h_0^2/(2fw)$**:** The interface adjusts upwards to accommodate an increased inflow (i.e. $h_{eq} \geq h_0$). The solution of the initial-value problem is

$$h(t) = h_{eq}\frac{\exp(t/\tau + s) - 1}{\exp(t/\tau + s) + 1}, \tag{9.5}$$

where

$$\tau = l\left(\frac{wf}{2\kappa(Q_i - Q_u)g'}\right)^{1/2} \tag{9.6}$$

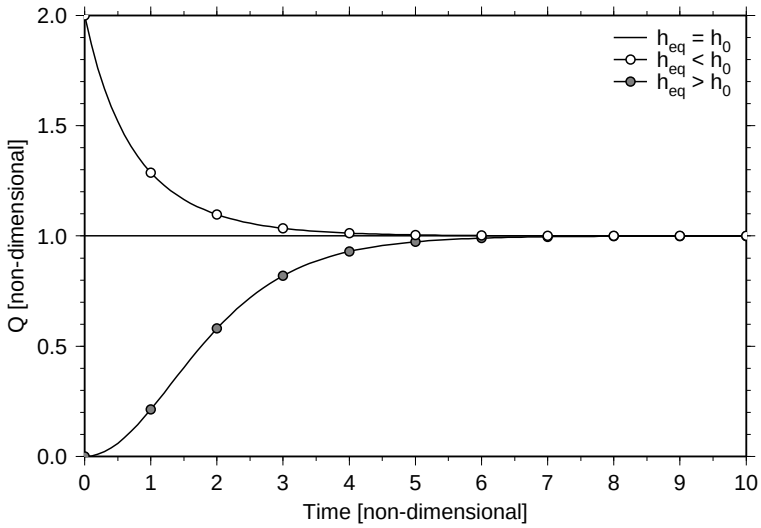

Fig. 9.2: Non-dimensional analytical solutions of expression (9.3) for steady forcing $Q_i - Q_u = 1$; the three curves show the steady state ($h_{eq} = h_0$), expression (9.8) with $h_0 = 2h_{eq}$, and expression (9.5) with $h_0 = 0$.

is a timescale of adjustment, and

$$s = \ln \frac{h_{eq} + h_0}{h_{eq} - h_0} \tag{9.7}$$

is a measure of the amount of adjustment required.

$0 < Q_i - Q_u \leq \kappa g' h_0^2/(2fw)$**:** The interface adjusts downwards to accommodate a decreased inflow (i.e. $h_{eq} \leq h_0$). The solution of the initial-value problem is

$$h(t) = h_{eq} \frac{1 + \exp(s' - t/\tau)}{1 - \exp(s' - t/\tau)}, \tag{9.8}$$

with

$$s' = \ln \frac{h_0 - h_{eq}}{h_0 + h_{eq}}. \tag{9.9}$$

The model response is expressed in terms of Q_o. Volume fluxes are non-dimensionalized with the steady-state flux observed at the outflow, i.e. with $Q_i - Q_u = Q_o^*/w$. Time is non-dimensionalized with τ calculated from the volume-flux scale. With these scalings the non-dimensional model solutions become independent of κ, i.e. they are fully specified by h_0 and $Q_i - Q_u$. Fig. 9.2 shows analytic solutions to steady-state forcing $Q_i - Q_u = 1$ for three initial conditions. The asymmetry of the solutions (i.e. the faster downward adjustment) reflects the non-linear dependence of Q_o on h in expression (9.2).

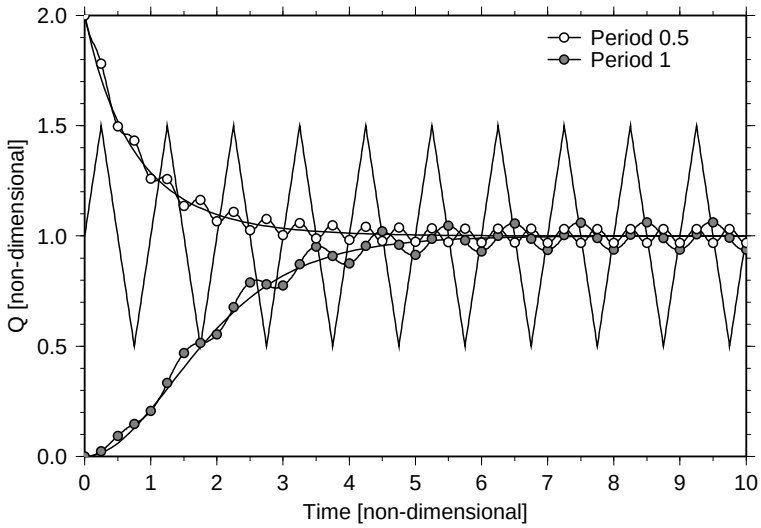

Fig. 9.3: Model responses to sawtooth forcing with (non-dimensional) amplitude 1, fluctuating around a mean of 1; responses to forcing with period 0.5 (not shown) and $h_0 = 2h_{eq}$, and to forcing with period 1 and $h_0 = 0$ are plotted; analytic solutions to steady-state forcing $Q_i - Q_u = 1$ are shown for comparison.

To estimate the time scales τ appropriate for the *AMAR* segments, values for $Q_i - Q_u$ and g' are taken from the hydraulic calculations at the outflows (sections 3.2.3 and 8.3). If the volume-flux deficits (section 9.2) are caused by "entrainment" into the overlying water column the time scales become 89 days for *South AMAR* and 20 days for *AMAR*. If the deficits are caused by additional outflows the corresponding time scales become 73 days for *South AMAR* ($\kappa = 1.5$) and 17 days for *AMAR* ($\kappa = 1.3$).

9.4 Non-Steady Forcing

To investigate the model responses to oscillatory forcing expression (9.3) is solved numerically for a variety of initial conditions, forcing amplitudes, frequencies and shapes. Fig. 9.3 shows model responses to sawtooth forcing with (non-dimensional) periods 0.5 and 1, and amplitudes 1 oscillating around a mean of $Q_i - Q_u = 1$. The model basin acts as an effective low-pass filter as indicated by the close resemblance of the numerical and the corresponding analytical solutions (for steady forcing with the same mean and the same initial conditions), by the near-sinusoidal responses to sawtooth forcing, and by the reduction of the model response amplitudes with increasing forcing frequency.

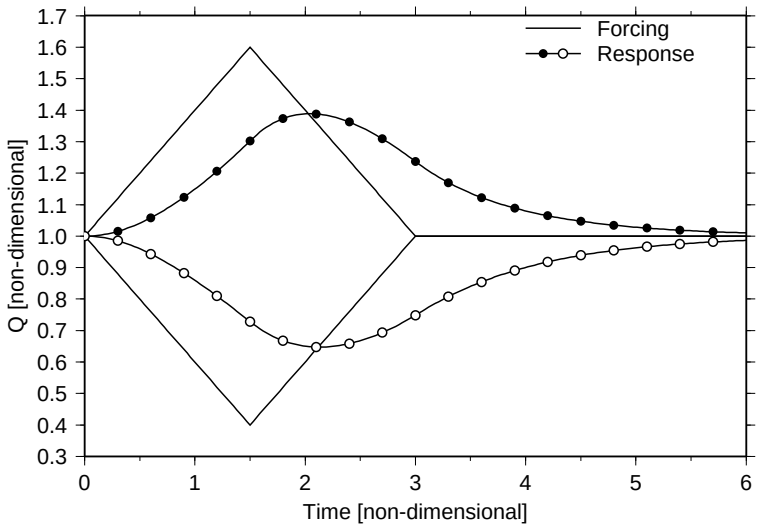

Fig. 9.4: Model adjustment to event-like deviations from the steady state $Q_i - Q_u = 1$; responses to positive and negative triangular spikes of amplitudes ± 0.6 and durations 3 are plotted.

To explore the responses of the model outflow to event-like disturbances expression (9.3) was solved numerically for a variety of deviations (of different shapes, durations and amplitudes) from the steady state. Fig. 9.4 shows two examples. The model outflow responds stronger to positive than to negative events and there is a temporal asymmetry in both cases. Responses to different event shapes are similar and the model response amplitudes decrease with decreasing event durations, consistent with the low-pass filtering property of the basin/sill combination.

9.5 Discussion

The simple model developed in this chapter indicates that basin/sill combinations act as effective low-pass filters. The model was developed with the intent to investigate some aspects of the low-frequency along-segment flow in the *AMAR* segments. The time scales derived from the appropriate parameters indicate that adjustment of the flow across *Rainbow Sill* to changes at the inflow takes months, while the inferred overflow from *AMAR* into *FAMOUS* responds with a time scale of weeks to changes at the *Rainbow Sill* overflow.

The parameter space of the model has been explored in greater detail than it is reported here but without any simultaneous inflow/outflow measurements or laboratory experiments

to validate the model solutions our confidence in the details of the results is limited, especially considering the simplicity of the model. The low-pass filtering property of basin/sill combinations does not depend on the model details, however. It is a direct consequence of the "storage capacity" (determined by the horizontal area) of the basin. This is easily observable, e.g. on rocky shores where breaking waves periodically supply water to small pools which can drain continuously without much apparent variability. Crudely representing the rift valley as such a basin/sill combination therefore provides a plausible explanation for the persistence of the *Rainbow Sill* overflow and for the apparent lack of transport variability observed during one year of direct measurements (chapter 4).

Chapter 10

Findings, Implications and Speculation

10.1 Main Observations and Conclusions

10.1.1 Observations

Rift-Valley Flow and Hydrography

1. Persistent unidirectional flow was observed in the rift-valley of the *AMAR* segments during a full year (1997–1998). The along-valley transport remained surprisingly constant in spite of a warming event shifting the flow patterns.

2. A range of processes potentially associated with high rates of diapycnal mixing were observed, including hydraulically controlled cross-sill flows, topographic lee waves, and strong tidal currents.

3. In the vicinity of eastern boundaries and on the saddle of a sill the flow energy was dominated by the lowest-frequency components. Elsewhere the semi-diurnal tide dominated with a range of additional energetic oscillations characterized by periods between 4 h and 14 days.

4. Except at the lowest frequencies the flow energy was dominated by the clockwise rotary component with the polarization decreasing with increasing depth.

5. In 1998 along-valley hydrographic gradients extending throughout the segments were

observed. Historical data are consistent with similar gradients in the *AMAR* segments in 1992 and in the rift valley of a segment near 45°N in 1979.

6. Volume-flux budgets of the *AMAR* segments indicate that there may be loss of water from the flow below 2000 m.

7. The convective heat flux from the *Rainbow* hydrothermal vent field together with conductive geothermal heating along the entire *AMAR* segments provide less than 10% of the thermal energy required to close the heat budgets of the rift valley.

8. Assuming that the heat budgets are balanced by diapycnal mixing yields bulk diffusivity estimates of order $5 \times 10^{-3}\,\mathrm{m^2 \cdot s^{-1}}$.

Basin/Sill Systems

1. Simple basin/sill combinations act as effective low-pass filters with time scales determined by the storage capacities of the basins.

Rainbow Hydrothermal Plume

1. In spite of high temporal and spatial near-field variability, the density-averaged particle plume was Gaussian in depth in 1997, without indications for layering caused by the multiple sources. In 1998 the plume was vertically bisected by a strongly sheared flow field dispersing the hydrothermal tracers both NE- and SW-ward away from the vent field.

2. In both years the particle plume was associated with cold/fresh isopycnal hydrographic anomalies proportional to the light-scattering signals. The 1997 near-field Gaussian mean plume was associated with peak hydrographic anomalies of $-5 \times 10^{-3}\,^{\circ}\mathrm{C}$ and -10^{-3} psu; peak anomalies in individual profiles were approximately six times higher.

3. The heat flux associated with the 1997 particle plume was approximately 2.5 GW. Height-of-rise modeling yields estimates which are an order of magnitude smaller.

10.1.2 Conclusions

Rift-Valley Hydrography and Flow

1. The rift-valley flow in the *AMAR* segments is largely controlled by topographic effects.

2. The persistence of the flow observed at *Rainbow Sill* is consistent with the low-pass filtering property of the basin/sill model; the inferred characteristic filtering time scales of the *AMAR* segments are of order weeks to months.

3. The along-segment hydrographic gradients and the rift-valley heat budgets imply strong diapycnal mixing, consistent with the observed dynamical processes; the diffusivity estimates appear high but not impossible.

4. The known geothermal processes do not contribute significantly to the heat budget of the rift-valley water in the *AMAR* segments.

Hydrothermal Hydrographic Anomalies

1. Hydrographic anomalies associated with hydrothermal particle plumes can be detected and quantified even in locations of complex hydrography where the water column overlying the plumes is not characterized by simple T/S relationships.

2. Hydrographic anomalies derived from properties extrapolated from the water column above hydrothermal particle plumes can significantly overestimate the anomalies associated with the plumes.

***Rainbow* Hydrothermal Plume**

1. The light-scattering signals in the near-field non-buoyant hydrothermal plume behave conservatively, i.e. the particle distribution near the vent field reflects varying hydrothermal effluent concentrations.

2. Height-of-rise modeling significantly underestimates the buoyancy and heat fluxes of the *Rainbow* hydrothermal vent field, which consists of multiple discrete sources distributed over an extended area.

10.2 Implications and Speculation

10.2.1 Geothermal Fluxes

It is well known that heat-flux estimates derived from hydrothermal equilibrium plume measurements are often associated with large uncertainties (e.g. *McDuff,* 1995). In case of the

(preferred) advective flux method the main causes are the spatial and temporal variability of the hydrothermal plumes and of the background flow fields. At the *Rainbow* site both these problems are much less severe than it is usually the case. Even though the variability within individual profiles is high, a Gaussian mean plume (the first such observation in a hydrothermal context) has been derived. Our data suggest that the relationships between different hydrothermal tracers in individual profiles can yield valuable information because typical tracers behave conservatively over the short time scales required to sample single profiles. The mutual consistency of the nephel vs. spice relationships within the *Rainbow* near-field plume allows the two tracers to be combined to derive a Gaussian temperature-anomaly plume associated with comparatively small uncertainties. The background flow advecting the near-source plume away from the vent field observed during the 1997 survey was particularly simple, at least partially because of the vicinity of the hydraulically controlled overflow across *Rainbow Sill*. Taken together, these observations significantly decrease the uncertainties of the resulting heat-flux estimate.

On a regional scale, good hydrothermal flux estimates are important, especially to constrain the sources of geochemical tracers. On a global scale it appears unlikely that the fluxes can be quantified accurately from plume measurements because of the large inherent uncertainties at most sites. The problem is compounded by the uncertainty as to what proportion of the low-temperature hydrothermal effluents are incorporated into the high-temperature particle plumes.

10.2.2 Rift-Valley Hydrography and Flow

Our observations indicate that the hypothesis of *Saunders and Francis* (1985) concerning the flushing of the MAR rift valley should be revised to allow for a quasi-steady state in addition to (or instead of) periodic inflow events alternating with periods of homogenization. Their hydrographic observations suggest that there may be similar unidirectional along-valley flows in other (long) MAR segments. While geothermal processes do not appear to significantly affect the heat budgets and dynamics within the rift valley of the *AMAR* segments, our data indicate that strong diapycnal mixing gives rise to hydrographic patterns similar to those observed in canyons on the flank of the MAR (e.g. *Ledwell et al.*, 2000). To what extent mixing within the rift valleys of slow-spreading ridges is important on a global scale cannot be determined without independent confirmation of our diapycnal-diffusivity estimates nor

without observations from other segments.

The transport budgets of the *AMAR* segments suggest that diapycnal mixing may also provide an additional pathway (in addition to hydraulically controlled outflows across sills) for the water to exit the rift valley by "entrainment" into the overlying water column. It is difficult to see how this hypothesis can be tested short of a tracer-release experiment or by monitoring the input and dispersal of passive natural tracers (such as ^{3}He) over a large area. The apparent lack of hydrothermal signatures in the vicinity of the MAR (see below) is consistent with the view that the hydrothermal tracers exit the rift valley in a "diffuse" manner.

Without any diapycnal mixing and geothermal heating in the rift valley the density drop between the hydraulically controlled inflows and outflows would determine the amount of water transported along the segments. Diapycnal mixing complicates the system considerably. The hydraulic-control assumption at the inflow appears to imply that it is the upstream condition, i.e. the depth of the interface on the ridge flank, which determines the inflow and, hence, the flux through the system. In reality there is no such interface, however. The "interface" required to apply a $1\frac{1}{2}$-layer hydraulic model is taken from the depth below which there is an upstream/downstream density difference across the sill, consistent with the view that the corresponding pressure gradient drives a cross-sill flow below that depth. The amount of inflow therefore depends on the processes which control the level of that "interface". Hydraulic control implies that if there is more inflow than the system can process the control is flooded, stopping the inflow. Subsequent diapycnal mixing gradually reduces the density of the stagnant water within the rift valley, eventually "un-flooding" the control (essentially the mechanism implied by *Saunders and Francis* (1985)). It appears reasonable to suggest that this process takes place before the control is fully flooded, implying that diapycnal mixing may also play a controlling role by setting a limit for the density difference and, thus, for the flux which is achievable at the inflow sill. Because "entrainment" provides an additional potential pathway for the water out of the rift valley it is not clear if there has to be a limit beyond which the amount of mixing does not influence the transport through the system any more, as is the case in "overmixed" estuaries and marginal seas where the maximal achievable exchange is purely hydraulically controlled *(Stommel and Farmer,* 1953). These questions merit further investigation. It is suggested that laboratory experiments might be a useful first step.

10.2.3 Dispersal of Hydrothermal Tracers and Biota

It is not a new observation that the near-field dispersal of hydrothermal tracers (and biota) released into the rift-valley water column of the MAR is primarily constrained by topographic effects. Within the *AMAR* segments the unidirectional along-valley flow provides an additional, dynamical, constraint. (The sheared flow observed in 1998 casts some doubt on that conclusion, however.) This appears to be the first study where an attempt has been made to infer the fate of the rift-valley water (and the associated hydrothermal tracers) beyond segment boundaries. Passive tracers such as ^{3}He must leave the rift valley somewhere. Why are there apparently no basin-scale hydrothermal signatures in the Atlantic? Does this rule out geothermal heating as a driving process for the mid-depth westward flows as suggested by *Talley and Johnson* (1994)? What are the inter-segment colonization pathways for organisms associated with the hydrothermal vent fields of the MAR rift valley? These questions cannot be answered in the context of this study. A more integrated approach, which includes investigating the flow over the crests and on the flanks of the ridges, is required. A proposal to that effect has recently been submitted to NSF (proposal #1051486).

Bibliography

Abraham, G. and W. D. Eysink (1969). Jets issuing into fluid with a density gradient. *Journal of Hydraulic Research 7*, 145–175.

Armi, L. (1986). The hydraulics of two flowing layers with different densities. *Journal of Fluid Mechanics 163*, 27–58.

Baines, P. G. (1987). Upstream blocking and airflow over mountains. *Annual Review of Fluid Mechanics 19*, 75–97.

Baker, E. T. and J. W. Lavelle (1984). The effect of particle size on the light attenuation coefficient of natural suspensions. *Journal of Geophysical Research 89*, 8197–8203.

Baker, E. T., J. W. Lavelle, and G. L. Massoth (1985). Hydrothermal particle plumes over the southern Juan de Fuca Ridge. *Nature 316*, 342–344.

Baker, E. T. and G. J. Massoth (1987). Characteristics of hydrothermal plumes from two vent fields on the Juan de Fuca Ridge, northeast Pacific Ocean. *Earth and Planetary Science Letters 85*, 59–73.

Baker, E. T., J. W. Lavelle, R. A. Feely, G. L. Massoth, and S. L. Walker (1989). Episodic venting of hydrothermal fluids from the Juan de Fuca Ridge. *Journal of Geophysical Research 94*, 9237–9250.

Baker, E. T. and J. E. Lupton (1990). Changes in submarine hydrothermal ^{3}He/heat ratios as an indicator of magmatic/tectonic activity. *Nature 346*, 556–558.

Baker, E. T., R. E. McDuff, and G. J. Massoth (1990). Hydrothermal venting from the summit of a ridge axis seamount: Axial Volcano, Juan de Fuca Ridge. *Journal of Geophysical Research 95*, 12843–12854.

Baker, E. T. and S. R. Hammond (1992). Hydrothermal venting and the apparent magmatic budget of the Juan de Fuca Ridge. *Journal of Geophysical Research 97*, 3443–3456.

Baker, E. T. (1994). A six-year time series of hydrothermal plumes over the Cleft segment of the Juan de Fuca Ridge. *Journal of Geophysical Research 99*, 4889–4904.

Baker, E. T., G. J. Massoth, R. A. Feely, R. W. Embley, R. E. Thomson, and B. J. Burd (1995). Hydrothermal event plumes from the CoAxial sea-floor eruption site, Juan de Fuca Ridge. *Geophysical Research Letters 22*, 147–150.

Baker, E. T., C. G. Fox, and J. P. Cowen (1999). In situ observations of the onset of hydrothermal discharge during the 1998 submarine eruption of Axial Volcano, Juan de Fuca Ridge. *Geophysical Research Letters 26*, 3445–3448.

Bemis, K. G., R. P. von Herzen, and M. J. Mottl (1993). Geothermal heat flux from hydrothermal plumes on the Juan de Fuca Ridge. *Journal of Geophysical Research 98*, 6351–6369.

Bendat, J. S. and A. G. Piersol (1971). *Random Data: Analysis and Measurement Procedures*. Wiley-Interscience. 407 pp.

Bischoff, J. L. and R. J. Rosenbauer (1985). An empirical equation of state for hydrothermal seawater (3.2% NaCl). *American Journal of Science 285*, 725–763.

Chin, C. S., K. H. Coale, V. A. Elrod, K. S. Johnson, G. J. Massoth, and E. T. Baker (1994). In situ observations of dissolved iron and manganese in hydrothermal vent plumes, Juan de Fuca Ridge. *Journal of Geophysical Research 99*, 4969–4984.

Converse, D. R., H. D. Holland, and J. M. Edmond (1984). Flow rates in the axial hot springs of the East Pacific Rise (21°N): Implications for the heat budget and the formation of massive sulfide deposits. *Earth and Planetary Science Letters 69*, 159–175.

Detrick, R. S., H. D. Needham, and V. Renard (1995). Gravity anomalies and crustal thickness variations along the Mid-Atlantic Ridge between 33°N and 40°N. *Journal of Geophysical Research 100*, 3767–3787.

Dickson, R. R., E. M. Gmitrowicz, and A. J. Watson (1990). Deep-water renewal in the northern North Atlantic. *Nature 344*, 848–850.

Eittreim, S., E. M. Thorndike, and L. Sullivan (1976). Turbidity distribution in the Atlantic Ocean. *Deep-Sea Research 23*, 1115–1127.

Elderfield, H. and A. Schultz (1996). Mid-ocean ridge hydrothermal fluxes and the chemical composition of the ocean. *Annual Review of Earth and Planetary Sciences 24*, 191–224.

Feely, R. A., M. Lewison, G. J. Massoth, G. Robert-Baldo, J. W. Lavelle, R. H. Byrne, K. L. Von Damm, and H. C. Curl Jr. (1987). Composition and dissolution of black smoker particulates from active vents on the Juan de Fuca Ridge. *Journal of Geophysical Research 92*, 11347–11363.

Fernandez, E. and R. D. Pingree (1996). Coupling between physical and biological fields in the North Atlantic subtropical front southeast of the Azores. *Deep-Sea Research 43*, 1369–1393.

Fischer, H. B. (1971). The dilution of an undersea sewage cloud by salt fingers. *Water Research 5*, 909–915.

Fischer, H. B. (1979). Turbulent jets and plumes. In H. B. Fischer, E. J. List, R. C. Koh, J. Imberger, and N. H. Brooks (Eds.), *Mixing in Inland and Coastal Waters*, pp. 315–389. Academic Press.

Flierl, G. R. and J. C. McWilliams (1978). On the sampling requirements for measuring moments of eddy variability. *Journal of Marine Research 35*, 797–820.

Fouquet, Y., F. Barriga, J. L. Charlou, H. Elderfield, C. R. German, H. Ondréas, L. Parson, J. Radford-Knoery, J. Relvas, A. Ribeiro, A. Schultz, R. Apprioual, P. Cambon, I. Costa, J. P. Donval, E. Douville, J. Y. Landuré, A. Normand, H. Pellé, E. Ponsevera, S. Riches, H. Santana, and M. Stephan (1998). FLORES diving cruise with the Nautile near the Azores — first dives on the Rainbow field: hydrothermal seawater/mantle interaction. *InterRidge News 7*, 24–28.

Fowler, C. M. (1990). *The Solid Earth: An Introduction to Global Geophysics*. Cambridge University Press. 472 pp.

Fukumori, I., F. Martel, and C. Wunsch (1991). The hydrography of the North Atlantic in the early 1980s. An atlas. *Progress in Oceanography 27*, 1–110.

German, C. R. and R. S. Sparks (1991). Particle recycling in the TAG hydrothermal plume. *Earth and Planetary Science Letters 116*, 129–134.

German, C. R., D. R. Dixon, H. Elderfield, P. J. Herring, M. R. Palmer, and K. J. Richards (1995). FLAME: The fluxes at AMAR experiment. *Research Proposal*.

German, C. R., L. M. Parson, C. Wilson, G. P. Klinkhammer, D. J. Fornari, and S. E. Humphris (1996a). The geologic setting of the Rainbow hydrothermal field, Mid-Atlantic Ridge. *EOS: Transactions, American Geophysical Union 77*, 707.

German, C. R., L. M. Parson, and the HEAT Scientific Team (1996b). Hydrothermal exploration at the Azores triple-junction: Tectonic control of venting at slow-spreading ridges? *Earth and Planetary Science Letters 138*, 93–104.

German, C. R., G. P. Klinkhammer, and M. D. Rudnicki (1996c). The Rainbow hydrothermal plume, 36°15′N, Mid-Atlantic Ridge. *Geophysical Research Letters 23*, 2979–2982.

German, C. R. and L. M. Parson (1998). Distributions of hydrothermal activity along the Mid-Atlantic Ridge: interplay of magmatic and tectonic controls. *Earth and Planetary Science Letters 160*, 327–341.

German, C. R., K. J. Richards, M. D. Rudnicki, M. M. Lam, J. L. Charlou, and the FLAME Scientific Party (1998). Topographic control of a dispersing hydrothermal plume. *Earth and Planetary Science Letters 156*, 267–273.

Gill, A. E. (1982). *Atmosphere-Ocean Dynamics*. Academic Press. 662 pp.

Ginster, U., M. J. Mottl, and R. P. Von Herzen (1994). Heat flux from black smokers on the Endeavor and Cleft segments, Juan de Fuca Ridge. *Journal of Geophysical Research 99*, 4937–4950.

Gonella, J. (1972). A rotary-component method for analysing meteorological and oceanographic vector time series. *Deep-Sea Research 19*, 833–846.

Gould, W. J. (1985). Physical oceanography of the Azores front. *Progress in Oceanography 14*, 167–190.

Hamming, R. W. (1989). *Digital Filters*. Prentice Hall. 284 pp.

Hautala, S. L. and S. C. Riser (1993). A nonconservative β-spiral determination of the deep circulation in the eastern South Pacific. *Journal of Physical Oceanography 23*, 1975–2000.

Helfrich, K. R. and T. Battisti (1991). Experiments on baroclinic vortex shedding from hydrothermal plumes. *Journal of Geophysical Research 96*, 12511–12518.

Helfrich, K. R. (1994). Thermals with background rotation and stratification. *Journal of Fluid Mechanics 259*, 265–280.

Helfrich, K. R. and K. G. Speer (1995). Oceanic hydrothermal circulation: Mesoscale and basin-scale flow. In S. E. Humphris, R. A. Zierenberg, L. S. Mullineaux, and R. E. Thomson (Eds.), *Seafloor Hydrothermal Systems: Physical, Chemical, Biological, and Geological Interactions*, pp. 347–356. American Geophysical Union.

Helfrich, K. R., T. M. Joyce, G. A. Cannon, S. A. Harrington, and D. J. Pashinski (1998). Mean hydrographic and velocity sections near Pipe Organ vent at Juan de Fuca Ridge. *Geophysical Research Letters 25*, 1737–1740.

Hogg, N., P. Biscaye, W. Gardner, and W. J. Schmitz (1982). On the transport and modification of Antarctic Bottom Water in the Vema Channel. *Journal of Marine Research 40*, 231–263.

Hoyal, D. C. D., M. I. Bursik, and J. F. Atkinson (1999). Settling-driven convection: A mechanism of sedimentation from stratified fluids. *Journal of Geophysical Research 104*, 7953–7966.

IAGA Division V Working Group 8 (1995). International geomagnetic field, 1995 revision. *Journal of Geomagnetism and Geoelectricity 47*, 1257–1261.

James, R. H., Elderfield, M. D. H., Rudnicki, C. R. German, M. R. Palmer, C. Chin, M. J. Greaves, E. Gurvich, G. P. Klinkhammer, E. Ludford, R. A. Mills, J. Thomson, and A. C. Williams (1995). Hydrothermal plumes at Broken Spur, 29°N Mid-Atlantic Ridge: Chemical and physical characteristics. In L. M. Parson, C. L. Walker, and D. R. Dixon (Eds.), *Hydrothermal Vents and Processes*, pp. 97–110. London: The Geological Society.

Jean-Baptiste, P., H. Bougault, A. Vangriesheim, J. L. Charlou, J. Radford-Knoery, Y. Fouquet, D. Needham, and C. German (1998). Mantle ^{3}He in hydrothermal vents and plume of the Lucky Strike site (Mid-Atlantic Ridge 36°17′N) and associated geothermal heat flux. *Earth and Planetary Science Letters 157*, 69–77.

Joyce, T. and K. Speer (1987). Modelling the large-scale influence of a geothermal source on abyssal flow. *Journal of Geophysical Research 92*, 2843–2850.

Joyce, T. M., B. A. Warren, and L. D. Talley (1986). The geothermal heating of the abyssal subarctic Pacific Ocean. *Deep-Sea Research 33*, 1003–1015.

Joyce, T. M., G. A. Cannon, K. R. Helfrich, S. A. Harrington, and D. Pashinski (1998).

Vertical and temporal vorticity observation at Juan de Fuca Ridge: hydrothermal signatures. *Geophysical Research Letters 25*, 1741–1744.

Kadko, D. C., N. D. Rosenberg, J. E. Lupton, R. W. Collier, and M. D. Lilley (1990). Chemical reaction rates and entrainment within the Endeavor Ridge hydrothermal plume. *Earth and Planetary Science Letters 99*, 315–335.

Killworth, P. D. (1994). On reduced-gravity flow through sills. *Geophysical and Astrophysical Fluid Dynamics 75*, 91–106.

Killworth, P. D. (1995). Hydraulic control and maximal flow in rotating stratified hydraulics. *Deep-Sea Research 42*, 859–871.

Kim, S. L. and L. S. Mullineaux (1998). Distribution and near-bottom transport of larvae and other plankton at hydrothermal vents. *Deep-Sea Research 2 45*, 423–440.

Kinder, T. H. and H. L. Bryden (1990). Aspiration of deep waters through straits. In L. J. Pratt (Ed.), *The Physical Oceanography of Sea Straits*, pp. 295–319. Kluwer Academic Publishers.

Lane-Serff, G. F. (1995). Particle recycling in hydrothermal plumes: comment on "Particle recycling in the TAG hydrothermal plume" by C.R. German and R.S.J. Sparks (1993). *Earth and Planetary Science Letters 132*, 233–234.

Lavelle, J. W. (1997). Buoyancy-driven plumes in rotating, stratified cross flows: Plume dependence on rotation, turbulent mixing, and cross-flow strength. *Journal of Geophysical Research 102*, 3405–3420.

Lavelle, J. W., E. T. Baker, and G. J. Massoth (1998). On the calculation of total heat, salt and tracer fluxes from ocean hydrothermal events. *Deep-Sea Research 2 45*, 2619–2636.

LeBlond, P. H. and L. A. Mysak (1978). *Waves in the Ocean*. Elsevier. 602 pp.

Ledwell, J. R., E. T. Montgomery, K. L. Polzin, L. C. StLaurent, R. W. Schmitt, and J. M. Toole (2000). Evidence for enhanced mixing over rough topography in the abyssal ocean. *Nature 403*, 179–182.

List, E. J. (1982). Turbulent plumes and jets. *Annual Reviews in Fluid Mechanics 14*, 189–212.

Lowell, R. P., P. A. Rona, and R. P. Von Herzen (1995). Seafloor hydrothermal systems. *Journal of Geophysical Research 100*, 327–352.

Lukashin, V. N., A. P. Lisitzin, G. V. Ivanov, V. A. Kravtsov, and V. Rusakov (1995). The southern hydrothermal plume at the Broken Spur vent field, 29°N (BRAVEX-94). *BRIDGE Newsletter 9*, 20–23.

Lupton, J. E., G. P. Klinkhammer, W. R. Normark, R. Haymon, K. C. MacDonald, R. F. Weiss, and H. Craig (1980). Helium-3 and manganese at the 21°N East Pacific Rise hydrothermal site. *Earth and Planetary Science Letters 50*, 115–127.

Lupton, J. E., J. R. Delaney, H. P. Johnson, and M. K. Tivey (1985). Entrainment and vertical transport of deep-ocean water by buoyant hydrothermal plumes. *Nature 316*, 621–623.

Lupton, J. E. (1995). Hydrothermal plumes: Near and far field. In S. E. Humphris, R. A. Zierenberg, L. S. Mullineaux, and R. E. Thomson (Eds.), *Seafloor Hydrothermal Systems: Physical, Chemical, Biological, and Geological Interactions*, pp. 317–346. American Geophysical Union.

Lupton, J. E., E. T. Baker, N. Garfield, G. J. Massoth, R. A. Feely, J. P. Cowen, R. R. Greene, and T. A. Rago (1998). Tracking the evolution of a hydrothermal event plume with a RAFOS neutrally buoyant drifter. *Science 280*, 1052–1055.

Lupton, J. E., E. T. Baker, and G. J. Massoth (1999). Helium, heat, and the generation of hydrothermal event plumes at mid-ocean ridges. *Earth and Planetary Science Letters 171*, 343–350.

Macdonald, K. C., D. S. Scheirer, and S. M. Carbotte (1991). Mid-ocean ridges: Discontinuities, segments and giant cracks. *Science 253*, 986–994.

McDougall, T. J. (1990). Bulk properties of "hot smoker" plumes. *Earth and Planetary Science Letters 99*, 185–194.

McDuff, R. E. (1988). Effects of vent fluid properties on the hydrography of hydrothermal plumes. *EOS: Transactions, American Geophysical Union 69*, 1497.

McDuff, R. E. (1995). Physical dynamics of deep-sea hydrothermal plumes. In S. E. Humphris, R. A. Zierenberg, L. S. Mullineaux, and R. E. Thomson (Eds.), *Seafloor Hydrothermal Systems: Physical, Chemical, Biological, and Geological Interactions*, pp. 357–368. American Geophysical Union.

Mercier, H. and H. L. Bryden (1994). Flow of Antarctic Bottom Water over the sill in the

Romanche Fracture Zone. *International WOCE Newsletter 17*, 9–10.

Middleton, J. M. and R. E. Thomson (1986). Modelling the rise of hydrothermal plumes. *Canadian Technical Report on Hydrography and Ocean Science 69*, 18pp.

Mihaly, S. F., R. E. Thomson, and A. B. Rabinovich (1998). Evidence for nonlinear interaction between internal waves of inertial and semidiurnal frequency. *Geophysical Research Letters 25*, 1205–1208.

Mooers, C. N. (1973). A technique for the cross spectrum analysis of pairs of complex-valued time series, with emphasis on properties of polarized components and rotational invariants. *Deep-Sea Research 20*, 1129–1141.

Morton, B. R., G. I. Taylor, and J. S. Turner (1956). Turbulent gravitational convection from maintained and instantaneous sources. *Proceedings of the Royal Society of London A234*, 1–13.

Müller, P., D. J. Olbers, and J. Willebrand (1978). The Iwex spectrum. *Journal of Geophysical Research 83*, 479–500.

Munk, W. (1966). Abyssal recipes. *Deep-Sea Research 13*, 707–730.

Munk, W. (1981). Internal waves and small-scale processes. In B. A. Warren and C. Wunsch (Eds.), *Evolution of Physical Oceanography*, pp. 264–291. M.I.T. Press.

Munk, W. and C. Wunsch (1998). Abyssal recipes II: energetics of tidal and wind mixing. *Deep-Sea Research 45*, 1977–2010.

Murton, B. J., L. J. Redbourn, C. R. German, and E. T. Baker (1999). Sources and fluxes of hydrothermal heat, chemicals and biology within a segment of the Mid-Atlantic Ridge. *Earth and Planetary Science Letters 171*, 301–317.

Nelsen, T. A., G. P. Klinkhammer, J. H. Trefry, and R. P. Trocine (1987). Real-time observation of dispersed hydrothermal plumes using nephelometry: examples from the Mid-Atlantic Ridge. *Earth and Planetary Science Letters 81*, 245–252.

Papantoniou, D. and E. J. List (1989). Large-scale structure in the far field of buoyant jets. *Journal of Fluid Mechanics 209*, 151–190.

Pierrehumbert, R. T. and B. Wyman (1985). Upstream effects of mesoscale mountains. *Journal of Atmospheric Sciences 42*, 977–1003.

Polzin, K. L., J. M. Toole, and R. W. Schmitt (1995). Finescale parameterizations of turbulent dissipation. *Journal of Physical Oceanography 25*, 306–328.

Polzin, K. L., K. G. Speer, J. M. Toole, and R. W. Schmitt (1996). Intense mixing of Antarctic Bottom Water in the equatorial Atlantic Ocean. *Nature 380*, 54–57.

Polzin, K. L., J. M. Toole, J. R. Ledwell, and R. W. Schmitt (1997). Spatial variability of turbulent mixing in the abyssal ocean. *Science 276*, 93–96.

Pratt, L. J. (1986). Hydraulic control of sill flow with bottom friction. *Journal of Physical Oceanography 16*, 1970–1980.

Press, W. H., S. A. Teukolsky, W. T. Vetterling, and B. P. Flannery (1993). *Numerical Recipes in C* (2nd ed.). Cambridge University Press. 1020 pp.

Priestley, C. H. (1956). A working theory of the bent-over plume of hot gas. *Quarterly Journal of the Royal Meteorological Society 82*, 165–176.

Queney, P. (1948). The problem of air flow over mountains: A summary of theoretical studies. *Bulletin of the American Meteorological Society 29*, 16–26.

Radford-Knoery, J., A. M. Thurnherr, C. R. German, K. J. Richards, J. L. Charlou, J. P. Donval, Y. Fouquet, and Flame and Flame-II Scientific Parties (1998). Dissolved manganese in AMAR and South AMAR axial valleys (Mid-Atlantic Ridge at 35°40-36°40N). *EOS: Transactions, American Geophysical Union 79*, 837.

Read, J. F. and R. T. Pollard (1999). Deep inflow into the Mozambique Basin. *Journal of Geophysical Research 104*, 3075–3090.

Rehder, G., R. S. Keir, E. Suess, and M. Rhein (1999). Methane in the northern Atlantic controlled by microbial oxidation and atmospheric history. *Geophysical Research Letters 26*, 587–590.

Reid, J. L. (1982). Evidence of an effect of heat flux from the East Pacific Rise upon the characteristics of the mid-depth waters. *Geophysical Research Letters 9*, 381–384.

Roemmich, D. and C. Wunsch (1985). 2 transatlantic sections — meridional circulation and heat-flux in the sub-tropical North-Atlantic Ocean. *Deep-Sea Research 32*, 619–664.

Roether, W., R. Well, A. Putzka, and C. Ruth (1998). Component separation of oceanic helium. *Journal of Geophysical Research 103*, 27931–27946.

Rona, P. and A. Trivett (1992). Discrete and diffuse heat transfer at ASHES vent field, Axial Volcano, Juan de Fuca Ridge. *Earth and Planetary Science Letters 109*, 57–71.

Rona, P. A., B. A. McGregor, P. R. Betzer, and D. C. Krause (1974). Anomalous water temperatures over Mid-Atlantic Ridge crest at 26°N. *EOS: Transactions, American Geophysical Union 55*, 293.

Rona, P. A. and K. G. Speer (1989). An Atlantic hydrothermal plume: Trans-Atlantic Geotraverse (TAG) area, Mid-Atlantic Ridge crest near 26°N. *Journal of Geophysical Research 94*, 13879–13893.

Rudnicki, M. D. and H. Elderfield (1992). Theory applied to the Mid-Atlantic Ridge hydrothermal plumes: The finite-difference approach. *Journal of Volcanology and Geothermal Research 50*, 161–172.

Rudnicki, M. D., R. H. James, and H. Elderfield (1994). Near-field variability of the TAG non-buoyant plume, 26°N, Mid-Atlantic Ridge. *Earth and Planetary Science Letters 127*, 1–10.

Rudnicki, M. D., C. R. German, R. E. Kirk, M. Sinha, H. Elderfield, and S. Riches (1995). New instrument platform tested at Mid-Atlantic Ridge. *EOS: Transactions, American Geophysical Union 76*, 329–330.

Rudnicki, M. D. (1995). Particle formation, fallout and cycling within the buoyant and non-buoyant plume above the TAG vent field. In L. M. Parson, C. L. Walker, and D. R. Dixon (Eds.), *Hydrothermal Vents and Processes*, pp. 387–396. The Geological Society.

Rüth, C., R. Well, and W. Roether (2000). Primordial ^{3}He in South Atlantic deep waters from sources on the Mid-Atlantic Ridge. *Deep-Sea Research 47*, 1059–1075.

Saunders, P. M. and T. J. Francis (1985). The search for hydrothermal sources on the Mid-Atlantic Ridge. *Progress in Oceanography 14*, 527–536.

Saunders, P. M. (1987). Flow through Discovery Gap. *Journal of Physical Oceanography 17*, 631–643.

Schultz, A., J. R. Delaney, and R. E. McDuff (1992). On the partitioning of heat flux between diffuse and point source seafloor venting. *Journal of Geophysical Research 97*, 12299–12314.

Schultz, A. and H. Elderfield (1997). Controls on the physics and chemistry of seafloor hydrothermal circulation. *Philosophical Transactions of the Royal Society A355*, 387–425.

Smith, W. H. and D. T. Sandwell (1997). Bathymetric prediction from dense altimetry and sparse shipboard bathymetry. *Journal of Geophysical Research 99*, 21803–21824.

Speer, K. G. and P. A. Rona (1989). A model of an Atlantic and Pacific hydrothermal plume. *Journal of Geophysical Research 94*, 6213–6220.

Speer, K. G. and J. Marshall (1995). The growth of convective plumes at seafloor hot springs. *Journal of Marine Research 53*, 1025–1057.

Speer, K. G. and K. R. Helfrich (1995). Hydrothermal plumes: a review of flow and fluxes. In L. M. Parson, C. L. Walker, and D. R. Dixon (Eds.), *Hydrothermal Vents and Processes*, pp. 373–386. London: The Geological Society.

Stein, C. A. and S. Stein (1994). Constraints on hydrothermal heat-flux through the oceanic lithosphere from global heat-flow. *Journal of Geophysical Research 99*, 3081–3095.

Stommel, H. and H. G. Farmer (1953). Control of salinity in an estuary by a transition. *Journal of Marine Research 12*, 13–20.

Stommel, H. (1962). On the cause of the temperature-salinity curve in the ocean. *Proceedings. National Academy of Sciences 48*, 764–766.

Stommel, H. (1982). Is the South Pacific helium-3 plume dynamically active? *Earth and Planetary Science Letters 61*, 63–67.

Sy, A. (1988). Investigation of large-scale circulation patterns in the central North Atlantic: the North Atlantic Current, the Azores Current, and the Mediterranean Water plume in the area of the Mid-Atlantic Ridge. *Deep-Sea Research 35*, 383–413.

Talley, L. D. and G. C. Johnson (1994). Deep, zonal subequatorial currents. *Science 263*, 1125–1128.

Thompson, L. and G. C. Johnson (1996). Abyssal currents generated by diffusion and geothermal heating over rises. *Deep-Sea Research 43*, 193–211.

Thomson, R. E., R. L. Gordon, and J. Dymond (1989). Acoustic Doppler Current Profiler observations of a mid-ocean ridge hydrothermal plume. *Journal of Geophysical Research 94*, 4709–4720.

Thomson, R. E., J. R. Delaney, R. E. McDuff, D. R. Janecky, and J. S. McClain (1992). Physical characteristics of the Endeavor Ridge hydrothermal plume during July 1988. *Earth and Planetary Science Letters 111*, 141–154.

Thomson, R. E., E. E. Davis, and B. J. Burd (1995). Hydrothermal venting and geothermal heating in Cascadia Basin. *Journal of Geophysical Research 100*, 6121–6141.

Thurnherr, A. M. and K. J. Richards (2000). Hydrography and high-temperature heat flux of the Rainbow hydrothermal site (36°14′N, Mid-Atlantic Ridge). *accepted by Journal of Geophysical Research — Oceans*.

Trivett, D. A. and A. J. Williams (1994). Effluent from diffuse hydrothermal venting. 2. measurements of plumes from diffuse hydrothermal vents at the southern Juan de Fuca Ridge. *Journal of Geophysical Research 99*, 18417–18432.

Tunnicliffe, V. (1991). The biology of hydrothermal vents: Ecology and evolution. In M. Barnes (Ed.), *Oceanography and Marine Biology, An Annual Review*, Volume 29, pp. 319–407. Aberdeen University Press.

Turner, J. S. (1973). *Buoyancy Effects in Fluids*. Cambridge University Press. 368 pp.

Turner, J. S. (1986). Turbulent entrainment: The development of the entrainment assumption, and its application to geophysical flows. *Journal of Fluid Mechanics 173*, 431–471.

Turner, J. S. and I. H. Campbell (1987). Temperature, density and buoyancy fluxes in "black smoker" plumes, and the criterion for buoyancy reversal. *Earth and Planetary Science Letters 86*, 85–92.

Von Damm, K. L. (1995). Controls on the chemistry and temporal variability of seafloor hydrothermal fluids. In S. E. Humphris, R. A. Zierenberg, L. S. Mullineaux, and R. E. Thomson (Eds.), *Seafloor Hydrothermal Systems: Physical, Chemical, Biological, and Geological Interactions*, pp. 222–247. American Geophysical Union.

Weiss, R. F., P. Lonsdale, J. E. Lupton, A. E. Bainbridge, and H. Craig (1977). Hydrothermal plumes in the Galapagos Rift. *Nature 267*, 600–603.

Wesson, J. C. and M. C. Gregg (1994). Mixing at Camarinal Sill in the Strait of Gibraltar. *Journal of Geophysical Research 99*, 9847–9878.

Whitehead, J. A., A. Leetmaa, and R. A. Knox (1974). Rotating hydraulics of straits and sill flows. *Geophysical Fluid Dynamics 6*, 101–125.

Whitehead, J. A. and L. V. Worthington (1982). The flux and mixing rates of Antarctic Bottom Water within the North Atlantic. *Journal of Geophysical Research 87*, 7903–7924.

Whitehead, J. A. (1989). Internal hydraulic control in rotating fluids — applications to oceans. *Geophysical and Astrophysical Fluid Dynamics 48*, 169–192.

Whitehead, J. A. (1997). Critical control at deep ocean passages. *International WOCE Newsletter 28*, 14–17.

Wilson, C., K. Speer, J.-L. Charlou, H. Bougault, and G. Klinkhammer (1995). Hydrography above the Mid-Atlantic Ridge (33°–40°N) and within the Lucky Strike segment. *Journal of Geophysical Research 100*, 20555–20564.

Wilson, C., J. L. Charlou, E. Ludford, G. Klinkhammer, C. Chin, H. Bougault, C. German, K. Speer, and M. Palmer (1996). Hydrothermal anomalies in the Lucky Strike segment on the Mid-Atlantic Ridge (37°17′N). *Earth and Planetary Science Letters 142*, 467–477.